Quantum tests of causal structures and non-orthogonal states

by

Megan Agnew

A thesis
presented to the University of Waterloo
in fulfillment of the
thesis requirement for the degree of
Master of Science
in
Physics - Quantum Information

Waterloo, Ontario, Canada, 2014

I hereby declare that I am the sole author of this thesis. This is a true copy of the thesis, including any required final revisions, as accepted by my examiners.

I understand that my thesis may be made electronically available to the public.

Abstract

This thesis details two experimental tests that can be applied to particular quantum states to reveal important information. We begin by discussing the relevant background in quantum information. We introduce qubits and qu$d$its as basic quantum states, and we discuss the evolution and measurement of quantum states. We then discuss quantum state tomography as a means by which to obtain complete information about a state, followed by a discussion of state discrimination as a means by which to determine the state given the promise that it is drawn from some known set. We then discuss relevant experimental techniques in quantum optics, including measurement, generation of entanglement, and generation of single photons from entanglement.

The first experiment we discuss deals with the causal structure of a system, which is the description of the origin of correlations between two or more states. The causal structure can be direct-cause, meaning that one state causes the other; common-cause, meaning that both states are caused by another; or hybrid-cause, which is a combination of the two. We perform the first implementation of a new type of tomography to determine the causal structure; this is called causal tomography and functions regardless of whether two qubits are related by a common state, a process, or some combination thereof. We implement a process on two entangled photons so that we can select the exact causal structure that results, which ranges continuously between direct-cause and common-cause structures. Using causal tomography, we recover causal structures that closely match expected results and demonstrate that quantum mechanics provides an advantage in causal inference.

The second experiment we discuss deals with the unambiguous discrimination of multiple quantum states. For the first time, we apply the principles of unambiguous state discrimination to high-dimensional systems. Given a state chosen randomly out of d possible states encoded in d dimensions, we implement a procedure for determining which state was chosen; this procedure in theory functions without error. We encode and detect the states in the orbital angular momentum degree of freedom up to dimension $d = 14$. Although no experiment can provide perfectly error-free measurement due to inevitable imperfections, we obtain an error rate below the theoretical error rate of minimum-error state discrimination for dimensions up to $d = 12$. At the time of submission of this thesis, this work has been accepted for publication in Physical Review Letters.

Acknowledgements

First, I would like to thank my supervisor, Kevin Resch, for his guidance throughout my degree. I thank my committee members, Donna Strickland and Matteo Mariantoni. I also thank Thomas Jennewein for agreeing to be on my examining committee.

Second, I would like to thank all of my colleagues in the Resch group who have helped me and provided guidance during my degree. I thank John Donohue for introducing me to the Resch lab and trying to impress upon me the importance of a lab book; Jonathan Lavoie for using my need for help in the lab as an excuse not to write his thesis; Lydia Vermeyden for her patience in teaching me about the Sagnac source, and her help and company in the lab; Mike Mazurek for the hours we spent in the lab trying to get a time tagger working; and the entire group, including Kent Fisher, Jean-Philippe MacLean, and Deny Hamel, for always having a minute to answer my numerous questions.

I would also like to thank my colleagues in Scotland for their help and company during my time there. It was a pleasure to work with both Eliot Bolduc and Francesco Tonolini, and I look forward to working with them again when I return for my PhD. I would also like to thank my Scottish supervisor, Jonathan Leach, for his immeasurable guidance and support, and I look forward to continuing our work together during my PhD.

I extend special thanks to my friends for keeping me sane during my degree. In particular, Corey Rae, Will, Mike, and John, thanks for all the great evenings at Kickoff and for all your caring and support. Jonathan, Lizzie, Eliot, and Geneviève, it's difficult to express my gratitude for everything you've done for me; you all know how important a role you have played in my decision to return to Scotland.

I must also thank the agencies that have provided funding for the equipment I used: the Natural Sciences and Engineering Research Council of Canada (NSERC), Canada Research Chairs, Industry Canada, the Canada Foundation for Innovation (CFI), and the Engineering and Physical Sciences Research Council (EPSRC). I also thank NSERC in particular for funding part of my degree, including my time in Scotland.

I leave the final thanks to my parents and my sister for their constant love and unwavering support, and their ability to listen to language like "quantum" for at least five minutes before tuning out.

An unknown person did something that no one else saw, the nature and extent of which is impossible to determine, and the result of which will be lost in the chaotic chain of causation and consequence that is history.

– "History Week," Welcome to Nightvale

There's going to come a day when you feel better;
You'll rise up free and easy on that day
And float from branch to branch,
Lighter than the air.
Just when that day is coming, who can say?

– "Up the Wolves," The Mountain Goats

We passed the time from one end of twelve to the other without stopping once. Well done, us! Good job, people who experience time! Time experiencers: good job!

– "History Week," Welcome to Nightvale

On second thought I'd rather hang around
And be there with my best friend
If she wants me.

– "If She Wants Me," Belle & Sebastian

Table of Contents

List of Tables

List of Figures

Chapter 1

Introduction

1.1 Quantum States

1.1.1 Qubits

A classical bit can be used to convey information and can exist in one of two states, for example, a switch that can be pointed "up" or "down". These states are typically represented as "0" and "1". Conversely, a quantum bit, or qubit, can exist in a superposition of two states, denoted $|0\rangle$ and $|1\rangle$. Each of these is represented by a vector in a two-dimensional Hilbert space $\mathcal{H}^2$ as

$$|0\rangle = \begin{pmatrix} 1 \\ 0 \end{pmatrix}; \quad |1\rangle = \begin{pmatrix} 0 \\ 1 \end{pmatrix}. \tag{1.1}$$

As these vectors form a basis for $\mathcal{H}^2$, we can represent any pure qubit state $|\psi\rangle$ as a superposition of these two such that

$$|\psi\rangle = \alpha|0\rangle + \beta|1\rangle. \tag{1.2}$$

The coefficients α and β are complex numbers; $|\alpha|^2$ and $|\beta|^2$ indicate the probability of the qubit being found in the state $|0\rangle$ and $|1\rangle$, respectively. As these probabilities must sum to unity, the state must be normalised.

An example of a physical qubit is the polarisation state of a single photon. Light is an electromagnetic wave whose electric field oscillates as it travels; the direction of this oscillation is called polarisation. This electromagnetic field can be quantised, resulting in the concept of a photon: a quantum of light. Photons can be polarised horizontally

$(|H\rangle \equiv |0\rangle)$ or vertically $(|V\rangle \equiv |1\rangle)$, which forms a basis; any polarisation state can be expressed as a superposition of these two polarisations. For example, an equal superposition of horizontal and vertical states describes an electric field oscillating diagonally $|D\rangle = (|H\rangle + |V\rangle)/\sqrt{2}$ or anti-diagonally $|A\rangle = (|H\rangle - |V\rangle)/\sqrt{2}$; these two states are orthogonal and thus also form a basis. An imaginary component in the superposition describes an electric field oscillating elliptically, such as right circular polarisation $|R\rangle = (|H\rangle + i|V\rangle)/\sqrt{2}$ or left circular polarisation $|L\rangle = (|H\rangle - i|V\rangle)/\sqrt{2}$; once again, these two states form a basis.

1.1.2 Qu*d*its

The concept of a qubit can be extended further than a two-dimensional Hilbert space. We can describe a qu*d*it in a d-dimensional Hilbert space $\mathcal{H}^d$ with basis states $\{|0\rangle, ..., |d-1\rangle\}$. Similar to qubits, the basis state $|j\rangle$ represents a vector of length d where the jth component is 1 and the others 0; for example, in a 3-dimensional space, a set of basis vectors is

$$|0\rangle = \begin{pmatrix} 1 \\ 0 \\ 0 \end{pmatrix}; \quad |1\rangle = \begin{pmatrix} 0 \\ 1 \\ 0 \end{pmatrix}; \quad |2\rangle = \begin{pmatrix} 0 \\ 0 \\ 1 \end{pmatrix}. \tag{1.3}$$

The state $|\psi\rangle$ of a qu*d*it can then be represented as

$$|\psi\rangle = \sum_{j=0}^{d-1} c_j |j\rangle, \tag{1.4}$$

where $|c_j|^2$ represents the probability of finding the qu*d*it in state $|j\rangle$. Once again, these probabilities sum to unity.

An example of a physical qu*d*it is the orbital angular momentum (OAM) of light. Light can possess an intrinsic orbital angular momentum so that its energy is spiralling around the axis of propagation. The faster it spirals, the more OAM it has. We denote a single photon with OAM $\ell\hbar$ as being in the state $|\ell\rangle$. This index ℓ is discrete and infinite; it can take on any positive or negative integer value. By encoding a single photon with a d-dimensional subset of these OAM values, we can readily access a physical qu*d*it.

1.1.3 Multi-particle states

In addition to using quantum states to describe single particles, it is also possible to describe the state of several particles at once. The combined state of multiple particles

2

can be described simply by the tensor product of the states of the constituent particles. For example, a particle in state $|\psi_1\rangle \in \mathcal{H}_1^a$ and a particle in state $|\psi_2\rangle \in \mathcal{H}_2^b$ combine to form the state $|\Psi\rangle = |\psi_1\rangle \otimes |\psi_2\rangle$. This two-particle state exists in the combined Hilbert space $\mathcal{H}_1^a \otimes \mathcal{H}_2^b$, whose basis consists of the tensor products of all the basis states of the constituent Hilbert spaces. That is, any two-particle state can be described as

$$|\Psi\rangle = \sum_{j=1}^{a} \sum_{k=1}^{b} c_{j,k} |j\rangle_1 \otimes |k\rangle_2, \tag{1.5}$$

where $\{|j\rangle\}$ and $\{|k\rangle\}$ are the basis states of the two constituent spaces and $|c_{j,k}|^2$ is the probability of finding particle 1 in the state $|j\rangle$ and particle 2 in the state $|k\rangle$.

1.1.4 Mixed states

The states we have described thus far have all been pure in that they are superpositions of basis states. Diagonally polarised light, for example, is in an equal superposition of horizontal and vertical polarisations; it is simultaneously in both states. However, it is also possible for a particle to be in a mixed state. A mixed state consists of two or more different pure states weighted by probabilities. For example, a source emitting light in a mixed polarisation state might have probability p of emitting horizontally polarised light and probability $1 - p$ of emitting vertically polarised light. This cannot in general be described by a state vector as above; instead, we require an alternative description. Using the density matrix formalism allows for a full description of the state.

The density matrix of a pure state $|\psi\rangle$ is simply the outer product of the vector with itself: $\rho_{\mathrm{pure}} = |\psi\rangle\langle\psi|$. Accordingly, the density matrix of a mixed state is the sum of the density matrices of the constituent pure states, weighted by their probabilities:

$$\rho = \sum_{i} p_i |\psi_i\rangle\langle\psi_i|. \tag{1.6}$$

The density matrix has unit trace and is Hermitian and positive semi-definite.

For illustration, the density matrix describing the example above, a mixed state of $|H\rangle$ with probability p and $|V\rangle$ with probability $1 - p$, is

$$\begin{aligned} \rho &= p|H\rangle\langle H| + (1-p)|V\rangle\langle V| \\ &= \begin{pmatrix} p & 0 \\ 0 & 1-p \end{pmatrix}. \end{aligned} \tag{1.7}$$

It is clear that this cannot be represented as a pure state vector.

1.2　Entanglement

Entangled states are a particular class of multi-particle states that have very useful properties. Particles that are entangled share correlations that are far stronger than those encountered classically. Performing any measurement on one particle of a maximally entangled pair gives exact information about the result of an identical measurement on the other particle. These correlations promise powerful applications in many fields, including computing and communication. Entanglement allows for the possibility of faster and more efficient quantum computers, which have incredible potential to significantly outperform classical computers. It also allows for the possibility of highly secure communication, creating one-time pads that are shared by only the communicating parties and can be used to encrypt information in a way far more secure than current standards. Entangled states are integral to the work discussed in this thesis, and thus we will examine the mathematical concept of entanglement in order to understand the power it provides.

An entangled state cannot be separated into products of states. Conversely, a separable state can be described using a sum of products of states. Such a state, for example in a two-qubit space, can be written as

$$\rho = \sum_i p_i \rho_i^A \otimes \rho_i^B, \tag{1.8}$$

where p_i represents the probability of finding particle A in state ρ_i^A and particle B in state ρ_i^B. If a state cannot be written this way, then it is entangled [1]. In the case of pure states, this criterion reduces to a simpler form. A pure separable state can be written as the product of two pure states

$$|\psi\rangle = |\psi_1\rangle \otimes |\psi_2\rangle. \tag{1.9}$$

Otherwise, it is entangled.

An important class of entangled states are called the Bell states, named after John Bell as they will maximally violate inequalities he proposed to test the fundamentals of quantum mechanics [2]. One example of a Bell state is that where each single particle will always be found in the same state:

$$|\Phi^+\rangle = \frac{1}{\sqrt{2}}(|0,0\rangle + |1,1\rangle), \tag{1.10}$$

where we have used the notation $|i,j\rangle = |i\rangle \otimes |j\rangle$. As this state cannot be factored into the product of two states as in Eq. (1.9), it must be entangled.

The work in this thesis makes extensive use of entangled states. In Chapter 3, we use a source of polarisation-entangled photons in order to test causality in a quantum system. In Chapter 4, we use a source of orbital-angular-momentum–entangled photons in order to create single photons for use in a quantum protocol.

1.3   Quantum Operations

Quantum operations are the means by which quantum states are manipulated. They are tools for describing the evolution of a quantum system or the implementation of a process to change the state of a system; these concepts are central to any quantum protocol. As a result, a rudimentary understanding of quantum operations is necessary when performing any action on a quantum state – from basic quantum gates to generalised measurements.

The general concept is as follows: if the initial state of a system is ρ, then applying the operation $\mathcal{E}$ yields the final state $\rho' = \mathcal{E}(\rho)$. For example, a polarisation qubit might begin in the state $\rho = |H\rangle\langle H|$ and be subjected to a rotation $\mathcal{E}_{\mathrm{rot}}$ of its polarisation by $\pi/4$. The light then becomes diagonally polarised in the state $\rho' = \mathcal{E}_{\mathrm{rot}}(\rho) = |D\rangle\langle D|$. While this operation is quite simple, there are many different ways to represent it, each with its advantages and disadvantages; more complicated operations may lend themselves better to one representation or another depending on the context. Here we describe just one of these representations, which will be required to describe a process in Chapter 3.

1.3.1   Operator-Sum Representation

The first representation that we will discuss describes a quantum process as a sum of operators acting on an input state. Fittingly, this is called the operator-sum representation [3]. Any process $\mathcal{E}$ acting on a state ρ can be represented as

$$\mathcal{E}(\rho) = \sum_k E_k \rho E_k^\dagger, \tag{1.11}$$

where $\{E_k\}$ are operators that act on the state space of ρ.

The resultant matrix $\rho' = \mathcal{E}(\rho)$ must be a physical density matrix with unit trace such

that

$$1 = \text{Tr}(\mathcal{E}(\rho)) \tag{1.12}$$

$$= \text{Tr}\left(\sum_k E_k \rho E_k^\dagger\right) \tag{1.13}$$

$$= \sum_k \text{Tr}\left(E_k \rho E_k^\dagger\right) \tag{1.14}$$

$$= \sum_k \text{Tr}\left(E_k^\dagger E_k \rho\right) \tag{1.15}$$

$$= \text{Tr}\left(\sum_k E_k^\dagger E_k \rho\right). \tag{1.16}$$

From this, as $\text{Tr}(\rho) = 1$, we deduce that $\sum_k E_k^\dagger E_k = \mathbb{1}$. This is called the completeness relation and requires the map $\mathcal{E}$ to be trace-preserving.

To illustrate the operator-sum representation, let us consider the partial swap process $\mathcal{E}_p$ applied to a two-qubit state; this process will be instrumental in Chapter 3 of this thesis. The operation swaps the qubits some portion of the time, occurring with probability p, and leaves the qubits alone the remainder of the time, occurring with probability $1 - p$. The two operators can be written respectively as

$$E_1 = \sqrt{p}\, \text{SWAP} = \sqrt{p} \begin{pmatrix} 1 & 0 & 0 & 0 \\ 0 & 0 & 1 & 0 \\ 0 & 1 & 0 & 0 \\ 0 & 0 & 0 & 1 \end{pmatrix} \tag{1.17}$$

$$E_2 = \sqrt{1-p}\, \mathbb{1} = \sqrt{1-p} \begin{pmatrix} 1 & 0 & 0 & 0 \\ 0 & 1 & 0 & 0 \\ 0 & 0 & 1 & 0 \\ 0 & 0 & 0 & 1 \end{pmatrix}, \tag{1.18}$$

and our operator-sum representation is simply

$$\mathcal{E}_p(\rho) = E_1 \rho E_1^\dagger + E_2 \rho E_2^\dagger \tag{1.19}$$

$$= p\, \text{SWAP} \rho\, \text{SWAP} + (1 - p)\rho. \tag{1.20}$$

Additionally, we note that

$$E_1^\dagger E_1 \;=\; p \begin{pmatrix} 1 & 0 & 0 & 0 \\ 0 & 0 & 1 & 0 \\ 0 & 1 & 0 & 0 \\ 0 & 0 & 0 & 1 \end{pmatrix} \begin{pmatrix} 1 & 0 & 0 & 0 \\ 0 & 0 & 1 & 0 \\ 0 & 1 & 0 & 0 \\ 0 & 0 & 0 & 1 \end{pmatrix} = p\mathbb{1}, \tag{1.21}$$

$$E_2^\dagger E_2 \;=\; (1-p) \begin{pmatrix} 1 & 0 & 0 & 0 \\ 0 & 1 & 0 & 0 \\ 0 & 0 & 1 & 0 \\ 0 & 0 & 0 & 1 \end{pmatrix} \begin{pmatrix} 1 & 0 & 0 & 0 \\ 0 & 1 & 0 & 0 \\ 0 & 0 & 1 & 0 \\ 0 & 0 & 0 & 1 \end{pmatrix} = (1-p)\mathbb{1}, \tag{1.22}$$

so that

$$\sum_k E_k^\dagger E_k = p\mathbb{1} + (1-p)\mathbb{1} = \mathbb{1}. \tag{1.23}$$

1.4 Quantum Measurements

After encoding information in a quantum system, as with any system, we require a means by which to extract that information. We need to perform an operation that reads out data, which we can then use to make conclusions about the system. This means by which to extract data is called quantum measurement.

Measurement operations are a subclass of quantum operations, but we will discuss them in detail here as they are a very important subclass. First we will discuss the general mathematics of measurement. We will then discuss two special cases of measurements: projective measurements and positive operator-valued measures.

1.4.1 Generalised Measurements

A measurement in quantum mechanics [3] is defined as a set $\{M_m\}$ of measurement operators, each corresponding to an outcome m. The probability of outcome m occurring when measuring a system in the state ρ is given by

$$p(m) = \mathrm{Tr}(M_m \rho M_m^\dagger) = \mathrm{Tr}(M_m^\dagger M_m \rho). \tag{1.24}$$

After undergoing this measurement, the system will be in the state

$$\rho' = \frac{M_m \rho M_m^\dagger}{\mathrm{Tr}(M_m^\dagger M_m \rho)}. \tag{1.25}$$

Additionally, the operators must satisfy the completeness relation

$$\sum_m M_m^\dagger M_m = \mathbb{1}, \tag{1.26}$$

which ensures that one of the outcomes m must occur with certainty. As a consequence, the probabilities $p(m)$ must sum to unity.

1.4.2 Projective Measurements

A projective measurement [3] is a particular class of quantum measurements in which the operators M_m are projectors. A projector $\Pi_m = |m\rangle\langle m|$ projects a system into the state $|m\rangle$. This type of measurement is important as it is used often to obtain the probability of a particular outcome.

As projectors have the convenient property that $\Pi_m^\dagger \Pi_m = \Pi_m$, we can simplify the equations presented above. We can express an observable M using its spectral decomposition

$$M = \sum_m m\Pi_m, \tag{1.27}$$

where m is the eigenvalue corresponding to the eigenstate $|m\rangle$. The probability of outcome m occurring when measuring a system in the state ρ is given by

$$p(m) = \text{Tr}(\Pi_m \rho), \tag{1.28}$$

which reduces to $p(m) = |\langle m|\psi\rangle|^2$ if the state is pure.

After undergoing this measurement, the system will be in the state

$$\rho' = \frac{\Pi_m \rho \Pi_m^\dagger}{\text{Tr}(\Pi_m \rho \Pi_m^\dagger)} = \frac{|m\rangle\text{Tr}(\Pi_m \rho)\langle m|}{\text{Tr}(\Pi_m \rho)} = |m\rangle\langle m|. \tag{1.29}$$

In other words, the state has been projected into the pure state $|m\rangle$.

1.4.3 Positive Operator-Valued Measures

Another important class of measurements is called the positive operator-valued measure, or POVM. This type of measurement is often used when the final state of the system is not of interest. For example, rather than projecting into a state and using that state at a later

point in the experiment, one might simply be interested in the probability of projecting into that state. In this case, it is more straightforward to use the POVM description of measurements.

As per Eq. (1.24), a measurement on a state ρ with measurement operators $\{M_m\}$ produces outcome m with probability $p(m) = \text{Tr}(M_m^\dagger M_m \rho)$. We can define a POVM operator

$$E_m = M_m^\dagger M_m \tag{1.30}$$

so that the probability of outcome m is now $p(m) = \text{Tr}(E_m \rho)$.

It is important to note that, by their definition, POVM elements are necessarily positive semi-definite. Additionally, their trace must not exceed unity so that the probabilities they produce cannot also exceed unity.

Due to the completeness relation Eq. (1.26), the POVM operators must sum to the identity $\sum_m E_m = \mathbb{1}$. This tells us that our state must fall into one of the POVM outcomes. As a result, POVMs are particularly useful for determining which of several possible states a system was in.

To illustrate this, we will consider a simple example. Suppose that we would like to determine whether a photon was prepared in the state $|H\rangle$ or the state $|D\rangle = (|H\rangle + |V\rangle)/\sqrt{2}$. As these states are non-orthogonal, it is not possible to distinguish them perfectly [3]. We can, however, define a POVM that distinguishes them without error some of the time:

$$E_0 = \frac{\sqrt{2}}{1 + \sqrt{2}}|V\rangle\langle V| \tag{1.31a}$$

$$E_1 = \frac{\sqrt{2}}{1 + \sqrt{2}}|A\rangle\langle A| \tag{1.31b}$$

$$E_2 = \mathbb{1} - E_0 - E_1. \tag{1.31c}$$

As E_0 has an expectation value of zero with $|H\rangle$, a positive result in E_0 indicates that the state cannot have been $|H\rangle$; it must have been $|D\rangle$. Similarly, a positive result in E_1 indicates that the state must have been $|H\rangle$. A positive result in E_2, however, reveals no information about the system as $|H\rangle$ and $|D\rangle$ deliver equal, nonzero expectation values. Thus when we obtain a result in E_0 or E_1, we can be certain that we have correctly identified the state; the only downside is that sometimes we cannot make any conclusion about the state. This particular use of a POVM is often called unambiguous state discrimination and will return in Chapter 4.

1.5 Quantum State Tomography

It is often necessary to acquire a full description of the state of a system. For example, when creating an entangled state, it is important to confirm that the desired state has been successfully created. As the density matrix is a complete description of the state, it suffices to obtain full knowledge of this matrix.

The density matrix cannot typically be measured directly as any measurement can only return probabilities, which compose the diagonal of the matrix; all off-diagonal elements are not probabilities and thus are not as easily accessed in experiments. Instead, we must use reconstruction techniques, the most common of which is tomography [4].

Tomography is a technique used in many fields. Most people are familiar with the concept of tomographic medical imaging; for example, when one desires a three-dimensional image of the brain, one instead takes many images of different two-dimensional cross-sections of the brain and reconstructs the full image of the brain using the information obtained. Similarly, quantum tomography functions by taking many different measurements on identical copies of the state and reconstructing the density matrix using the probabilities obtained as measurement outcomes.

Specifically, the number of measurements required scales with the size of the density matrix, which is determined by the dimension of the system. For a state existing in a d-dimensional Hilbert space, the density matrix has d^2 elements. As the density matrix is Hermitian, implying that elements below the diagonal are simply complex conjugates of those above the diagonal, and positive semi-definite, implying that the elements on the diagonal are real and positive, this constitutes d^2 unknowns. This means that one requires d^2 measurements in order to completely determine the state. It is in theory possible to reduce this to $d^2 - 1$ unknowns as the matrix has unit trace, but in practice one must normalise the counts obtained in the experiment into probabilities, requiring an additional measurement to bring the total back up to d^2.

The d^2 measurements chosen must form an informationally complete set [5]. This means that the measurements must span the state space the density matrix occupies. In order to take the fewest measurements to accomplish this, we typically choose to take measurements from different bases that overlap minimally. These are called mutually unbiased bases; for a given dimension d, there are at most $d+1$ mutually unbiased bases [6, 7]. For polarisation, an example set of these bases has already been discussed briefly: the horizontal/vertical basis ($|H\rangle$, $|V\rangle$), the diagonal/anti-diagonal basis ($|D\rangle$, $|A\rangle$), and the right-/left-circular basis ($|R\rangle$, $|L\rangle$). For a two-dimensional polarisation state, we only strictly need four measurements; however, due to the fluctuations inherent in photon detection, it is common to

use all six in order to obtain better statistics.

A straightforward way to determine the density matrix of a system is by linear inversion [3]. However, there are two problems with this: Firstly, this method doesn't function when the number of measurements is larger than the number of degrees of freedom. Secondly, due to fluctuations in photon numbers, the probabilities obtained experimentally often lead to unphysical density matrices when calculated in this manner. Thus a more intelligent way to reconstruct the density matrix involves finding the physical matrix that best fits the data. There are many methods for performing this reconstruction; we will discuss only one such method as it is the one we choose to implement in Chapters 3 and 4.

1.5.1   Maximum Likelihood Estimation

Maximum likelihood estimation [5] is a common method for tomographically reconstructing the density matrix of a system. To produce a physical matrix, the method relies on the fact that any matrix ρ that can be described by another matrix T as $\rho = T^\dagger T$ is Hermitian and positive semi-definite. The only additional constraint for a physical matrix is that it must have unit trace. Thus we choose to parametrise our density matrix as

$$\rho = \frac{T^\dagger T}{\text{Tr}(T^\dagger T)}. \tag{1.32}$$

As we know a d-dimensional state has d^2 unknown parameters, we choose T to be a lower triangular matrix with real values on the diagonal. For example, for $d = 4$ (such as a two-qubit state), we choose $\vec{t} = \{t_1, t_2, ..., t_{16}\}$ such that

$$T = \begin{pmatrix} t_1 & 0 & 0 & 0 \\ t_5 + it_6 & t_2 & 0 & 0 \\ t_{11} + it_{12} & t_7 + it_8 & t_3 & 0 \\ t_{15} + it_{16} & t_{13} + it_{14} & t_9 + it_{10} & t_4 \end{pmatrix}. \tag{1.33}$$

Now given a set of detected counts $\{n_i\}$ and a set of measurements $\{\Pi_i\}$ performed to obtain those counts, we know the matrix we seek must satisfy

$$n_i = N\text{Tr}[\rho(\vec{t})\Pi_i], \tag{1.34}$$

where N is a constant that converts probabilities into counts. However, as mentioned above, fluctuations in counts prevent this equation from being exact; thus we must find the matrix ρ that has a maximal probability of producing the observed counts. We do this using a likelihood function.

Assuming that the noise on the measurements follows a Gaussian distribution, i.e, the expected standard deviation on n counts is approximately $\sqrt{n}$, the probability of obtaining the set of counts $\vec{n} = \{n_1, n_2, ..., n_{\max}\}$ from matrix $\rho(\vec{t})$ is

$$P(\vec{n}) = \frac{1}{C} \prod_i \exp\left[-\frac{N\mathrm{Tr}[\rho(\vec{t})\Pi_i] - n_i}{2N\mathrm{Tr}[\rho(\vec{t})\Pi_i]}\right]. \tag{1.35}$$

We seek to maximise this probability. To simplify this task, we can instead maximise the logarithm of this quantity; however, minimising functions is always more precise, so we can also choose to minimise the likelihood function [5]

$$\mathcal{L}(\vec{t}) = \sum_i \frac{\{N\mathrm{Tr}[\rho(\vec{t})\Pi_i] - n_i\}^2}{2N\mathrm{Tr}[\rho(\vec{t})\Pi_i]}. \tag{1.36}$$

The density matrix $\rho(\vec{t})$ that minimises this function is then the most likely state to have produced the observed counts.

1.6 Distance measures

Often we need to determine the proximity of a state to a desired state, for example, to determine whether we prepared the state we intended to. For this, we use several distance measures, two of which are discussed here. We use both throughout this thesis.

1.6.1 Fidelity

The fidelity between two quantum states ρ and σ is defined as

$$F = \left[\mathrm{Tr}\left(\sqrt{\sqrt{\rho}\sigma\sqrt{\rho}}\right)\right]^2. \tag{1.37}$$

The fidelity can range between 0 and 1. A fidelity of 1 or 100% indicates that ρ and σ are identical; a fidelity of 0 indicates that ρ and σ are orthogonal.

1.6.2 Trace distance

The trace distance between two quantum states ρ and σ is defined as

$$D = \frac{1}{2}\mathrm{Tr}\sqrt{(\rho - \sigma)^\dagger(\rho - \sigma)}. \tag{1.38}$$

The trace distance can range between 0 and 1. A trace distance of 0 indicates that ρ and σ are identical; a trace distance of 1 indicates that ρ and σ are orthogonal.

1.7 State Discrimination

The second experiment presented in this thesis concerns the discrimination of quantum states. The basic problem is the following: Alice would like to send information to Bob. They have agreed upon the use of two known states. Alice can send state $|\Psi_0\rangle$, conveying the bit "0", or she can send the state $|\Psi_1\rangle$, conveying the bit "1". Bob then requires some means of determining which state Alice has sent him in order to decode her message.

This task is easily accomplished when Alice uses orthogonal quantum states; however, if Alice must use non-orthogonal quantum states, the task becomes more difficult. In fact, unlike orthogonal states, non-orthogonal quantum states cannot be distinguished deterministically and without error as they have nonzero overlap. However, it is possible to devise a method of measurement that maximises Bob's ability to decode Alice's message.

There are several methods that can be used to maximise success in this task, but the two most common methods represent two extremes. The first extreme provides completely error-free discrimination but has a non-unit frequency of detection; this is called unambiguous state discrimination (USD) [8, 9, 10, 11, 12, 13, 14, 15, 16, 17, 18, 19, 20, 21]. The second extreme provides a unit detection frequency but allows errors to occur; this is called minimum-error state discrimination (MESD) [22]. In Chapter 4, we will see an experimental implementation of USD. As the experiment will also make use of some concepts in MESD, we present an introduction to both methods here.

1.7.1 Unambiguous State Discrimination

Unambiguous state discrimination aims to provide error-free discrimination of non-orthogonal quantum states. Intuitively, we can discuss Bob's "guess" at which state Alice has sent. In an error-free scheme such as USD, Bob's guess is always correct: if he thinks Alice has sent $|\Psi_0\rangle$, then he can be certain she has sent $|\Psi_0\rangle$. However, Bob must necessarily sacrifice frequency of detection: sometimes, he will not have a guess about the state. In this case, he receives an *inconclusive* result, and he obtains no information about what state Alice sent. As a result, USD provides either correct information about the state or inconclusive information.

In order to be certain that Alice sent a particular state, it suffices to know that she cannot have sent any of the other possible states. This was discussed briefly in Section 1.4.3, but we will review it here. Bob makes a measurement with two outcomes, M_0 and M_1. The state $|\Psi_0\rangle$ has zero probability of producing the outcome M_1; similarly, $|\Psi_1\rangle$ has zero probability of producing the outcome M_0. As a result, if Bob obtains outcome M_0, he can be certain Alice sent $|\Psi_0\rangle$; if he obtains outcome M_1, he can be certain Alice sent $|\Psi_1\rangle$.

USD in Two Dimensions

We will discuss the specific example of discriminating two pure two-dimensional states, using polarisation as our basis. The states we will discriminate are separated by some angle 2α as shown in Fig. 1.1 and are given by

$$
\begin{align}
|\Psi_0\rangle &= \cos\alpha\,|H\rangle + \sin\alpha\,|V\rangle \tag{1.39a}\\
|\Psi_1\rangle &= \cos\alpha\,|H\rangle - \sin\alpha\,|V\rangle. \tag{1.39b}
\end{align}
$$

We seek a POVM element E_0 such that $\langle\Psi_1|E_0|\Psi_1\rangle = 0$. The simplest such operator is the projector of the state orthogonal to $|\Psi_1\rangle$. The orthogonal state $|\Psi_1^\perp\rangle$ is simply $|\Psi_1\rangle$ rotated by $\pi/2$:

$$
|\Psi_1^\perp\rangle = \sin\alpha\,|H\rangle + \cos\alpha\,|V\rangle. \tag{1.40}
$$

The POVM element is then

$$
E_0 = q\begin{pmatrix} \sin^2\alpha & \cos\alpha\sin\alpha \\ \cos\alpha\sin\alpha & \cos^2\alpha \end{pmatrix}, \tag{1.41}
$$

where we have included a constant factor q that will be useful momentarily.

In a similar fashion, we can find a POVM element E_1 such that $\langle\Psi_0|E_1|\Psi_0\rangle = 0$, given by

$$
E_1 = q\begin{pmatrix} \sin^2\alpha & -\cos\alpha\sin\alpha \\ -\cos\alpha\sin\alpha & \cos^2\alpha \end{pmatrix}, \tag{1.42}
$$

with the same coefficient q, as we would like our probabilities for detecting $|\Psi_0\rangle$ and $|\Psi_1\rangle$ to be equal.

Recall that POVM elements must have trace ≤ 1 so that the probabilities resulting from them cannot exceed unity. As a result, q cannot exceed unity and thus $E_0 + E_1 \neq \mathbb{1}$. We require a third element $E_?$ to complete the POVM. We define

$$
E_? = \mathbb{1} - E_0 - E_1 = \begin{pmatrix} 1 - 2q\sin^2\alpha & 0 \\ 0 & 1 - 2q\cos^2\alpha \end{pmatrix}. \tag{1.43}
$$

This element corresponds to an inconlusive result; obtaining outcome $E_?$ provides no information about the state.

Now to determine q, we use the requirement that POVM elements be positive semidefinite. The eigenvalues of $E_?$ are simply the diagonal elements. We require both to be nonnegative; this can be accomplished by solving for the value of q that makes one zero and the other positive. We find

$$q = \frac{\sec^2\alpha}{2}. \tag{1.44}$$

Finally, we obtain the full POVM

$$E_0 = \frac{1}{2}\begin{pmatrix} \tan^2\alpha & -\tan\alpha \\ -\tan\alpha & 1 \end{pmatrix} \tag{1.45a}$$

$$E_1 = \frac{1}{2}\begin{pmatrix} \tan^2\alpha & \tan\alpha \\ \tan\alpha & 1 \end{pmatrix} \tag{1.45b}$$

$$E_? = \begin{pmatrix} 1-\tan^2\alpha & 0 \\ 0 & 0 \end{pmatrix}. \tag{1.45c}$$

The probability of successfully identifying a state is $2\sin^2\alpha$. The probability of an inconclusive result is $\cos(2\alpha)$, which is exactly equal to the overlap of the states $|\langle\Psi_0|\Psi_1\rangle|$ [9, 10].

Experimental Implementation of USD

Implementing the POVM (1.45) is not as straightforward as it might seem. Experimentally, it is difficult to perform three projective measurements simultaneously in a two-dimensional state space; one requires an additional degree of freedom so that the state space becomes three-dimensional. This method was used on polarisation states of the form (1.39) in the first experimental implementation of USD [23], which we will discuss briefly here.

To implement the POVM (1.45), we need to orthogonalise the states. It is possible to orthogonalise the states by attenuating one basis state, as illustrated in Fig. 1.1. To this end, another degree of freedom is introduced, for example, two different paths the light can take, $|1\rangle$ and $|2\rangle$. By taking some amplitude from the $|H\rangle$ state in path 1 and placing it in path 2, we effectively attenuate the $|H\rangle$ state, thereby orthogonalising what is left in path 1. The states then become

$$|\Psi_0'\rangle = \sin\alpha\,(|H\rangle + |V\rangle)\otimes|1\rangle + \sqrt{\cos(2\alpha)}|H\rangle\otimes|2\rangle \tag{1.46a}$$

$$|\Psi_1'\rangle = \sin\alpha\,(|H\rangle - |V\rangle)\otimes|1\rangle + \sqrt{\cos(2\alpha)}|H\rangle\otimes|2\rangle. \tag{1.46b}$$
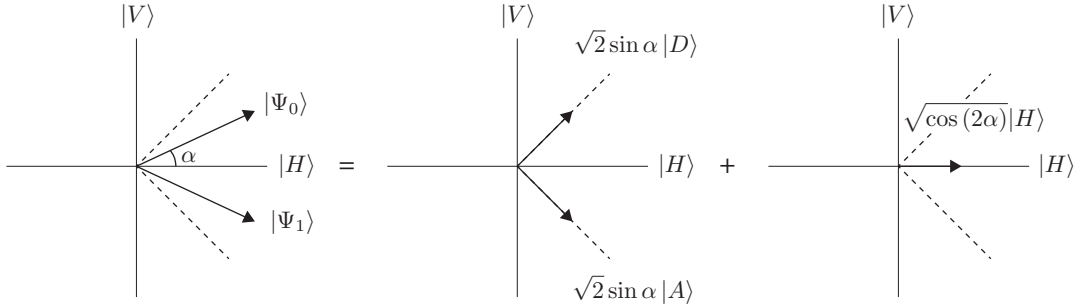
Figure 1.1: Non-orthogonal states can be orthogonalised by attenuating the $|H\rangle$ component.

Thus, looking only at path 1, we obtain the states $|D\rangle = (|H\rangle + |V\rangle)/\sqrt{2}$ and $|A\rangle = (|H\rangle - |V\rangle)/\sqrt{2}$. As these states are orthogonal, it is straightforward to perform a measurement to distinguish the two. This opportunity to unambiguously discriminate the states occurs with probability $2\sin^2\alpha$. On the other hand, looking only at path 2, we obtain a probability $\cos(2\alpha)$ of receiving no information about what the state was; this corresponds to an inconclusive result. These probabilities match exactly those produced by the POVM (1.45).

1.7.2 Minimum-Error State Discrimination

Minimum-error state discrimination aims to provide frequent, though not error-free, discrimination of non-orthogonal quantum states. In this scheme, Bob always has a guess about which state Alice sent. However, Bob must necessarily sacrifice certainty: his guess will be incorrect a known percentage of the time. We will demonstrate how to find the detection operators for two-dimensional MESD, as well as the probability of error that results from it.

Bob must choose a POVM of two detection operators, D_0 to detect the state $|\Psi_0\rangle$ and D_1 to detect the state $|\Psi_1\rangle$, that will minimise his probability of obtaining an incorrect result. We also assume that Alice chooses which state to send based on *a priori* probabilities η_0 and η_1. The probability of an incorrect result or error is then given by [24]

$$P_{\text{err}} = \eta_0 \text{Tr}(\rho_0 D_1) + \eta_1 \text{Tr}(\rho_1 D_0), \tag{1.47}$$

where ρ_i is the density matrix for state $|\Psi_i\rangle$. It will become clear momentarily that it is

16

helpful to express this probability using a new operator $\Lambda = \eta_1\rho_1 - \eta_0\rho_0$ so that

$$
\begin{aligned}
P_{\text{err}} &= \eta_0 \operatorname{Tr}(\rho_0 D_1) + \eta_1 \operatorname{Tr}\left(\frac{\Lambda + \eta_0\rho_0}{\eta_1} D_0\right) && (1.48)\\
&= \eta_0 \operatorname{Tr}[\rho_0(D_0 + D_1)] + \operatorname{Tr}(\Lambda D_0) && (1.49)\\
&= \eta_0 + \operatorname{Tr}(\Lambda D_0) && (1.50)
\end{aligned}
$$

since $D_0 + D_1 = \mathbb{1}$. Similarly, one can also write $P_{\text{err}} = \eta_1 - \operatorname{Tr}(\Lambda D_1)$.

Now we choose to write Λ in terms of its spectral decomposition with eigenvectors $|\phi_k\rangle$ with eigenvalues λ_k:

$$
\Lambda = \sum_{k=1}^{d} \lambda_k |\phi_k\rangle\langle\phi_k|. \tag{1.51}
$$

Then we can write the probability of error as

$$
P_{\text{err}} = \eta_0 + \sum_{k} \lambda_k \langle\phi_k|D_0|\phi_k\rangle. \tag{1.52}
$$

In order to minimise this quantity, we would like for the second term to be negative. Thus we desire D_0 such that $\langle\phi_k|D_0|\phi_k\rangle = 0$ for positive eigenvalues and $\langle\phi_k|D_0|\phi_k\rangle = 1$ for negative eigenvalues.

Examining the expression for the probability of error in terms of D_1, we find

$$
P_{\text{err}} = \eta_1 - \sum_{k} \lambda_k \langle\phi_k|D_1|\phi_k\rangle, \tag{1.53}
$$

so we would like for the second term to be positive in this case. Thus we desire D_1 such that $\langle\phi_k|D_1|\phi_k\rangle = 0$ for negative eigenvalues and $\langle\phi_k|D_1|\phi_k\rangle = 1$ for positive eigenvalues.

Thus we define our operators to be

$$
\begin{aligned}
D_0 &= \sum_{k=1}^{k_0} |\phi_k\rangle\langle\phi_k| && (1.54\text{a})\\
D_1 &= \sum_{k_0+1}^{d} |\phi_k\rangle\langle\phi_k|, && (1.54\text{b})
\end{aligned}
$$

where we have ordered the eigenvectors for convenience such that the first k_0 of them have negative eigenvalues and the remainder have nonnegative eigenvalues. These are then the operators that distinguish ρ_0 and ρ_1 with minimum error.

17

Example

For the example of the states described by Eq. (1.39) with equal probability of occurrence $\eta_0 = \eta_1 = 1/2$, we have

$$\Lambda = \begin{pmatrix} 0 & -\cos\alpha\sin\alpha \\ -\cos\alpha\sin\alpha & 0 \end{pmatrix}, \tag{1.55}$$

which has eigenvalues and eigenvectors

$$\lambda_1 = -\cos\alpha\sin\alpha \quad , \quad |\phi_1\rangle = \frac{1}{\sqrt{2}}\left(|H\rangle + |V\rangle\right) \tag{1.56a}$$

$$\lambda_2 = \cos\alpha\sin\alpha \quad , \quad |\phi_2\rangle = \frac{1}{\sqrt{2}}\left(|H\rangle - |V\rangle\right). \tag{1.56b}$$

Since $\cos\alpha\sin\alpha$ is always positive for the region of interest $0 \le \alpha \le \pi/4$, we can create our two operators

$$D_0 = |\phi_1\rangle\langle\phi_1| = \frac{1}{2}\begin{pmatrix} 1 & 1 \\ 1 & 1 \end{pmatrix} \tag{1.57a}$$

$$D_1 = |\phi_2\rangle\langle\phi_2| = \frac{1}{2}\begin{pmatrix} 1 & -1 \\ -1 & 1 \end{pmatrix}. \tag{1.57b}$$

Error Bound

We have found the operators that produce the minimum error, but we can also find an expression for what that minimum error is. Taking the sum of Eqs. (1.52) and (1.53) with these expressions for D_0 and D_1, we obtain

$$P_{\mathrm{err}} = \frac{1}{2}(1 - \sum_k |\lambda_k|) = \frac{1}{2}(1 - \mathrm{Tr}|\Lambda|), \tag{1.58}$$

where $|\Lambda| = \sqrt{\Lambda^\dagger \Lambda}$. Since $\Lambda = \eta_1\rho_1 - \eta_0\rho_0$, we find the final result for the probability of error using minimum-error state discrimination, also known as the Helstrom bound [22, 24]:

$$P_{\mathrm{err}} = \frac{1}{2}(1 - \mathrm{Tr}|\eta_1\rho_1 - \eta_0\rho_0|). \tag{1.59}$$

It is with this bound that the merit of experimental implementations of USD is determined. USD promises in theory no errors, but due to unavoidable dark counts in experiments, there

will always be some error in practical applications. Typically this error is compared to the bound for MESD, and if the error from USD is below, then it can be seen as a useful implementation. In Chapter 4, we will revisit error bounds in MESD and derive a bound for higher dimensions in order to confirm the results of a high-dimensional USD experiment.

Chapter 2

Experimental Techniques

Quantum information applications in optics require many different experimental techniques. This work makes use of several key techniques including measurement of states encoded in specific degrees of freedom of light, generation of entangled states encoded in these degrees of freedom, and the generation of heralded single photons from such entanglement. In this chapter, we will discuss these techniques and how they are implemented.

2.1 Measuring States

An integral part of any experiment is measurement; we need to be able to obtain data from the experiment to understand what occurred and why. In quantum optics, this means using photon detectors to determine the number of photons passing through a projective measurement operation during a particular timespan. These photon counts are then converted to probabilities in order to analyse the data. In this work, we use two different degrees of freedom of light, polarisation and orbital angular momentum, each with its own measurement technique.

2.1.1 Measuring Polarisation

Any polarisation projective measurement can be accomplished using three optical elements: a polarising beamsplitter (PBS), a half-wave plate (HWP), and a quarter-wave plate (QWP).

A polarising beamsplitter couples two polarisation basis states (typically horizontal $|H\rangle$ and vertical $|V\rangle$) to the spatial degree of freedom. The horizontally polarised light continues through the beamsplitter, whilst the vertically polarised light reflects at $90°$. This makes measurement in an orthogonal basis extremely simple by detecting the light in each path individually. This provides the additional advantage of leaving both basis states intact: it is then possible to perform not only a projective measurement but also a generalised measurement of both basis states.

With only a polarising beamsplitter, it is difficult to measure in more than one basis. Thus it is helpful to use wave plates in order to rotate the measurement basis. A half-wave plate placed at an angle θ from the horizontal acts on a polarisation qubit in the following way:

$$\begin{pmatrix} a' \\ b' \end{pmatrix} = \begin{pmatrix} \cos(2\theta) & \sin(2\theta) \\ \sin(2\theta) & -\cos(2\theta) \end{pmatrix} \begin{pmatrix} a \\ b \end{pmatrix}. \tag{2.1}$$

Thus with a half-wave plate, it is possible to access states with real phase between $|H\rangle$ and $|V\rangle$; for example, a half-wave plate allows access to the $\{|D\rangle, |A\rangle\}$ basis using $\theta = \pm\pi/4$.

A quarter-wave plate placed at an angle ϕ from the horizontal acts on a polarisation qubit in the following way:

$$\begin{pmatrix} a' \\ b' \end{pmatrix} = \begin{pmatrix} 1 + i\cos(2\phi) & i\sin(2\phi) \\ i\sin(2\phi) & 1 - i\cos(2\phi) \end{pmatrix} \begin{pmatrix} a \\ b \end{pmatrix}. \tag{2.2}$$

Thus a quarter-wave plate provides the additional capability to access states with imaginary phase between $|H\rangle$ and $|V\rangle$; for example, a quarter-wave plate allows access to the $\{|R\rangle, |L\rangle\}$ basis using $\theta = 0$ and $\phi = \pm\pi/4$. Using the combination of one half- and one quarter-wave plate followed by a polarising beamsplitter, it is possible to measure any basis of polarisation.

2.1.2 Measuring Orbital Angular Momentum

Due to the infinite-dimensional space of orbital angular momentum, measurement of this degree of freedom is not quite as straightforward. Orbital angular momentum is distinguished by its helical phase fronts. A plane wave has a flat phase front in its propagation direction, but if a cross-section is taken at an angle, the phase will increase from one side of the cross-section to the other. The frequency at which the increasing phase goes through 2π, i.e., the frequency of phase cycles, indicates the angle of propagation, as seen in Fig. 2.1(a). Similarly, a Gaussian beam ($\ell = 0$) has a flat phase front, but light with nonzero OAM will have phase increasing in the clockwise direction. This time the number
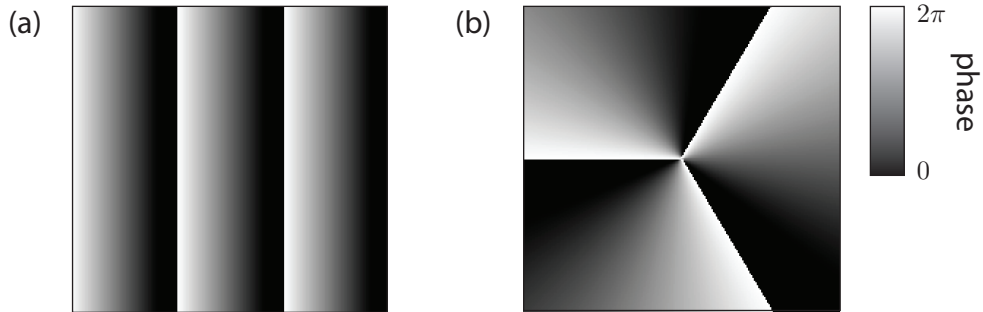
Figure 2.1: Phase of (a) a plane wave at an angle and (b) an OAM mode ($\ell = 3$).
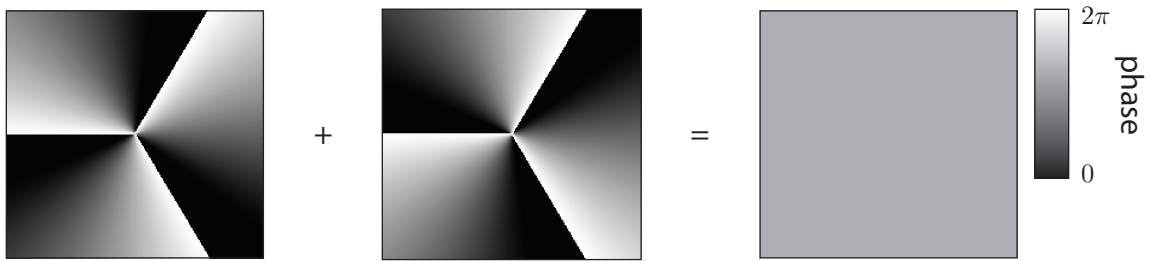
Figure 2.2: Measurement using an SLM. The phase of the hologram on the SLM is added to the phase of the OAM mode. If the two are equal and opposite, as in this case ($\ell_{\mathrm{OAM}} = 3$ and $\ell_{\mathrm{SLM}} = -3$), they cancel out to become the Gaussian mode ($\ell = 0$), which has a flat phase front.

of phase cycles indicates the OAM value of the light; one cycle indicates an OAM of $\hbar$, two cycles indicate an OAM of $2\hbar$, and so on. Phase increasing in the anticlockwise direction indicates a negative OAM value. An example of an OAM phase front is shown in Fig. 2.1(b).

The equivalent of a polarising beamsplitter for orbital angular momentum is called an OAM mode sorter [25, 26]; however, the mode sorter doesn't afford the versatility of different bases that a polarising beamsplitter affords for polarisation as the equivalent of half- and quarter-wave plates for OAM do not exist. As a result, it is more common to use projective measurements to measure OAM.

Projective measurements can be performed by first noting that a single-mode fibre accepts only light with an OAM value of $\ell = 0$. Thus by "flattening" the phase front of the desired light into an $\ell = 0$ mode, it is possible to couple only the desired light into the fibre and subsequently detect it. This flattening can be performed by placing in the beam a phase-inducing material whose phase increases azimuthally. This can be accomplished using a spatial light modulator (SLM) as shown in Fig. 2.2. An SLM is a liquid crystal

display in which each pixel can be programmed to have a different phase. Any phase pattern can be displayed on the SLM; for example, if an $\ell = 3$ phase pattern is displayed, then light with OAM $\ell = -3$ will be transformed into an $\ell = 0$ mode. Additionally, superpositions of OAM modes can be displayed on the SLM. Thus combining the SLM with a single-mode fibre allows for any projective measurement of any OAM mode or superposition to be performed.

2.2   Generating Entanglement

Generating entanglement is one of the most important technologies in quantum information. In optics, this typically involves a nonlinear process called spontaneous parametric downconversion (SPDC) [27, 28, 29]. This process can occur when light is incident on a nonlinear crystal. Infrequently (with probability 10^{-6} to 10^{-12} per photon), a photon from the pump will "downconvert" to two photons of lower frequency. The two downconverted photons are referred to as the *signal* and the *idler*. To conserve energy, their frequencies must sum to the pump photon frequency. We will briefly treat the mathematical derivation of SPDC here.

We can express the quantised field of the pump photon with wave vector $\mathbf{k}_p$ and frequency ω_p as

$$E_p^{(+)} = i\sqrt{\frac{\hbar\omega_p}{2\epsilon_0 V}} a_p e^{i(\mathbf{k}_p \cdot \mathbf{r} - \omega_p t)}, \tag{2.3}$$

for crystal interaction volume V. Here we have introduced the annihilation operator a_p. The expression for the signal and idler fields are identical save the index p. The complex conjugate of the above operator is $E_p^{(-)}$. Now we are able to write the interaction Hamiltonian for the process of SPDC [30, 31] as

$$H = -\frac{\epsilon_0}{3}\chi^{(2)}\int_V dV \left(E_s^{(-)}E_i^{(-)}E_p^{(+)} + E_p^{(-)}E_s^{(+)}E_i^{(+)}\right), \tag{2.4}$$

where $\chi^{(2)}$ is the second-order nonlinearity, a parameter of the crystal. Now we can use this Hamiltonian to determine the evolution of the input state, which we will take to be a coherent state as the pump beam and the vacuum state in the signal and idler modes $|\alpha\rangle_p|0\rangle_s|0\rangle_i$. Over the interaction time t, we obtain the state

$$
\begin{aligned}
|\psi\rangle &= e^{-iHt/\hbar}|\alpha\rangle_p|0\rangle_s|0\rangle_i \\
&= |\alpha\rangle_p|0\rangle_s|0\rangle_i + \frac{i\epsilon_0 t}{3\hbar}\chi^{(2)}\int_0^t dt' \int_V dV E_s^{(-)}E_i^{(-)}E_p^{(+)}|\alpha\rangle_p|0\rangle_s|0\rangle_i + ... \tag{2.5}
\end{aligned}
$$

23

We note that we have neglected higher-order terms, and the $E_p^{(-)}E_s^{(+)}E_i^{(+)}$ term in the first order does not contribute as the signal and idler annihilate the vacuum state. In the remainder of this section, we will also ignore the zeroth-order term as it is not of interest, and we will instead look only at the first-order term. We can now substitute the expressions of the electric fields and, ignoring the constant coefficient in front that results, we obtain

$$
\begin{aligned}
|\psi\rangle \quad \propto \quad & \int_0^t dt' \int_V dV \exp\left[i(\mathbf{k}_p{\cdot}\mathbf{r} - \omega_p t') - i(\mathbf{k}_p{\cdot}\mathbf{r} - \omega_s t') - i(\mathbf{k}_p{\cdot}\mathbf{r} - \omega_i t')\right] a_p a_s^\dagger a_i^\dagger |\alpha\rangle_p |0\rangle_s |0\rangle_i \\
= \quad & \alpha \int_0^t dt' \int_V dV \exp\left[i(\mathbf{k}_p - \mathbf{k}_s - \mathbf{k}_i){\cdot}\mathbf{r}\right] \exp\left[-i(\omega_p - \omega_s - \omega_i)t'\right] |\alpha\rangle_p |1\rangle_s |1\rangle_i. \quad (2.6)
\end{aligned}
$$

To complete the first integral, we assume a long interaction time t in comparison to the frequencies and obtain

$$
\int_0^t dt' \exp\left[-i(\omega_p - \omega_s - \omega_i)t'\right] = 2\pi\delta(\omega_s + \omega_i - \omega_p). \quad (2.7)
$$

This enforces energy conservation: the signal and idler frequencies must sum to the pump frequency $\omega_p = \omega_s + \omega_i$.

To complete the second integral, also known as the phase-matching term, we examine one dimension, which will generalise to the other two dimensions. If the length of the crystal in the z direction is L_z, and introducing the phase mismatch $\Delta k = k_p - k_s - k_i$, we have

$$
\begin{aligned}
\int_0^{L_z} dz\, e^{i\Delta k_z z} \quad = \quad & \frac{i}{\Delta k_z}(1 - e^{i\Delta k_z L_z}) \\
= \quad & e^{i\Delta k_z L_z/2} L_z \mathrm{sinc}\left(\frac{\Delta k_z L_z}{2}\right). \quad (2.8)
\end{aligned}
$$

The phase-matching term is then a product of three sinc functions.

We note that when the phase mismatch Δk is zero, the phase-matching term is maximised. Several techniques exist to minimise the mismatch. Tuning the angle of a crystal such as BBO can reduce the mismatch; however, the signal and idler are then no longer collinear, which reduces the efficiency of the process. Adjusting the temperature of a crystal such as KTP can also reduce the mismatch; additionally, however, *periodic poling* can be used to create a periodically poled KTP (ppKTP) crystal [32].

Periodic poling is a technique that can be implemented in ferromagnetic materials in order to make the $\chi^{(2)}$ of the material periodic in z. This is desirable to reduce the phase

walkoff occurring naturally in the crystal. Creating a $\chi^{(2)}$ whose orientation flips with period Λ as

$$\chi^{(2)}(z) = \chi_0^{(2)} \operatorname{sign}\left[\cos\left(\frac{2\pi z}{\Lambda}\right)\right] \tag{2.9}$$

results in a modified phase mismatch [32]

$$\Delta k = k_p - k_s - k_i \pm \frac{2\pi}{\Lambda}. \tag{2.10}$$

Thus any initial phase mismatch can be mitigated with the selection of an appropriate poling period Λ, keeping the light in phase and increasing the downconversion efficiency.

2.2.1 Generating OAM Entanglement

In Chapter 4, we use a BBO crystal to implement downconversion resulting in entanglement in the orbital angular momentum degree of freedom. Due to conservation of momentum, the downconverted photons must have orbital angular momenta summing to the OAM of the pump photon. Typically, the crystal is pumped with a Gaussian mode, and thus the OAM of the signal ℓ_s and that of the idler ℓ_i must be equal and opposite such that $\ell_s = -\ell_i$. In fact, the photons are in a superposition of all possible ℓ-values that satisfy this criterion. As a result, not only are the orbital angular momenta of the downconverted photons correlated, but they are also entangled [33]. The form of the entanglement is

$$|\Psi\rangle = \sum_{\ell=-\infty}^{\infty} c_\ell |\ell\rangle_i \otimes |-\ell\rangle_s, \tag{2.11}$$

where $|c_\ell|^2$ represents the probability of finding the idler photon with OAM $\ell\hbar$ and the signal photon with OAM $-\ell\hbar$, as shown in Fig. 2.3(a).

The distribution of $|c_\ell|^2$ is referred to as the *spiral bandwidth* [34, 35]. In theory, OAM entanglement exists in an infinite number of OAM modes and thus is infinite-dimensional; however, in practice, the spiral bandwidth is limited by several factors. These factors will not be discussed in depth here as they are not of direct consequence to the work herein, but they include the pump beam waist and the phase-matching of the crystal [34, 35]. An example of a typical spiral bandwidth as shown in Ref. [34] is shown in Fig. 2.3(b).

(a)

(b)

ℓ

$-\ell$

probability $|c_\ell|^2$

0.4

0.3

0.2

0.1

0.0

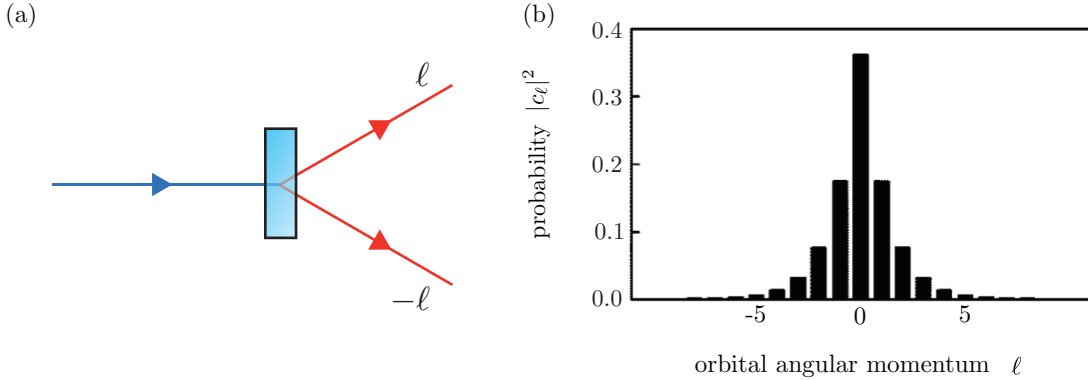-5

0

5

orbital angular momentum ℓ

Figure 2.3: **Orbital angular momentum entanglement.** (a) Light with OAM $\ell = 0$ strikes a crystal and downconverts to two entangled photons with OAM ℓ and $-\ell$. (b) A typical spiral bandwidth [34].

2.2.2   Generating Polarisation Entanglement

The generation of photon pairs entangled in the polarisation degree of freedom also uses SPDC, but typically additional optics are used in order to obtain high rates of production. There are many ways in which to do this, but we will treat only the method used in this thesis, which is based on a Sagnac interferometer [28, 29, 36]. This setup will hereafter be referred to as the Sagnac source.

The setup of the Sagnac source is shown in Fig. 2.4. The interferometer is pumped with a 10-mW continuous-wave laser at wavelength 405 nm. The polarisation is rotated to diagonal polarisation prior to the interferometer using a half-wave plate. The light is then focussed into a polarising beamsplitter, which separates the horizontal and vertical components to travel in different directions around the Sagnac interferometer.

Within the interferometer is a 10-mm periodically poled KTP (ppKTP) crystal phase-matched for type-II downconversion. A type-II crystal produces two orthogonally polarised photons; the crystal we use downconverts only horizontally polarised incident light, creating one horizontal and one vertical photon. Thus the vertically polarised light (propagating anticlockwise) first encounters a half-wave plate to rotate its polarisation to horizontal. It then strikes the crystal, and the downconverted photons propagate to the polarising beamsplitter. The vertical one reflects into mode 1, and the horizontal one is transmitted and reflects off a dichroic mirror into mode 2.

The clockwise (horizontally polarised) direction strikes the same crystal and downconverts to one horizontal and one vertical photon. Just prior to re-entering the polarising beamsplitter, the polarisations are (inconsequentially) swapped in the half-wave plate. The
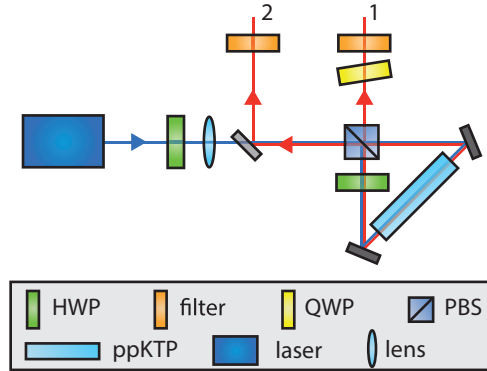
Figure 2.4: **Source of polarisation-entangled photon pairs.** Downconverted photons are created by pumping a ppKTP crystal in either direction within a Sagnac interferometer. The photons are entangled in modes 1 and 2 after encountering a polarising beamsplitter.

horizontal one is transmitted through the PBS into mode 1, and the vertical one is reflected by the PBS and the dichroic mirror into mode 2.

There is uncertainty as to which polarisation is in which mode: if the clockwise direction downconverted, mode 1 will contain a horizontally polarised photon, but if the anticlockwise direction downconverted, mode 1 will contain a vertically polarised photon. As a result, the photons are entangled in the Bell state

$$|\Psi^+\rangle = \frac{1}{\sqrt{2}}\left(|HV\rangle + |VH\rangle\right), \tag{2.12}$$

where $|ab\rangle = |a\rangle_1 \otimes |b\rangle_2$. By tilting a quarter-wave plate placed in mode 1, it is possible to change the phase to produce the Bell state

$$|\Psi^-\rangle = \frac{1}{\sqrt{2}}\left(|HV\rangle - |VH\rangle\right), \tag{2.13}$$

or indeed any state with phase ϕ of the form $\left(|HV\rangle - e^{i\phi}|VH\rangle\right)/\sqrt{2}$.

Polarisation controllers after coupling the photons into fibre make it possible to also produce any state of the form $\left(|HH\rangle - e^{i\phi}|VV\rangle\right)/\sqrt{2}$, in particular the two Bell states

$$|\Phi^-\rangle = \frac{1}{\sqrt{2}}\left(|HH\rangle - |VV\rangle\right), \tag{2.14}$$

$$|\Phi^+\rangle = \frac{1}{\sqrt{2}}\left(|HH\rangle + |VV\rangle\right). \tag{2.15}$$

It is the latter state that we choose to use in Chapter 3 of this thesis.

2.3 Generating Single Photons from Entanglement

In Chapter 4 of this thesis, we require the ability to produce single photons prepared in the spatial state of our choosing. We do this using remote state preparation [37, 38] on photons entangled in their orbital angular momentum.

We would like to prepare the signal photon in the state $|\psi\rangle$. We define a corresponding "reverse conjugate" state $|\psi\rangle_{\text{conj}}$ wherein the signs of the ℓ-values are reversed and the coefficient of each ℓ-value is conjugated. That is, if

$$|\psi\rangle = \sum_\ell a_\ell |\ell\rangle \tag{2.16}$$

then

$$|\psi\rangle_{\text{conj}} = \sum_\ell a_\ell^* |-\ell\rangle. \tag{2.17}$$

In order to remotely prepare a state in the signal photon, we must make a measurement of the idler photon. We use an SLM combined with a single-mode fibre to complete this measurement. On the SLM, we display the hologram corresponding to the state $|\psi\rangle$. As an SLM turns the reverse conjugate state of its hologram into the Gaussian mode, any photon that is accepted into the single mode fibre must then have been in the reverse conjugate state $|\psi\rangle_{\text{conj}}$. Displaying a hologram of $|\psi\rangle$ then performs a projective measurement of the state $|\psi\rangle_{\text{conj}}$.

Applying this measurement to the overall entangled state $|\Psi\rangle$ of Eq. (2.11), we obtain

$$
\begin{aligned}
\left(|\psi\rangle_{\text{conj},i} \langle\psi|_{\text{conj},i} \otimes \mathbb{1}_s \right) |\Psi\rangle &= \left(\sum_j a_j^* |-j\rangle_i \sum_k a_k \langle -k|_i \otimes \mathbb{1}_s \right) \left(\sum_\ell c_\ell |\ell\rangle_i \otimes |-\ell\rangle_s \right) \\
&= \sum_j \sum_k \sum_\ell c_\ell a_j^* a_k |-j\rangle_i \delta_{-k,\ell} \otimes |-\ell\rangle_s \\
&= \sum_j \sum_k c_{-k} a_j^* a_k |-j\rangle_i \otimes |k\rangle_s \\
&= \sum_j a_j^* |-j\rangle_i \otimes \sum_k c_{-k} a_k |k\rangle_s.
\end{aligned} \tag{2.18}
$$

If the spiral bandwidth is uniformly distributed, that is, if c_ℓ is a constant for all ℓ, the overall state reduces to

$$|\psi\rangle_{\text{conj},i} \otimes |\psi\rangle_s. \tag{2.19}$$

Thus, ignoring the spiral bandwidth (as we will deal with it momentarily), we see that displaying a hologram corresponding to the state $|\psi\rangle$ on one of the SLMs yields the state $|\psi\rangle$ in the other photon. As a result, by using coincidences between the signal and idler as confirmation, we are able to successfully remotely prepare any single-photon state in the signal arm. In this way, the idler photon acts as a herald.

Entanglement Concentration for OAM Modes

The remote state preparation shown in Eq. (2.19) requires a uniformly distributed spiral bandwidth, that is, a state in which the probabilities of production $|c_\ell|^2$ are equal. Otherwise, the state of the signal would become

$$\sum_\ell a_\ell^* c_\ell | - \ell\rangle_s \neq |\psi\rangle_{\text{conj},s}. \tag{2.20}$$

As the probabilities $|c_\ell|^2$ are not generally equal, it is necessary to "flatten" the spiral bandwidth to a uniform distribution. This can be accomplished by reducing the efficiency of the detection optics and is referred to as entanglement concentration [39].

The modification of the spiral bandwidth can be accomplished by attenuating certain OAM modes such that all states of interest have equal probability. This can be done by adjusting the holograms projected onto the SLMs. It can be done with both SLMs or just one; we use only the idler arm to perform this adjustment. It functions as follows.

We must apply an ℓ-dependent multiplier b_ℓ to each OAM mode displayed on the SLM in the idler arm so that the state of the idler becomes $|\psi\rangle_{\text{conj},i}^{\text{SB}} = \sum_\ell b_\ell a_\ell |\ell\rangle_i$. Thus the entire state of the system is

$$
\begin{aligned}
\left(|\psi\rangle_{\text{conj},i}^{\text{SB}} \langle\psi|_{\text{conj},i}^{\text{SB}} \otimes \mathbb{1}_s \right) |\Psi\rangle &= \left(\sum_j b_j^* a_j^* | - j\rangle_i \sum_k b_k a_k \langle -k|_i \otimes \mathbb{1}_s \right) \left(\sum_\ell c_\ell |\ell\rangle_i \otimes | - \ell\rangle_s \right) \\
&= \sum_j \sum_k \sum_\ell c_\ell b_j^* a_j^* b_k a_k | - j\rangle_i \delta_{-k,\ell} \otimes | - \ell\rangle_s \\
&= \sum_j \sum_k c_{-k} b_j^* a_j^* b_k a_k | - j\rangle_i \otimes |k\rangle_s \\
&= \sum_j b_j^* a_j^* | - j\rangle_i \otimes \sum_k c_{-k} b_k a_k |k\rangle_s. \tag{2.21}
\end{aligned}
$$

We can see that if we choose $b_k = 1/c_{-k}$, we obtain the state

$$|\psi\rangle_{\text{conj},i}^{\text{SB}} \otimes |\psi\rangle_s. \tag{2.22}$$

In practice, we must choose a dimension to work in. We select the number of OAM modes we will use, and we use the maximum OAM value m as our reference OAM; this OAM will have the lowest probability amplitude c_m. We then determine for each other ℓ-value what multiplier b_ℓ we require to reduce the amplitude of $|\ell\rangle$ to match that of $|m\rangle$. In other words, we seek b_ℓ such that $c_m = c_\ell b_\ell$.
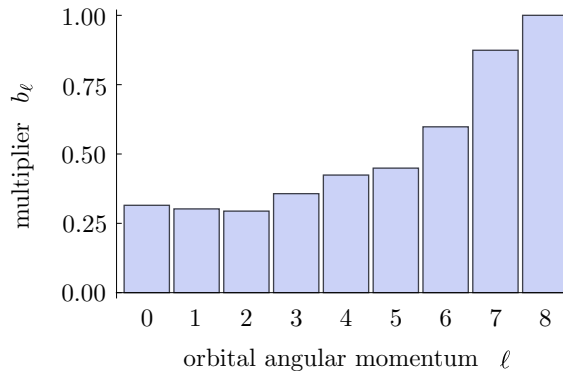
Figure 2.5: The multiplier b_ℓ required to flatten the spiral bandwidth.

Physically, this multiplier can be applied using the spatial light modulator. In order to determine these coefficients, we employ an iterative procedure. For the kth iteration, for a coefficient $b_{\ell,k}$, we calculate the deviation from $c_m - c_\ell b_{\ell,k} = 0$. The coefficient is given by $b_{\ell,k} = k/k_{\max}$, where $k_{\max}$ is the maximum number of iterations, such that we scan through the coefficents from 0 to 1. After performing $k_{\max}$ iterations, we fit a line to the data and choose the coefficient b_ℓ so that $c_m - c_\ell b_\ell = 0$. The exact procedure for each iteration is as follows.

1. Set the idler SLM to measure the state $|\phi\rangle = \frac{1}{\sqrt{1+b_{\ell,k}^2}} (|m\rangle_i + b_{\ell,k}|\ell\rangle_i)$.

2. Set the signal SLM to measure the state $|-m\rangle_s$.

3. Measure the counts $C_{m,k}$.

4. Set the signal SLM to instead measure the state $|-\ell\rangle_s$.

5. Measure the counts $C_{\ell,k}$.

6. Calculate $C_k = C_{\ell,k} - C_{m,k}$.

We perform this procedure for 20 values of $b_{\ell,k}$ in $[0, 1]$ at intervals of 0.05. We plot C_k as a function of $b_{\ell,k}$ and fit a line to the data. As C_k should be equal to zero, we find where the line intersects the $b_{\ell,k}$ axis and use the corresponding value of $b_{\ell,k}$ for our final value b_ℓ. We do this for all values of ℓ that will be used in the experiment.

An example of experimental results of the procedure for $m = 8$ is shown in Fig. 2.5. Here we show only the positive OAM modes under the assumption that the spiral bandwidth is symmetric and thus the negative OAM modes will give the same results. As our reference OAM is $m = 8$, the multiplier b_8 is simply equal to unity.

Chapter 3

Causal tomography

3.1 Notes and Acknowledgements

In this chapter, we describe an experiment in which tomography is performed on a system that can be a state, a process, or a combination of the two. We implement a quantum process on two entangled photons that provides the ability to select the exact causal structure existing between two qubits. We then determine the causal structure by performing causal tomography. We use the principles of quantum operations and state tomography as described in Chapter 1. We also make use of all techniques in Chapter 2 related to polarisation.

The work in this chapter was part of a collaboration with R. W. Spekkens and K. Ried. The collaboration, including some of the work described here and some further work, is to be submitted for publication:

M. Agnew,* K. Ried,* L. Vermeyden, D. Janzing, R. W. Spekkens, K. J. Resch, Inferring causal structure: a quantum advantage. *These authors contributed equally to this work.*

The text of this chapter constitutes an early version of the paper in which the content was mainly written by the author of this thesis. For the final version, further experiments were performed and theory developed that led to additional data analysis and further conclusions separate from the work described in this chapter. A draft of that manuscript is included as an appendix for completeness.

Contributions of the authors to this chapter are as follows.

DJ and RWS conceived the original idea for the project.

KR and RWS developed the project and the theory.

MA and KJR designed the experiment.

MA and LV performed the experiment.

MA performed all data analysis appearing in this chapter.

All text and figures in this chapter are written and provided by MA.

3.2   Overview

Determining how two objects are causally related is a problem that is common to many disciplines. Often one needs to perform tomography on a process occurring from one state to another, but correlations with the environment give rise to a causal structure that is not purely a process. In this work, using a new form of tomography termed *causal tomography*, we are able to deduce the causal structure between two qubits. Crucially, this type of tomography works regardless of whether the relation between the qubits is described by a common state, a process, or a combination thereof. We perform an experiment using quantum optics in which we implement a process with variable causal structure that allows us to select exactly how two qubits are related. We perform causal tomography on these qubits and completely recover the causal structure.

3.3   Introduction

In quantum optics, causal structure is important as it effects correlations between states. For example, one might have some process $\mathcal{E}_{A \to B}$ which transforms a qubit A into qubit B. In this case, the correlations that arise between the two qubits originate from a direct-cause structure (see Fig. 3.1(a)). For example, the rotation of horizontally polarised light into vertically polarised light has a direct-cause structure. Conversely, one might have a two-qubit state ρ_{AB}, containing qubits A and B. In this case, the correlations that arise between the two qubits originate from a common-cause structure (see Fig. 3.1(b)). For example, an entangled state produces strong correlations between qubits and exhibits a common-cause structure.

Now suppose a process transforms qubit A to qubit B, but there is a coupling between the environment and qubit A prior to the process, and a coupling between the environment and qubit B after the process. This common coupling with the environment causes additional correlations between the two qubits different from those induced by the direct process between them. As a result, the correlations between A and B originate simultaneously from a direct-cause structure and a common-cause structure; we refer to this as a hybrid-cause structure (see Fig. 3.1(c)).

Hybrid-cause structures arise often in experiments as it is difficult to completely separate the system of interest from its environment. Thus experimental results are often unknowingly affected by unintended correlations. For example, if one is trying to perform process tomography to determine process $\mathcal{E}$, but the environment is also producing correlations, then differences in the correlations will arise and the reconstructed process will not be process $\mathcal{E}$.

A solution to this problem is to perform a type of tomography that functions regardless of whether the system of interest is a process or a state. This type of tomography, which is termed *causal tomography*, completely determines the causal structure of the system. In this work, we implement a process on photonic qubits that provides the ability to select the exact causal structure of the qubits. We use causal tomography to reconstruct the complete causal structure with a high degree of accuracy.

3.4 Theory

Consider two qubits A and B in the state $\rho_{AB} = |\Phi^+\rangle\langle\Phi^+|$, and two additional qubits C and D that exist at a later time. We would like to be able to select one of three types of causal structure to occur between qubits A and C: direct-cause, common-cause, and hybrid-cause. A direct-cause structure can be implemented by allowing qubit A to become qubit C with no change; the identity operation is performed, and qubit B becomes qubit D to be used simply as a herald (see Fig. 3.1(d)). A common-cause structure can be implemented by swapping qubits A and B so that qubit B becomes qubit C. Now qubit A becomes qubit D and is used as a herald. Now qubits A and C have taken on the state originally held by A and B, so the common cause between A and B is now transferred to A and C (see Fig. 3.1(e)). Finally, a hybrid-cause structure can be implemented by creating a probabilistic mixture of these two scenarios: a probability p of swapping the qubits and creating a common-cause structure, and a probability $1 - p$ of perfoming the identity and creating a direct-cause structure (see Fig. 3.1(f)). This process can be expressed in the
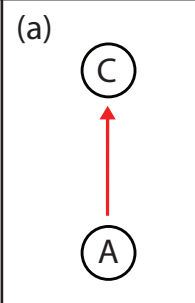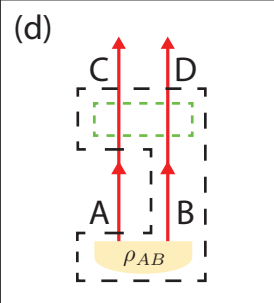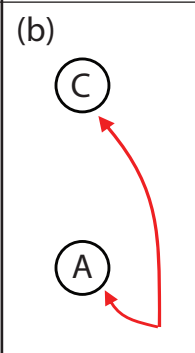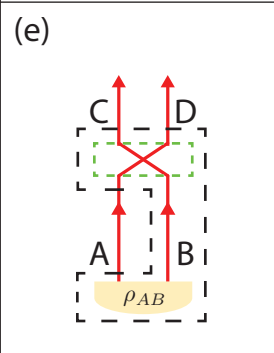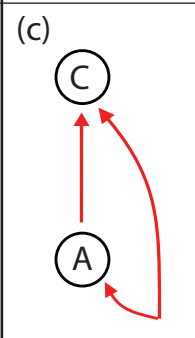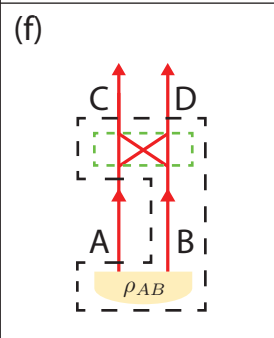
	Causal structure	Experimental implementation
Direct cause	(a)	(d)
Common cause	(b)	(e)
Hybrid cause	(c)	(f)

Figure 3.1: (a)-(c) Causal structures. In a direct-cause structure (a), A causes C. In a common-cause structure (b), A and C share a common cause. In a hybrid-cause structure (c), A and C are related by both direct- and common-cause structures. (d)-(f) Experimental implementations of the causal structures in (a)-(c). The green outlined box contains a process implementing the relevant causal structure. Direct-cause structure is implemented by the identity (d). Common-cause structure is implemented by the SWAP gate (e). Hybrid-cause structure is implemented by a probabilistic mixture of the identity and SWAP (f). The black dashed box contains all elements of the system that we do not have access to for measurement.

operator-sum representation as

$$\mathcal{E}_p(\rho_{AB}) = p\,\text{SWAP}\rho_{AB}\,\text{SWAP} + (1-p)\rho_{AB}, \tag{3.1}$$

where the SWAP operator swaps qubits A and B. The $p = 0$ case reduces simply to the direct-cause case, and the $p = 1$ case reduces to the common-cause case.

The causal structure is described by a matrix ρ_{AC} that is reconstructed from tomographic measurements as though A and C were a bipartite state. A projective measurement Π_i of qubit A is made just after preparation of the state ρ_{AB} and prior to implementation of the process. A second projective measurement Π_j is then performed on qubit C after the process is implemented. If A and C are in fact related by a common cause, then ρ_{AC} describes a bipartite state that is identical to the initially prepared state ρ_{AB}. Thus the expected state for the case of $p = 1$ is $\rho_{AC} = |\Phi^+\rangle\langle\Phi^+|$.

In the direct-cause case, the qubits A and C are related solely by a one-qubit process $\mathcal{E}_{A\to C}$. Due to the Choi-Jamiolkowsi isomorphism [40, 41] the reconstructed joint state ρ_{AC} corresponds to the Jamiolkowski operator [41], which is defined as

$$\rho_{AC} = (\mathcal{E}_{A\to C} \otimes \mathbb{1})(|\Phi^+\rangle\langle\Phi^+|)^{T_A}, \tag{3.2}$$

where X^{T_A} denotes the partial transpose of X with respect to qubit A. Thus the state we expect for the case of $p = 0$, i.e., when $\mathcal{E}_{A\to C} = \mathbb{1}$, is $\rho_{AC} = |\Phi^+\rangle\langle\Phi^+|^{T_A}$.

To understand the direct-cause case intuitively, first note that entangled states cannot exhibit correlations in all three bases; i.e., they must exhibit anti-correlations in at least one basis. For example, $|\Phi^+\rangle$ is anti-correlated in $|R\rangle/|L\rangle$, whilst $|\Psi^-\rangle$ is anti-correlated in $|H\rangle/|V\rangle$, $|D\rangle/|A\rangle$, and $|R\rangle/|L\rangle$. In contrast, two qubits related by direct cause will exhibit perfect correlations in all bases: if qubit A is in an arbitrary polarisation state $|P\rangle$, and qubit A becomes qubit C with no change, then qubit C will also be found in the state $|P\rangle$. As a result, if A and C are related by a direct cause, then the correlations obtained may be unphysical: they will not necessarily be explained by an entangled state, or in fact any physical two-particle state, and the resulting matrix can have negative eigenvalues. Since ρ_{AC} may be unphysical, we call it a *pseudo-density matrix* to distinguish it from positive semi-definite density matrices.

The pseudo-density matrix provides information about the type of causal structure describing the system. As a common-cause structure produces a pseudo-density matrix that describes a physical state, it must have non-negative eigenvalues. Conversely, a direct-cause structure produces an unphysical pseudo-density matrix that has at least one negative eigenvalue. As a result, finding the minimum eigenvalue of the pseudo-density matrix

36

$\lambda_{\min}(\rho_{AC})$ to be negative implies that the system cannot have a purely common-cause structure.

We can also obtain similar information from the partial transpose of the pseudo-density matrix. From the Choi-Jamiolkowski isomorphism [40, 41] and Eq. (3.2), if $\mathcal{E}_{A \to C}$ is a completely positive (CP) process, i.e., a direct-cause relation, then the partial transpose of the pseudo-density matrix $\rho_{AC}^{T_A}$ must be positive semi-definite as well. As an example, consider our case, where $\mathcal{E}_{A \to C} = \mathbb{1}$ is CP and $\rho_{AC}^{T_A} = [(|\Phi^+\rangle\langle\Phi^+|)^{T_A}]^{T_A} = |\Phi^+\rangle\langle\Phi^+|$, which of course is positive semi-definite. Conversely, $\rho_{AC}^{T_A}$ may have negative eigenvalues if the structure is common-cause. As a result, finding the minimum eigenvalue of the partial transpose of the pseudo-density matrix $\lambda_{\min}(\rho_{AC}^{T_A})$ to be negative implies that the system cannot have a purely direct-cause structure.

Combining the conditions for $\lambda_{\min}(\rho_{AC})$ and $\lambda_{\min}(\rho_{AC}^{T_A})$, we find that if both the pseudo-density matrix and its partial transpose have at least one negative eigenvalue, then the system can only be described by a hybrid-cause structure. In contrast, if all the eigenvalues of ρ_{AC} and its partial transpose are non-negative, we cannot make any conclusion about the state. These results are summarised in Table 3.1. Full details of the theory can be found in Appendix B.

		$\lambda_{\min}(\rho_{AC})$	
		Negative	Non-negative
$\lambda_{\min}(\rho_{AC}^{T_A})$	Negative	Hybrid-cause	Not purely direct-cause
	Non-negative	Not purely common-cause	Unknown

Table 3.1: Causal structures implied by minimum eigenvalues.

3.5 Experiment

We implement the probabilistic swap as described by Eq. (3.1) for varying values of p. We encode our qubits in the polarisation of single photons. Our experimental setup is shown in Fig. 3.2.

We produce polarisation-entangled photons using parametric downconversion in a non-linear crystal embedded in a Sagnac interferometer [28, 29, 36]. A 10-mW laser with centre wavelength 405 nm is propagated through a polarising beamsplitter (PBS), splitting into two components that travel in opposite directions in the Sagnac interferometer. Each component produces degenerate type-II phase-matched downconverted pairs at 809.5 nm
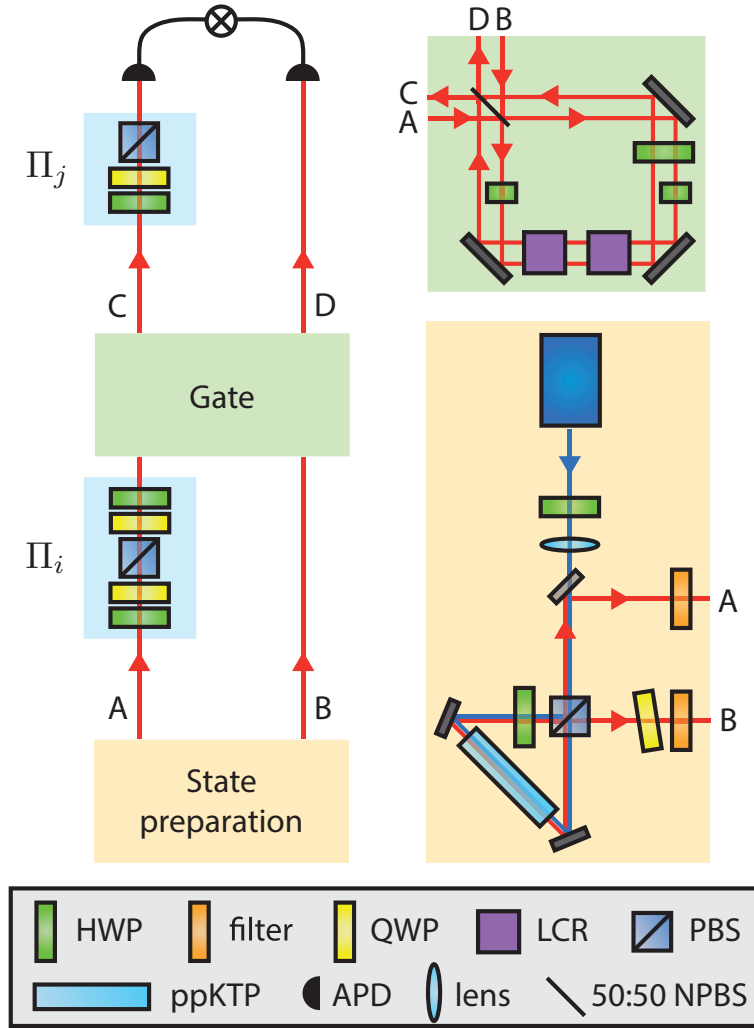
Figure 3.2: Experimental setup. In the state preparation stage, photon pairs entangled in the $|\Phi^+\rangle$ state are generated into modes A and B using a periodically-poled KTP (ppKTP) crystal. A projective measurement Π_i is performed on qubit A before the pair undergoes the process described by Eq. (3.1) to become modes C and D. Finally, a projective measurement Π_j is performed on qubit C, which is heralded by the arrival of qubit D. HWP = half-wave plate, QWP=quarter-wave plate, LCR=liquid crystal retarder, PBS=polarising beamsplitter, APD=avalanche photodiode, NPBS=non-polarising beamsplitter.

in a 10-mm periodically-poled KTP (ppKTP) crystal. There is a half-wave plate (HWP) placed on one side of the crystal so that each component enters the crystal with horizontal polarisation. Upon exiting the interferometer through the PBS, the photon pair is entangled in polarisation. The exact entangled state can be set using a HWP in the pump beam and a quarter-wave plate (QWP) in one of the exiting photon paths; we prepare the maximally entangled state $|\Phi^+\rangle$. In one arm, we separate the pump from the downconverted light using a dichroic mirror. The photons are coupled into single-mode fibres after passing through a bandpass filter to reduce background. We use standard quantum state tomography to characterise the source and find an average fidelity of 98.5% with $|\Phi^+\rangle$.

The experiment requires a process $\mathcal{E}_p$ that can faithfully transmit the photon polarisations directly from $A \to C$ and $B \to D$ with probability $1 - p$ and swap the photon polarisations from $B \to C$ and $A \to D$ with probability p. We implement this with the displaced Sagnac interferometer shown in Fig. 3.2. There are two distinct paths in the interferometer: one travelling clockwise, the other travelling anticlockwise. If there is no phase difference between the two paths, the light exits the interferometer at the same side of the beamsplitter at which it entered, with a transverse displacement; if there is a π phase difference, it exits at the opposite side. If light is incident on both input ports of the interferometer, the zero phase shift implements the identity, whilst the π phase shift implements the swap.

This probabilistic switching is implemented using a variable liquid crystal retarder (LCR), whose birefringence can be controlled by an external voltage. A second LCR is included and set to perform the identity for compensation. Three half-wave plates at 45° are inserted in the interferometer. The clockwise path encounters the LCR after passing through both waveplates, while the anticlockwise path encounters the LCR *between* the two waveplates. This asymmetry results in the birefringence affecting the two paths differently. When the LCR implements the identity $\mathbb{1}$, both paths pick up the same phase shift, so the net effect of the gate is the identity. When it implements the phase gate Z, one path picks up a π phase shift with respect to the other, so the net effect of the gate is the swap. We switch between these two levels of birefringence probabilistically using the random number generator in LabView at a rate of 5 Hz, effectively changing between the identity and swap operations with a chosen probability p.

The experiment proceeds as follows. After preparing the entangled state on modes A and B, we perform a projective measurement of the polarisation of mode A using a half-wave plate (HWP), quarter-wave plate (QWP), and polarising beamsplitter (PBS) followed by a second QWP and HWP. Qubits A and B are then sent into the interferometer implementing $\mathcal{E}_p$. The output of the process in mode C is projectively measured using a HWP, QWP, and PBS, and both C and D are detected. We detect in coincidence to ensure
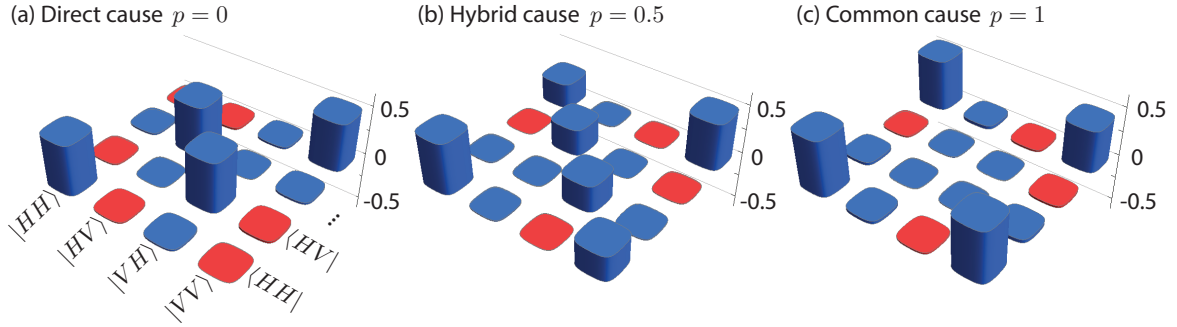
Figure 3.3: Real parts of the reconstructed pseudo-density matrices ρ_{AC}. (a) The direct-cause structure with $p = 0$ is an unphysical pseudo-density matrix. (b) The hybrid-cause structure with $p = 0.5$ is a probabilistic mixture of the direct-cause and common-cause pseudo-density matrices. (c) The common-cause structure with $p = 1$ is a physical density matrix describing the entangled state $|\Phi^+\rangle$. Positive values are shown in blue whilst negative are shown in red. Here we use $|ac\rangle$ to represent the basis state $|a\rangle_A \otimes |c\rangle_C$. Imaginary parts of the matrices are not shown as the average of the absolute value of their components was 0.02 ± 0.02.

that the source produced the requisite state. The coincidence detection is done using single-photon detectors and coincidence logic with a window of 3 ns. Our coincidence count rate at C and D is approximately 2000 Hz. We can set each half- and quarter-wave plate pair to measure any of the six Pauli eigenstates. Our measurement set consists of horizontal $|H\rangle$ and vertical $|V\rangle$ polarisations as well as $|D\rangle$, $|A\rangle$, $|R\rangle$, and $|L\rangle$. For each choice of measurement at A, we cycle through all six measurement possibilities at C for a total of 36 measurements.

3.6   Reconstruction

Given the coincidence counts n_{ij} obtained at C and D by performing measurement i on qubit A and measurement j on qubit C, we are able to perform tomographic reconstruction to obtain the causal structure relating A and C. We use maximum-likelihood estimation [5] to reconstruct the pseudo-density matrix ρ_{AC}; however, we remove the restriction of a positive semi-definite matrix. Instead, we parametrise the matrix in the following way:

$$\rho_{AC} = \begin{pmatrix} t_1 & t_5 + it_6 & t_{11} + it_{12} & t_{15} + it_{16} \\ t_5 - it_6 & t_2 & t_7 + it_8 & t_{13} + it_{14} \\ t_{11} - it_{12} & t_7 - it_8 & t_3 & t_9 + it_{10} \\ t_{15} - it_{16} & t_{13} - it_{14} & t_9 - it_{10} & t_4 \end{pmatrix}, \tag{3.3}$$

where all t_i are real, thus forcing our pseudo-density matrix to be Hermitian while allowing for negative eigenvalues. We then find ρ_{AC} that minimises the quantity

$$\chi^2 = \sum_{ij} \frac{\{\text{Tr}[\rho_{AC}(\Pi_i^A \otimes \Pi_j^C)] - n_{ij}\}^2}{\text{Tr}[\rho_{AC}(\Pi_i^A \otimes \Pi_j^C)]}, \tag{3.4}$$

where $\Pi_i^A = |i\rangle\langle i|$ is the projector of state $|i\rangle$ measured at qubit A, $\Pi_j^C = |j\rangle\langle j|$ is the projector of state $|j\rangle$ measured at qubit C, and n_{ij} is the corresponding number of coincidence counts measured. Finally, the matrix is normalised to unit trace.

3.7 Results

We implemented the process described by Eq. (3.1) for varying values of p and performed tomography on qubits A and C to determine the pseudo-density matix ρ_{AC}. The reconstructed pseudo-density matrices for three values of p are shown in Fig. 3.3.

The pseudo-density matrix describing a common-cause structure, implemented using $p = 1$, is shown in Fig. 3.3(c). In this case, as the qubits are swapped during process (3.1), qubit B becomes qubit C, and thus qubit C is entangled with qubit A in the entangled state $|\Phi^+\rangle$. The reconstructed pseudo-density matrix is very close to this entangled state; in fact, the trace distance between our reconstructed pseudo-density matrix and $|\Phi^+\rangle$ is 0.116, indicating that the states are very similar.

The pseudo-density matrix describing a direct-cause structure, implemented using $p = 0$, is shown in Fig. 3.3(a). In this case, as the qubits are left unchanged when passing through process (3.1), qubit A becomes qubit C and thus we will see perfect correlations between A and C. As a result, we expect to see an unphysical pseudo-density matrix that corresponds to the partial transpose of the entangled state, $|\Phi^+\rangle\langle\Phi^+|^{T_A}$. The reconstructed pseudo-density matrix is very close to this state; in fact, the trace distance between the two is 0.098, indicating that the states are very similar.

The pseudo-density matrix describing a hybrid-cause structure, implemented using $p = 0.5$, is shown in Fig. 3.3(b). In this case, as the qubits undergo a probabilistic mixture of a direct-cause structure and a common-cause structure, we expect to see a probabilistic mixture of the two states above: $(|\Phi^+\rangle\langle\Phi^+| + |\Phi^+\rangle\langle\Phi^+|^{T_A})/2$. The reconstructed pseudo-density matrix is very close to this state; the trace distance between the two is 0.084, indicating a high degree of similarity between the states.

The minimum eigenvalues of the pseudo-density matrix and of its partial transpose are plotted as a function of p in Fig. 3.4. The error bars are the same for all values and

41
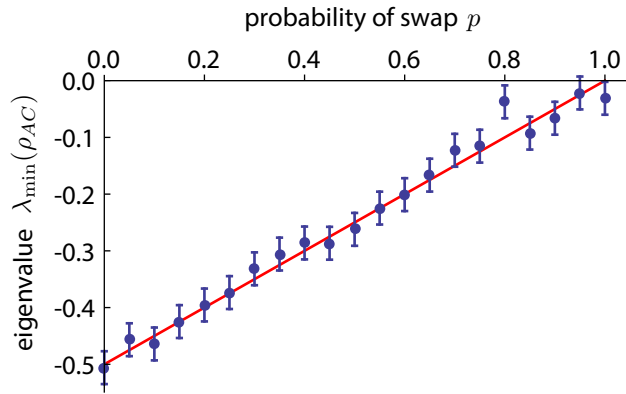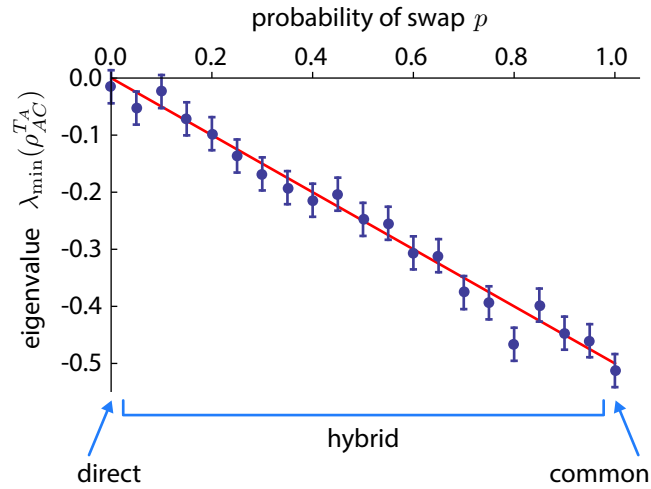
Figure 3.4: Minimum eigenvalues of (a) the pseudo-density matrix and (b) the partial transpose of the pseudo-density matrix as a function of SWAP probability p. Blue points represent measured data; red lines represent theoretical predictions.

were calculated by repeating the measurements 100 times for $p = 0.5$, performing causal tomography each time, and calculating the standard deviation of the resultant minimum eigenvalue. The experimental data shows good agreement with theoretically predicted values.

Furthermore, from the eigenvalues of the pseudo-density matrix and those of its partial transpose, we are able to make inferences about the causal structure of the system. For example, when $p = 0$, the minimum eigenvalue of the pseudo-density matrix was found to be $\lambda_{\min}(\rho_{AC}) = -0.506 \pm 0.028 < 0$, whilst that of the partial transpose was found to be $\lambda_{\min}(\rho_{AC}^{T_A}) = -0.015 \pm 0.025$. This latter value is within one standard deviation of zero. These values are compatible with an almost exclusively direct-cause structure. Similarly, at $p = 1$ we found $\lambda_{\min}(\rho_{AC}^{T_A}) = -0.513 \pm 0.028 < 0$ and $\lambda_{\min}(\rho_{AC}) = -0.031 \pm 0.028$. This latter value is very close to zero; the slight difference is likely due to unavoidable errors in the detection process. These values are compatible with a structure that is almost exclusively common-cause. Given the promise that the causal structure is either direct-cause or common-cause, this allows us to determine the causal structure unambiguously. Finally, at intermediate values of p, including $p = 0.5$, both values are clearly negative. This data cannot be interpreted as either direct-cause or common-cause and instead indicates a hybrid causal structure.

3.8   Conclusion

We have performed causal tomography on systems with varying causal structure: direct-cause, common-cause, and hybrid-cause. We implemented the varying causal structure using a quantum optical interferometer that applied a probabilistic mixture of the identity and swap operations on a pair of entangled photonic qubits. We reconstructed pseudo-density matrices that describe the causal structure and obtained trace distances with the expected matrices that indicated high similarity. We examined the eigenvalues of the pseudo-density matrix and its partial transpose in order to determine possible causal structures to describe the data. This indicates that causal tomography can be implemented to determine the causal structure of a system with a high degree of accuracy.

Chapter 4

Discriminating single-photon states unambiguously in high dimensions

4.1 Notes and Acknowledgements

In this chapter, we describe an experiment in which single photons were encoded with high-dimensional states in their orbital angular momentum. These states were then discriminated unambiguously with a high degree of confidence. We use the principles of POVMs and state discrimination as discussed in Chapter 1. We also make use of all techniques in Chapter 2 related to orbital angular momentum.

This chapter has been submitted for publication:

M. Agnew, E. Bolduc, K. J. Resch, S. Franke-Arnold, J. Leach, Discriminating single-photon states unambiguously in high dimensions. Accepted for publication in Physical Review Letters, to be published May 30th.

JL and SF conceived the experiment.

MA performed the experiment and data analysis.

EB and JL contributed to the design and realisation of the experiment.

MA wrote the manuscript. All authors contributed to editing for the final version.

4.2   Overview

The ability to uniquely identify a quantum state is integral to quantum science, but for non-orthogonal states, quantum mechanics precludes deterministic, error-free discrimination. However, using the non-deterministic protocol of unambiguous state discrimination (USD) enables error-free differentiation of states, at the cost of a lower frequency of success. We discriminate experimentally between non-orthogonal, high-dimensional states encoded in single photons; our results range from dimension $d = 2$ to $d = 14$. We quantify the performance of our method by comparing the total measured error rate to the theoretical rate predicted by minimum-error state discrimination. For the chosen states, we find a lower error rate by more than one standard deviation for dimensions up to $d = 12$. This method will find immediate application in high-dimensional implementations of quantum information protocols, such as quantum cryptography.

4.3   Introduction

Discriminating between different quantum states without error is a fundamental requirement of quantum information science. However, due to the nature of quantum mechanics, only orthogonal states can be exactly discriminated without error 100% of the time. In contrast, the discrimination of non-orthogonal states requires a decrease in either detection accuracy, using minimum-error state discrimination, or detection frequency, using unambiguous state discrimination. Minimum-error state discrimination (MESD) always provides information about the state, though the information may be incorrect [22]. Conversely, unambiguous state discrimination (USD) provides either the correct information about a detected state or inconclusive information about the state [8, 9, 10, 11, 12, 13, 14, 15, 16, 17, 18, 19, 20, 21].

High-dimensional quantum states are an important resource for quantum information. In comparison to qubits, the use of qu*d*its, which are states belonging to a d-dimensional space, provides access to a larger alphabet and correspondingly higher information rates, and a higher tolerance to noise. The ability to unambiguously discriminate such states is thus of key importance, and successful protocols that accomplish this task will extend the use of these states in quantum information science. Examples of such systems include the time degree of freedom and the spatial light profile, or more specifically the orbital angular momentum degree of freedom, which we use in this work [33, 42, 43, 44, 45, 46, 47, 48, 49, 50, 51, 52, 53, 54]. High-dimensional USD is also potentially relevant for pattern

recognition in quantum and classical regimes as images contain typically very large numbers of spatial modes and are non-orthogonal to one another [55].

The problem of unambiguous discrimination of qu*d*it states has received a great deal of attention [56, 57, 58, 59, 60, 61]. USD was first experimentally realised, with a classical light source, to distinguish two non-orthogonal states in the polarisation degree of freedom [23]. A subsequent experiment with a similar source extended this to distinguish three states encoded in three-dimensional photon path information [62]. USD has also been performed for two mixed polarisation states using a quantum dot single-photon source [63].

In this work, we discriminate unambiguously between non-orthogonal quantum states encoded in single photons, in dimensions ranging from $d = 2$ to $d = 14$. While USD theoretically promises the unambiguous discrimination of any set of states, real experimental situations always include error sources, and perfect discrimination in an experimental environment is challenging. Even with these unavoidable errors, we show that our scheme successfully discriminates between the chosen states and does so with lower error rates than those predicted by MESD. We note that here we implement USD as a sequential measurement of all required detection states. Using instead simultaneous detection, e.g., based on OAM sorter technology [25, 26], would allow unambiguous discrimination at the single-photon level.

4.4 Theory

To perfectly distinguish orthogonal states, one requires projections onto the orthogonal state basis, giving d measurement outcomes in a d-dimensional space. To implement the USD protocol, which distinguishes non-orthogonal states, one requires the introduction of an additional measurement outcome – an inconclusive result – into the procedure, providing $d + 1$ measurement possibilities. The increased number of measurement outcomes necessitates the introduction of an ancillary dimension or degree of freedom; orbital angular momentum lends itself well to this treatment as it provides an unlimited supply of additional dimensions. The introduction of the inconclusive result enables the remaining measurement outcomes to be orthogonalised [64]. The protocol then provides one of the following: a correct state identification, in which case the state is known with certainty, or an inconclusive result, in which case no information is known about the state.

In this work, we choose d states in d dimensions that have an equal overlap with each other; these are referred to as equally probable, linearly independent, symmetrical states
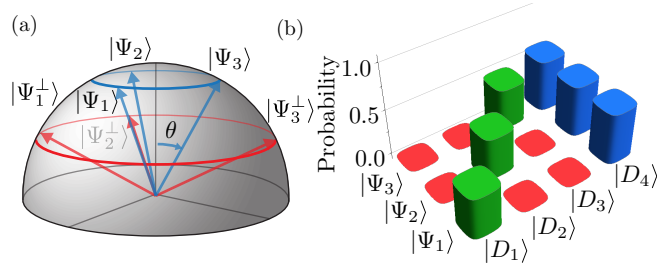
46

Figure 4.1: **Vectors and probabilities in three dimensions.** (a) As the states we consider have real amplitudes, they can be represented on a sphere whose axes are the amplitudes of each basis vector. The vectors we choose to discriminate in dimension $d = 3$, $\{|\Psi_i\rangle\}$ with $\theta \approx 33°$, are shown in blue. Vectors perpendicular to each pair ($\{|\Psi_i^{\perp}\rangle\}$) are shown in red. (b) Theoretically calculated probabilities of discrimination for the vectors shown in (a).

and, compared to less symmetric states, have a maximal discrimination probability [11] (see Supplementary Materials). See Fig. 4.1(a) for an example in three dimensions. Note that all of these states have only real amplitudes. The overlap between any two states is then a function of the parameter θ, given by

$$\langle\Psi_i|\Psi_j\rangle = \frac{d\cos^2\theta - 1}{d - 1}, \tag{4.1}$$

for $i \neq j$. To ensure positive overlap between the input states, the maximum value of θ is $\theta_{\max} = \cos^{-1}\sqrt{1/d}$ (see Supplementary Materials).

In the problem of USD, we must establish a set of measurement states $\{|D_i\rangle\}$ to distinguish the set of input states $\{|\Psi_i\rangle\}$. To achieve this, for every state $|\Psi_i\rangle$ we first identify a preliminary measurement state $|\Psi_i^{\perp}\rangle$; this preliminary state is orthogonal to all other states $|\Psi_j\rangle$ (for $j \neq i$) but has a nonzero overlap with $|\Psi_i\rangle$. Due to this definition, a detection with $|\Psi_i^{\perp}\rangle\langle\Psi_i^{\perp}|$ will unambiguously indicate that the photon was in state $|\Psi_i\rangle$. These d preliminary measurement states $\{|\Psi_i^{\perp}\rangle\}$, however, do not generally form an orthonormal basis set. This can be achieved by extending the preliminary measurement states to an ancillary dimension, followed by normalisation to obtain d measurement states $\{|D_i\rangle\}$. The basis set is completed by including an additional state $|D_{d+1}\rangle$ orthogonal to all other measurement states, so that the whole $(d+1)$-dimensional basis of measurement states is $\{|D_i\rangle\}$ with $\langle D_i|D_j\rangle = \delta_{ij}$.

The probability of obtaining an inconclusive result, $|\langle\Psi_i|D_{d+1}\rangle|^2$, and the probability of correctly identifying a state, $|\langle\Psi_i|D_i\rangle|^2$, sum to unity as the probability of an error is by definition zero. The probability of an inconclusive result is precisely the overlap

47

Sample holograms for state preparation

$|\Psi_1\rangle$ $|\Psi_2\rangle$ $|\Psi_3\rangle$

Sample holograms for measurement

$|D_1\rangle$ $|D_2\rangle$ $|D_3\rangle$ $|D_4\rangle$
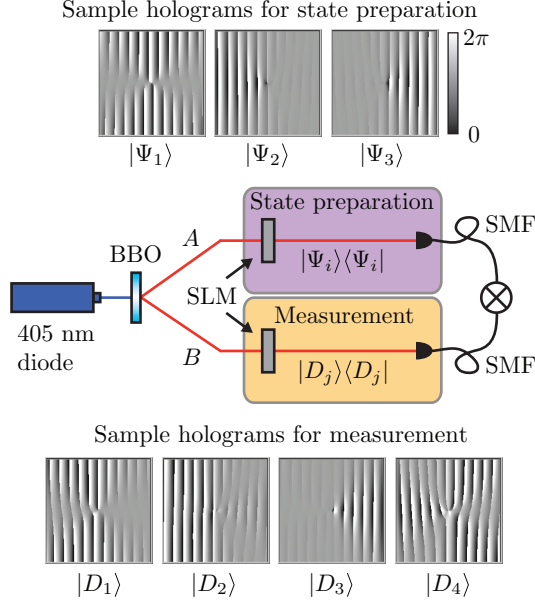
Figure 4.2: **Experimental setup.** A pair of entangled photons is produced in a BBO crystal. Arm A is used to prepare a state $|\Psi_i\rangle$, indicated by the purple box; arm B is used to perform a measurement $|D_j\rangle$, indicated by the orange box. Each measurement is accomplished using a spatial light modulator (SLM) and single-mode fibre (SMF). The holograms shown are representative of those used for state preparation and measurement in dimension $d = 3$.

between any two input states [9, 11]. Thus using Eq. (4.1), we can write the probabilities of successful identification, erroneous identification, and inconclusive result as

$$p_{\mathrm{suc}} = \frac{d}{d-1}\sin^2\theta \tag{4.2a}$$

$$p_{\mathrm{err}} = 0 \tag{4.2b}$$

$$p_{\mathrm{inc}} = \frac{d\cos^2\theta - 1}{d-1}. \tag{4.2c}$$

Theoretical predictions of these values for states in three dimensions are shown in Fig. 4.1(b).

4.5   Experiment

We use the process outlined above to find the discrimination states for a range of input states in a range of dimensions, and we use them to implement USD as a sequential measurement on orbital angular momentum states. Our experimental procedure is as follows.

We produce entangled photons by spontaneous parametric downconversion (SPDC) [27] in a 3-mm type-I BBO crystal with a phase mismatch factor of approximately $\phi = -1$. We pump the crystal with a 100-mW laser at 405 nm. In each path, we image the plane of the BBO crystal to a different section of a spatial light modulator (SLM), allowing us to manipulate both the phase and the amplitude of each photon's mode with high fidelity. The simplified experimental setup is shown in Fig. B.2.

The photons produced from the BBO crystal are entangled in their orbital angular momentum in the two-photon state $|\psi\rangle = \sum_{\ell=-\infty}^{\infty} c_\ell |\ell\rangle_A \otimes |-\ell\rangle_B$, where $|c_\ell|^2$ is the probability of finding photon A with OAM $\ell\hbar$ and photon B with OAM $-\ell\hbar$ [34]. The SLM in our experiment performs a number of functions in regards to this state: first, it allows us to select a range of OAM values and explore a discrete dimension space, and second, it allows us to equalise the probabilities of detection, a process similar to entanglement concentration [39]. Finally, in a procedure similar to that in Refs. [46, 47, 48, 51, 52, 53], the SLM, in combination with the single-mode fibres, allows us to perform high-fidelity projective measurements on the signal and idler photons. By displaying a hologram of the conjugate phase of a particular mode, we convert the chosen state into the Gaussian mode, which can then be coupled into a single-mode fibre.

The entanglement of the OAM degree of freedom allows the use of remote state preparation [37, 38], which enables us to herald the presence of a range of single-photon states $|\Psi_i\rangle$. These heralded states are prepared by using one half of the SLM in combination with a single-mode fibre. Consequently, the detection of a single photon in the first arm collapses the photon in the other arm into the desired state. The second path is then used to perform the state discrimination measurements $|D_j\rangle$ on the heralded state $|\Psi_i\rangle$, and we measure the coincidences between the two paths. In our experiment, as we use a single SLM, the measurements on the signal and idler modes are performed simultaneously. In this manner, the input states are prepared at the same time as they are measured. However, identical results would be obtained using two spatially separated SLMs, where the preparation and measurement stages are performed one after another. Our chosen method of measurement does not limit the use of such states for tasks in quantum information processing.

For a given dimension d, we measure all $d + 1$ measurement outcomes for each input state $|\Psi_i\rangle$. We use our measurements to calculate a quantity called the quantum contrast, which is defined by the coincidence rates normalised by the singles $Q_{ij} = C_{ij}/(S_{Ai}S_{Bj}t)$; this accounts for any variations in the quantum efficiency of the detection and generation of particular states. Here C_{ij} is the number of coincidence counts defined by an event in both detectors within a time window of $t = 25$ ns. The quantities S_{Ai} and S_{Bj} represent the number of counts in path A (heralding the preparation of $|\Psi_i\rangle$) and B (measuring

49

$|D_j\rangle$) respectively. We normalise this quantum contrast into probabilities using $P_{ij} = (Q_{ij} - 1)/\sum_j(Q_{ij} - 1)$. The -1 term accounts for the fact that two independent and uncorrelated sources will have a quantum contrast equal to unity. An integration time of 30 s was used for each measurement, and the maximal coincidence count rate was approximately 350 Hz.
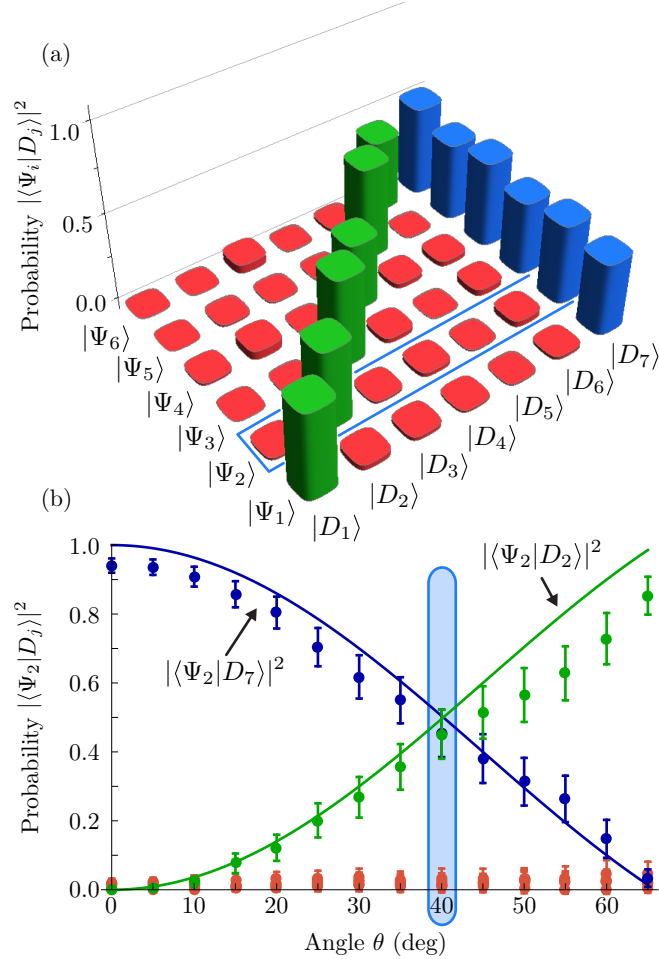
Figure 4.3: **Experimental results for dimension $d = 6$.** (a) Probabilities of detecting input states $|\Psi_i\rangle$ using detection states $|D_j\rangle$ when $\theta = 40°$. (b) Probabilities as a function of θ of identifying the state $|\Psi_2\rangle$ correctly (green, $|D_2\rangle$), incorrectly (red, $|D_1\rangle, |D_3\rangle, |D_4\rangle, |D_5\rangle, |D_6\rangle$), or inconclusively (blue, $|D_7\rangle$). The points represent experimental data, while the solid lines represent theoretical values calculated using Eq. (4.2). The points within the shaded area in part (b) correspond to the blue outlined box in part (a). The uncertainties were calculated using Gaussian error propagation, where the measured counts N were assumed to have standard deviation $\sqrt{N}$.

50

4.6 Results

We have implemented our procedure for unambiguous discrimination of states in high dimensions ranging from $d = 2$ to $d = 14$ and with varying overlap between the states. In Fig. 4.3, we show the unambiguous discrimination of 6 states in $d = 6$ dimensions.

Fig. 4.3(a) shows the results at $\theta = 40°$ of measuring all $\{|\Psi_i\rangle\}$ states using all $\{|D_j\rangle\}$ measurements. The green bars denote successful identifications, the red bars denote erroneous identifications, and the blue bars denote inconclusive results. As the probabilities of successful identification greatly exceed the probabilities of erroneous identification, it follows that each input state $|\Psi_i\rangle$ almost always results in either correct detection by $|D_i\rangle$ or the inconclusive outcome $|D_7\rangle$.

Fig. 4.3(b) shows the results of measuring a specific state, in this case $|\Psi_2\rangle$, using all $\{|D_j\rangle\}$ measurements, for a range of angles θ. Each angle corresponds to a different overlap between the $\{|\Psi_i\rangle\}$ states as in Eq. (4.1). An angle of $0°$ corresponds to a complete overlap between the states and hence a completely inconclusive result; the probability for correct identification increases with θ, with in principle perfect identification at $\theta \approx 66°$. The solid lines indicate theoretical predictions from Eq. (4.2); our experimental data is in good agreement with these predictions.

Whilst USD has the theoretical advantage of never misidentifying a state, in practice this is not possible to achieve. In experimental implementations, errors necessarily occur due to finite detector efficiency and errors caused by transformation optics. To evaluate the performance of our measurements, we compare our experimentally recorded errors to those theoretically predicted for the MESD protocol. A significant advantage is found in the case that the recorded errors for our scheme are smaller than those produced in MESD.

Due to the equal overlap between our input states, the minimum error rate for MESD in d dimensions [65] reduces to (see Supplementary Materials)

$$p_{\text{err}} \geq \frac{1}{2} \left(1 - \sqrt{1 - |\langle \Psi_i | \Psi_j \rangle|^2} \right), \tag{4.3}$$

where the overlap $\langle \Psi_i | \Psi_j \rangle$ is given by Eq. (4.1). A violation of this inequality indicates that USD provides less ambiguity in state identification than is theoretically possible using MESD.

In Fig. 4.4, we compare this bound to the mean total error rate observed using our method. To determine our error rate, we first determine the error rate for a single input
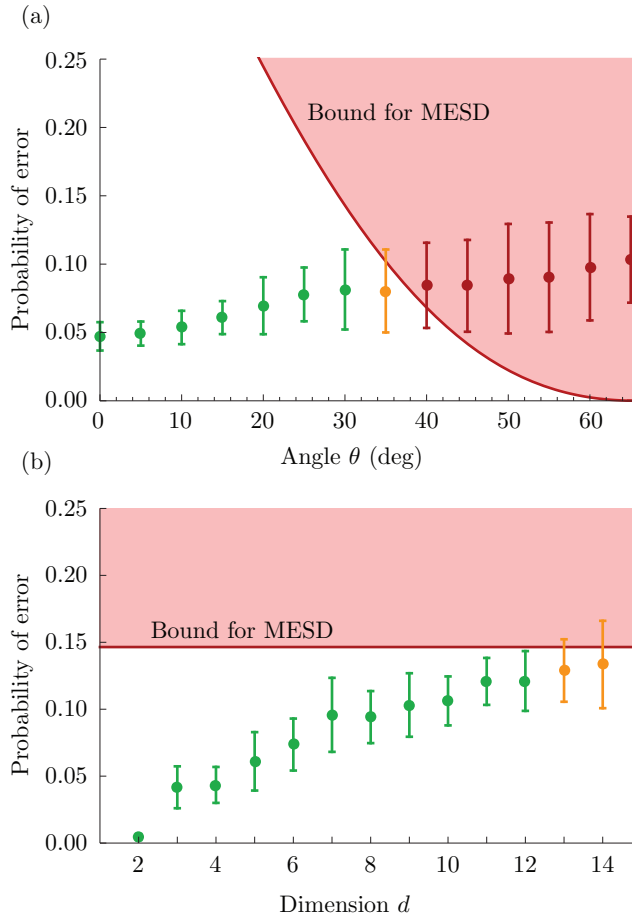
Figure 4.4: **Probability of error.** (a) Mean total error rate as a function of angle in dimension $d = 6$. (b) Mean total error rate as a function of dimension. Here the angle θ is chosen individually for each dimension such that the MESD bound is the same in all dimensions. In both plots, the red line indicates the theoretical minimum error rate predicted for MESD. The green points denote error rates at least one standard deviation below this limit, the orange points denote error rates whose uncertainties extend above the limit, and the red points denote error rates above the limit. The uncertainties are the standard deviations associated with the mean values.

state $|\Psi_i\rangle$; this is the sum of all possible incorrect state identifications. We then average over all input states $\{|\Psi_i\rangle\}$ to obtain the mean total error rate.

Fig. 4.4(a) shows the total error rate as a function of angle for the $d = 6$ case. The total error rate for angles up to $\theta = 30°$ is at least one standard deviation below the MESD bound, demonstrating that our approach is particularly successful for states with large overlap. The total error rate exceeds the MESD bound at higher angles, where the states have lower overlap and are closer to orthogonal. In this case, the bound converges to 0, matching the theoretical prediction for USD. Since the two schemes converge, it is inevitable that the experimentally measured errors exceed the ideal MESD curve at a sufficiently high angle.

Fig. 4.4(b) shows the total error rate as a function of dimension for a fixed overlap of $1/\sqrt{2}$ between the initial states. We choose a constant overlap so that the MESD bound is equal in all dimensions (in this case, $(1 - \sqrt{1/2})/2 \approx 0.146$). To achieve the constant overlap, the parameter θ must change with dimension (see Supplementary Materials). The total error rate for dimensions up to $d = 12$ is below the MESD bound by at least one standard deviation.

In dimensions $d \geq 13$, the bound for MESD is successfully violated, but by less than one standard deviation. This is due to two main factors. Firstly, for all of these data, the average measured probability of obtaining an error, i.e., measuring a state $|\Psi_i\rangle$ with an incorrect detection state $|D_j\rangle$ ($i \notin \{j, d+1\}$), is approximately 1%. As the dimension increases, so too does the number of opportunities to misidentify a state. Thus the total error grows accordingly, making it increasingly difficult to obtain a low total error. Secondly, due to the limited spiral bandwidth in the downconverted state, the probability amplitudes of the individual OAM modes decrease as ℓ increases. This limits the coincidence rate, and thus increases the uncertainty of the measurements, for high dimensions.

4.7 Conclusions

We have demonstrated USD via sequential measurements to distinguish d non-orthogonal single-photon states in d-dimensional Hilbert spaces. In a modified set-up, our method could be realised as a true POVM experiment in high dimensions. To implement simultaneous measurement of the input states, one would require a scheme that takes any of the d non-orthogonal states and produces $d + 1$ orthogonal outputs. Such a scheme is similar in concept to current mode sorting technology that can, in principle, take d orthogonal OAM input states and sort them into d orthogonal transverse states [25, 26]. Before using

an OAM mode sorter, we would require an initial stage to convert the input states into a $(d+1)$-dimensional basis. Such an experimental implementation will be the focus of future work.

In our experiment, while experimental constraints prevent completely error-free identification, we have shown that, for a range of high-dimensional states, our method still provides a lower error rate than minimum-error state discrimination. With suitable improvements in SLM resolution, spiral bandwidth production, and detector efficiency, this could be increased to even higher dimensions. This method of state discrimination will allow the use of high-dimensional non-orthogonal states in quantum protocols, enabling secure quantum communication with larger alphabets.

4.8 Acknowledgements

4.9 Supplementary Materials

4.9.1 Determining d symmetric states in d dimensions

The d states in d dimensions that we choose to distinguish are maximally separated when projected onto $d-1$ dimensions. We describe first how to construct the $d-1$ projected vectors $\{|\Psi_i'\rangle\}$. Without loss of generality, the first of these vectors, $|\Psi_1'\rangle$, can be chosen to lie along one axis such that its first component is 1 and its remaining components are 0. We can construct all other vectors from their pairwise overlap, $\langle\Psi_i'|\Psi_j'\rangle = -1/(d-1)$ for $i \neq j$, and the normalisation condition, $\langle\Psi_i'|\Psi_i'\rangle = 1$. The overlap condition requires that the first component of each remaining vector $|\Psi_{j\geq2}'\rangle$ must be $-1/(d-1)$. For the second vector we can determine the second component from the normalisation condition and set all following components equal to zero. The remaining vectors can be iteratively determined in the same way: for the third vector, the second component is determined from the overlap with the second vector, the third from normalisation, and all following components are zero; and similar for all subsequent vectors.

Once we have obtained these states, we transform them into d-dimensional states using

$$|\Psi_i\rangle = \sin\theta\,|\Psi'_i\rangle + \cos\theta\,|d\rangle. \tag{4.4}$$

For example, in dimension $d = 3$, the states are the lifted trine states

$$|\Psi_1\rangle = \sin\theta\,|\ell_1\rangle + \cos\theta\,|\ell_3\rangle \tag{4.5a}$$

$$|\Psi_2\rangle = -\frac{1}{2}\sin\theta\,|\ell_1\rangle + \frac{\sqrt{3}}{2}\sin\theta\,|\ell_2\rangle + \cos\theta\,|\ell_3\rangle \tag{4.5b}$$

$$|\Psi_3\rangle = -\frac{1}{2}\sin\theta\,|\ell_1\rangle - \frac{\sqrt{3}}{2}\sin\theta\,|\ell_2\rangle + \cos\theta\,|\ell_3\rangle, \tag{4.5c}$$

where $|\ell_1\rangle$, $|\ell_2\rangle$, and $|\ell_3\rangle$ are the three chosen OAM basis states.

4.9.2 Determining discrimination states

We determine the orthogonal states $\{|\Psi_i^\perp\rangle\}$, with $\langle\Psi_i^\perp|\Psi_j\rangle \propto \delta_{ij}$, by taking each $(d-1)$-sized subset of the $\{|\Psi_i\rangle\}$ vectors and applying the Gram-Schmidt algorithm to find a vector orthogonal to this subset.

We then transform the set $\{|\Psi_i^\perp\rangle\}$ to an orthonormal basis set $\{|D_i\rangle\}$ by extension to an ancillary dimension followed by normalisation. For this, we make use of the fact that due to the inherent symmetry, the inner product of any two of the $\{|\Psi_i^\perp\rangle\}$ states, $\langle\Psi_i^\perp|\Psi_j^\perp\rangle$, $i \neq j$, is the same. As a result, we obtain

$$|D_i\rangle = |\Psi_i^\perp\rangle + \sqrt{-\langle\Psi_1^\perp|\Psi_2^\perp\rangle}\,|d+1\rangle. \tag{4.6}$$

Finally, we identify the inconclusive measurement state $|D_{d+1}\rangle$ such that $\langle D_i|D_{d+1}\rangle = 0$, resulting in a complete basis in $d+1$ dimensions, again using the Gram-Schmidt algorithm.

4.9.3 Transforming $|\Psi_i^\perp\rangle$ to $|D_i\rangle$

Here we illustrate the calculation for $d = 3$, but it functions similarly in higher dimensions. In order to orthogonalise our three 3-dimensional measurement states

$$|\Psi_1^\perp\rangle = \sqrt{3}\cos\theta\sin\theta\,|\ell_1\rangle + \frac{\sqrt{3}}{2}\sin^2\theta\,|\ell_3\rangle \tag{4.7a}$$

$$|\Psi_2^\perp\rangle = -\frac{\sqrt{3}}{2}\cos\theta\sin\theta\,|\ell_1\rangle + \frac{3}{2}\cos\theta\sin\theta\,|\ell_2\rangle + \frac{\sqrt{3}}{2}\sin^2\theta\,|\ell_3\rangle \tag{4.7b}$$

$$|\Psi_3^\perp\rangle = -\frac{\sqrt{3}}{2}\cos\theta\sin\theta\,|\ell_1\rangle - \frac{3}{2}\cos\theta\sin\theta\,|\ell_2\rangle + \frac{\sqrt{3}}{2}\sin^2\theta\,|\ell_3\rangle \tag{4.7c}$$

into three 4-dimensional measurement states $\{|D_1\rangle, |D_2\rangle, |D_3\rangle\}$, we need only to add an arbitrary fourth component to each vector such that

$$|D_j\rangle = |\Psi_j^\perp\rangle + (a_j + ib_j)|d+1\rangle, \tag{4.8}$$

where a_i and b_i are real numbers. For orthogonality, these states must satisfy

$$\langle D_i|D_j\rangle = C\delta_{ij}, \tag{4.9}$$

where C is some constant since the vectors are as yet unnormalised.

By examining the inner product $\langle D_1|D_2\rangle$, we obtain

$$\langle D_1|D_2\rangle = 0 = \langle\Psi_1^\perp|\Psi_2^\perp\rangle + a_1 a_2 + i a_1 b_2 - i b_1 a_2 + b_1 b_2. \tag{4.10}$$

The real and imaginary parts then independently need to be equal to zero:

$$\langle\Psi_1^\perp|\Psi_2^\perp\rangle + a_1 a_2 + b_1 b_2 = 0 \tag{4.11}$$

$$a_1 b_2 - b_1 a_2 = 0. \tag{4.12}$$

From the inner products $\langle D_2|D_3\rangle$ and $\langle D_1|D_3\rangle$, we obtain similar equations. These six equations are solved simultaneously by defining the coefficients a_i and b_i as

$$a_2 = a_1 \frac{\langle\Psi_2^\perp|\Psi_3^\perp\rangle}{\langle\Psi_1^\perp|\Psi_3^\perp\rangle} \tag{4.13a}$$

$$b_2 = b_1 \frac{\langle\Psi_2^\perp|\Psi_3^\perp\rangle}{\langle\Psi_1^\perp|\Psi_3^\perp\rangle} \tag{4.13b}$$

$$a_3 = a_1 \frac{\langle\Psi_2^\perp|\Psi_3^\perp\rangle}{\langle\Psi_1^\perp|\Psi_2^\perp\rangle} \tag{4.13c}$$

$$b_3 = b_1 \frac{\langle\Psi_2^\perp|\Psi_3^\perp\rangle}{\langle\Psi_1^\perp|\Psi_2^\perp\rangle}. \tag{4.13d}$$

By substituting these values back into Eq. (4.11), we obtain

$$0 = \langle\Psi_1^\perp|\Psi_2^\perp\rangle + \frac{\langle\Psi_2^\perp|\Psi_3^\perp\rangle}{\langle\Psi_1^\perp|\Psi_3^\perp\rangle}(a_1^2 + b_1^2) \tag{4.14}$$

$$a_1^2 + b_1^2 = -\frac{\langle\Psi_1^\perp|\Psi_2^\perp\rangle\langle\Psi_1^\perp|\Psi_3^\perp\rangle}{\langle\Psi_2^\perp|\Psi_3^\perp\rangle}. \tag{4.15}$$

However, in our particular case, we know that the overlap between each pair of vectors in the set $\{|\Psi_i^\perp\rangle\}$ is equal; as a result, this can be reduced to

$$a_1^2 + b_1^2 = -\langle\Psi_1^\perp|\Psi_2^\perp\rangle. \tag{4.16}$$

Recall that we defined $a_i, b_i \in \mathbb{R}$; thus $a_1^2 + b_1^2 \geq 0$ and we find that the states $\{|D_i\rangle\}$ as defined above can only exist if

$$\langle\Psi_1^\perp|\Psi_2^\perp\rangle \leq 0. \tag{4.17}$$

In order to form our $|D_i\rangle$ states, we choose $b_1 = 0$ for simplicity and thus $a_1 = \sqrt{-\langle\Psi_1^\perp|\Psi_2^\perp\rangle}$ and our discrimination states become

$$|D_i\rangle = |\Psi_i^\perp\rangle + \sqrt{-\langle\Psi_1^\perp|\Psi_2^\perp\rangle}|d+1\rangle. \tag{4.18}$$

The normalised form of these states is

$$|D_i\rangle = \frac{|\Psi_i^\perp\rangle + \sqrt{-\langle\Psi_1^\perp|\Psi_2^\perp\rangle}|d+1\rangle}{(\langle\Psi_i^\perp|\Psi_i^\perp\rangle - \langle\Psi_1^\perp|\Psi_2^\perp\rangle)^2}. \tag{4.19}$$

The inconclusive result $|D_4\rangle$ can then be found using the Gram-Schmidt algorithm on the first three $\{|D_i\rangle\}$ vectors.

For our example of dimension $d = 3$, we end up with the following discrimination states:

$$|D_1\rangle = \sqrt{\frac{2}{6}}|\ell_1\rangle + \frac{1}{\sqrt{6}}\tan\theta|\ell_3\rangle + \sqrt{\frac{3\cos^2\theta - 1}{6}}\sec\theta|\ell_4\rangle \tag{4.20a}$$

$$|D_2\rangle = -\frac{1}{\sqrt{6}}|\ell_1\rangle + \frac{1}{\sqrt{2}}|\ell_2\rangle + \frac{1}{\sqrt{6}}\tan\theta\,|\ell_3\rangle + \sqrt{\frac{3\cos^2\theta - 1}{6}}\sec\theta|\ell_4\rangle \tag{4.20b}$$

$$|D_3\rangle = -\frac{1}{\sqrt{6}}|\ell_1\rangle - \frac{1}{\sqrt{2}}|\ell_2\rangle + \frac{1}{\sqrt{6}}\tan\theta\,|\ell_3\rangle + \sqrt{\frac{3\cos^2\theta - 1}{6}}\sec\theta|\ell_4\rangle \tag{4.20c}$$

$$|D_4\rangle = -\sqrt{\frac{3\cos^2\theta - 1}{2}}\sec\theta|\ell_3\rangle + \frac{1}{\sqrt{2}}\tan\theta|\ell_4\rangle. \tag{4.20d}$$

4.9.4   Angle calculation for fixed overlap

From the definition of the vector $|\Psi_i\rangle$ in Eq. (4.4), we find that the overlap is

$$\langle\Psi_i|\Psi_j\rangle = \sin^2\theta\langle\Psi_i'|\Psi_j'\rangle + \cos^2\theta, \tag{4.21}$$

where we have used that all vectors $|\Psi_i\rangle$ are orthogonal to $|d\rangle$. Using furthermore that all vectors have the same overlap $\langle\Psi_i'|\Psi_j'\rangle = -1/(d-1)$ we find

$$
\begin{aligned}
\langle\Psi_i|\Psi_j\rangle &= \sin^2\theta\left(-\frac{1}{d-1}\right) + \cos^2\theta \\
&= \frac{d\cos^2\theta - 1}{d-1}.
\end{aligned}
\tag{4.22}
$$

In order to obtain states with equal overlap but defined in different dimensions, as we have chosen for Fig. 4(b), we can solve the above equation for θ,

$$
\theta = \cos^{-1}\sqrt{\frac{1}{d}(1 + (d-1)\langle\Psi_i|\Psi_j\rangle)}.
\tag{4.23}
$$

4.9.5   MESD bound in d dimensions

As shown in Ref. [65], the error obtained using MESD to distinguish d states in d dimensions satisfies the inequality

$$
p_{\text{err}} \geq \frac{1}{2}\left(1 - \frac{1}{d-1}\sum_{i=1}^{d}\sum_{j=1}^{i-1}\text{Tr}\,|\eta_i\rho_i - \eta_j\rho_j|\right),
\tag{4.24}
$$

where η_i is the *a priori* probability of generating the state ρ_i and $|X| = \sqrt{X^\dagger X}$.

This expression can be simplified somewhat in our case. Firstly, our *a priori* probabilities η_i are all equal to $1/d$ so that

$$
\text{Tr}\,|\eta_i\rho_i - \eta_j\rho_j| = \frac{1}{d}\text{Tr}\,|\rho_i - \rho_j|.
\tag{4.25}
$$

Secondly, we use only pure states, so that [3]

$$
\text{Tr}\,|\rho_i - \rho_j| = 2\sqrt{1 - |\langle\Psi_i|\Psi_j\rangle|^2}.
\tag{4.26}
$$

Then Eq. (4.24) becomes

$$
p_{\text{err}} \geq \frac{1}{2}\left(1 - \frac{1}{d-1}\sum_{i=1}^{d}\sum_{j=1}^{i-1}\frac{2}{d}\sqrt{1 - |\langle\Psi_i|\Psi_j\rangle|^2}\right).
\tag{4.27}
$$

Since all initial states $\{|\Psi_i\rangle\}$ for a particular angle and dimension have a known equal overlap with one another, the term inside the sum is a constant and can be factored out so that

$$p_{\text{err}} \geq \frac{1}{2}\left(1 - \frac{1}{d-1}\frac{2}{d}\sqrt{1 - |\langle\Psi_i|\Psi_j\rangle|^2}\sum_{i=1}^{d}\sum_{j=1}^{i-1}1\right). \tag{4.28}$$

By evaluating the sum as $\sum_{i=1}^{d}\sum_{j=1}^{i-1}1 = (d^2 - d)/2$, we obtain

$$p_{\text{err}} \geq \frac{1}{2}\left(1 - \sqrt{1 - |\langle\Psi_i|\Psi_j\rangle|^2}\right). \tag{4.29}$$

As the overlap is defined by Eq. (4.22), we finally find the MESD error bound to be

$$p_{\text{err}} \geq \frac{1}{2}\left[1 - \sqrt{1 - \left(\frac{d\cos^2\theta - 1}{d-1}\right)^2}\right]. \tag{4.30}$$

For states that overlap by $\langle\Psi_i|\Psi_j\rangle = 1/\sqrt{2}$, as in Fig. 4(b), this evaluates to $p_{\text{err}} \geq \frac{1}{2}\left(1 - \sqrt{\frac{1}{2}}\right) \approx 0.146$.

4.9.6   OAM values

For dimension d, we require $d+1$ OAM values: d OAM values to form a basis for our states, and one additional OAM value to facilitate our discrimination measurements. As the probability of production of an OAM value decreases in absolute value, it is advantageous to use OAM values closest to zero to obtain greatest signal. The chosen OAM values for several dimensions are shown in Table 4.1.

Dimension d	ℓ-values for states	Ancillary ℓ-value
2	0,1	-1
3	-1,0,1	-2
4	-1,0,1,2	-2
5	-2,-1,0,1,2	-3

Table 4.1: OAM values.

Chapter 5

Summary and Conclusions

In this thesis we have discussed two experiments in quantum optics. In Chapter 3, we demonstrated causal tomography of several different causal structures. We implemented a process that allowed us to select the exact causal structure to prepare, and we proceeded to reconstruct the pseudo-density matrix that provides information about the causal structure. By examining the eigenvalues of the matrix and its partial transpose, we were able to infer some characteristics of the causal structure. This type of tomography functions equally on qubits related by states, processes, or combinations thereof. Future work could focus on the use of causal tomography on a structure in a coherent superposition of direct-cause and common-cause structures. This would mean implementing a two-qubit process that, rather than being a probabilistic mixture of SWAP and identity as in this work, is instead a coherent mixture of SWAP and identity, meaning that the two processes are occurring simultaneously.

In Chapter 4, we demonstrated the unambiguous discrimination of quantum states encoded in high-dimensional bases. We encoded states in the high-dimensional basis of the orbital angular momentum of light, and we performed measurements to determine the state with very low error. These measurements were performed sequentially as projective measurements, reducing the efficiency of the state identification as compared to the use of a POVM. A natural next step would be to perform the measurements simultaneously in a POVM. This could be accomplished using modifications to an OAM mode sorter, which is typically used to sort d orthogonal OAM input states into d orthogonal transverse states. In order to implement our measurements, we would modify the mode sorter to first convert the input states into a $(d+1)$-dimensional basis prior to sorting the new states into $(d+1)$ transverse states.

APPENDICES

Appendix A

Building a displaced Sagnac interferometer

Interferometers are integral to quantum optics as many protocols require intereference between photons. Typically, a Mach-Zehnder interferometer is used, as shown in Fig. A.1. Light enters the interferometer at a beamsplitter and splits into an upper path and a lower path. These paths can be individually manipulated before recombining and interfering at the second beamsplitter.

The problem with this type of interferometer is that it is often quite unstable; in a typical experimental setting, the phase will drift on a timescale between several minutes and an hour. This makes measurement difficult, especially when count rates are low and long integration times are necessary. Active phase stabilisation can be used, but this is often inconvenient and overly complicated.
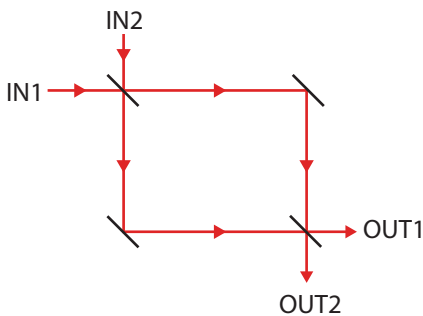
Figure A.1: Mach-Zehnder interferometer.
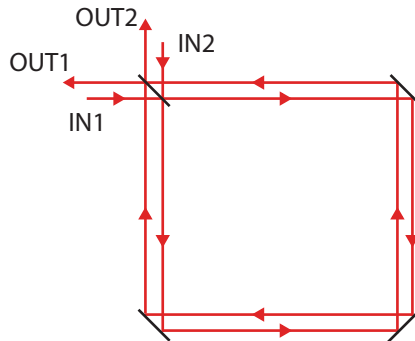
Figure A.2: Displaced Sagnac interferometer.

An alternative solution is to use a displaced Sagnac interferometer [66]. A Sagnac interferometer is similar to a Mach-Zehnder interferometer that has been folded back on itself; the input and output beamsplitters are the same. As a result, rather than an upper and lower path as in the Mach-Zehnder, instead the Sagnac has clockwise-propagating and anticlockwise-propagating paths, as shown in Fig. A.2.

Aligning a displaced Sagnac interferometer is straightforward if done correctly, but if it is done sloppily it will easily result in no interference at all. This is because the beams must run parallel to each other throughout the interferometer; if they are skewed, then it will be difficult to overlap them at the output port. The easiest way to avoid this is to first align the two paths so that they are collinear throughout the interferometer. A cleverly placed translation stage can then make the separation of the beams a quick and easy task.

To build a displaced Sagnac interferometer, you will require two to four apertures for alignment of the beam, one to three translation stages depending on how easy you want things to be, two to three mirrors depending on the desired configuration (we will use three), a non-polarising beamsplitter, a business card, and a camera if available.

Step 1:

- Place the input beam on a stage that allows translation perpendicular to the direction of propagation. This is the only completely necessary translation stage in the setup.

- Place the non-polarising beamsplitter on a mount that allows adjustment of the vertical and horizontal angle. You should make sure that the visible width of the beamsplitter through the mount at a 45° angle is at least equal to the width you will want to displace the beams.
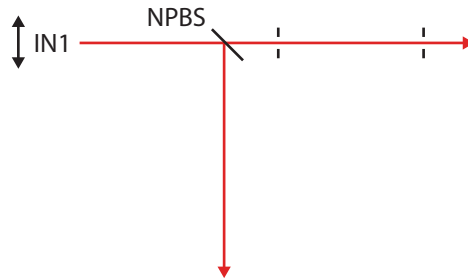
Figure A.3: Step 1.

- Place the NPBS mount on a translation stage if you don't want to pull that much of your hair out. Place the NPBS in the path of the beam at approximately a 45° angle.

- Align the beam to a line of holes using apertures, as shown in Fig. A.3. If you try to do this step without the NPBS in, there will be a slight walkoff when you add the NPBS later. This will take the beam off the line of holes, and you won't notice until the end of the procedure when you wonder how you managed to misalign the very first beam.

Step 2:

- Align the reflection of the NPBS to a line of holes as shown in Fig. A.4.

- Changing the beamsplitter's position adjusts the spot on iris 1; changing the beam-splitter's angle adjust the spot on iris 2.

- This step may need to be iterated with step 1 for perfect alignment.

Step 3:

- Centre a mirror M1 in the path of the first beam at approximately a 45° angle and align to a line of holes as shown in Fig. A.5.

- Changing the mirror's position adjusts the spot on iris 1; changing the mirror's angle adjust the spot on iris 2.

- Obviously this would be easier with a translation stage, but once you're used to it, it only takes about a minute to get a reasonable alignment – the translation stage wouldn't be worth the enormous amount of money it costs.
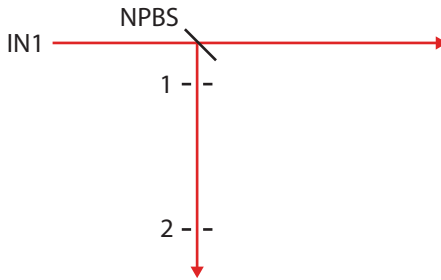
Figure A.4: Step 2.
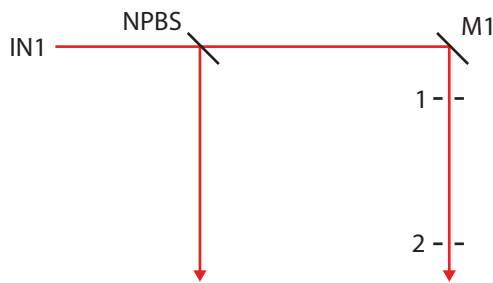
Figure A.5: Step 3.

- After alignment, make sure the beam is still in the centre of the mirror; if it is too far off, then you will run into infuriating problems at the very end and all your work will have come to naught.

Step 4:

- Centre a mirror M2 in the path of the second beam as in Fig. A.6 and do the same as in step 3.

Step 5:

- This step is possibly the most difficult and the most crucial.

- Centre a mirror M3 at the intersection of the two beams. If you have done everything right thus far, the intersection should be directly over a hole.

- Placing M3 on a translation stage is immensely helpful and shortens the job significantly, but if you're struggling for grant money, you can make do without. If you are jittery, I recommend enlisting the help of someone with steady hands and a good constitution.

65
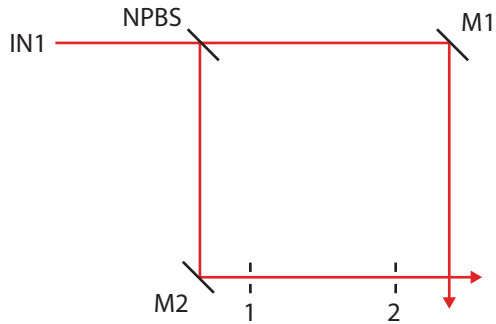
Figure A.6: Step 4.
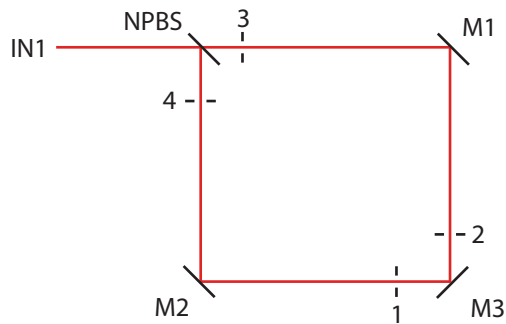
Figure A.7: Step 5.

- Place an aperture in each beam just next to M3 and just next to the NPBS as shown in Fig. A.7.

- Use the position of M3 to align the beams reflecting from M3 to apertures 1 and 2.

- Use the angle of M3 to align the beams reflecting from M3 to apertures 3 and 4.

- Iterate position and angle until all apertures show good alignment. This is where the translation stage comes in handy.

- If you aren't using the translation stage, hang in there! I promise it will work. Listen to soothing music, and be prepared to take breaks if you're frustrated.

Step 6:

- This is the big moment. If you have aligned everything correctly, a simple translation of the input beam should produce a perfect displaced Sagnac as in Fig. A.8.
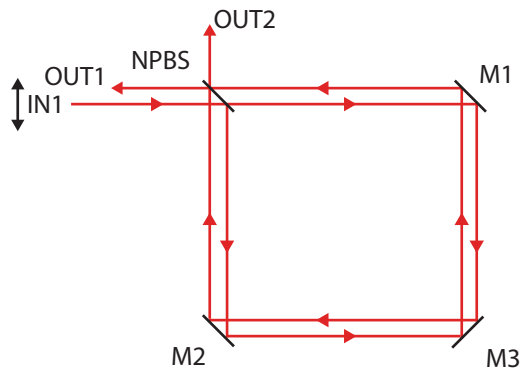
Figure A.8: Step 6.

- Use a business card to check visually at several places around the interferometer that your beams are displaced by a constant amount. Any deviation visible by the eye means something's gone wrong. If it looks fine, though, you should only require minor adjustments to get good interference.

- Image the two output ports on a camera. If you don't have one, I guess you could use optics to enlarge the beam and look at it on a business card.

- You should see fringes at the outputs. Fine adjustment of the horizontal angle of M3 should allow you to extinguish light at output 2 and see no fringes (completely constructive interference) at output 1.

- Adding the second input is straightforward: simply place another beam on a translation stage and perform the same alignment procedure with the second input pointing perpendicular to the first. The first input should be blocked for this to make it easier.

Final notes:

- If you have succeeded, congratulations! If you haven't, there are some issues that might have come up.

- Was there enough room for the light to be displaced in your beamsplitter? If not, it may have been cut off upon displacement. Plate beamsplitters can be placed in lens mounts to maximise the available area – you can get about 1.7 cm this way. Cube beamsplitters should have no problem unless you need to just get a bigger cube.

- Were your beams centred on your mirrors? If not, displacement might have moved one beam completely off the reflective area. You will have to start again from that mirror.

- Is your beamsplitter perfectly 50:50 for each polarisation for the wavelength you're using? If the overall ratio is 50:50, but the individual polarisations have different ratios, then the amplitudes of the different polarisations will not be equal in both ports. In this case, you will not be able to obtain full extinction.

Appendix B

Inferring causal structure: a quantum advantage

B.1   Notes and Acknowledgements

In this appendix, we show in its entirety the manuscript partially based on work described in Chapter 3. Chapter 3 is based on the first draft of this work, but significant changes have taken place in the text, experiments, analysis, and general content. The following section contains significant content contributed by all aforementioned authors and is included for completeness. The content of this appendix is to be submitted for publication:

M. Agnew,* K. Ried,* L. Vermeyden, D. Janzing, R. W. Spekkens, K. J. Resch, Inferring causal structure: a quantum advantage. *These authors contributed equally to this work.*

DJ and RWS conceived the original idea for the project. KR and RWS developed the project and the theory.

MA and KJR designed the experiment.

MA and LV performed the experiment.

MA, KR and KJR performed the numerical calculations.

MA, KR, KJR and RWS analyzed the results.

KR, MA and RWS wrote the first draft of the paper and all authors contributed to the final version.

B.2 Overview

The problem of using observed correlations to infer causal relations is relevant to a wide variety of scientific disciplines. Yet given correlations between just two classical variables, it is impossible to determine whether they arose from a causal influence of one on the other or a common cause influencing both. Only randomized trials can resolve the ambiguity. We here consider the problem of causal inference in quantum theory. We introduce *causal tomography*, which unifies and generalizes conventional quantum tomography schemes to provide a complete solution to the causal inference problem using a quantum analogue of a randomized trial. We furthermore show that, in contrast to the classical case, observed quantum correlations alone can sometimes provide a solution. We implement a quantum-optical experiment that allows us to control the causal relation between two optical modes, and two measurement schemes—one with and one without randomization—that extract this relation from the observed correlations. Our results show that entanglement and coherence, known to be central to quantum information processing, also provide a quantum advantage for causal inference.

B.3 Introduction

"Correlation does not imply causation." This slogan is meant to capture the following fact: it is possible to explain any joint probability distribution over two variables not only by a direct causal influence of one variable on the other, but also by a common cause acting on both. We here address the question of whether a similar ambiguity holds for systems that exhibit quantum effects. We find that, surprisingly, it does not.

Finding causal explanations of observed correlations is a fundamental problem in science, with applications ranging from medicine and genetics to economics [67, 68]. As a practical illustration, consider a drug trial. Naïvely, a correlation between the variables *treatment* and *recovery* may suggest a direct causal influence of the former on the latter. But suppose men are more likely than women to seek treatment, and also more likely to recover spontaneously, regardless of treatment. In this case, gender is a common cause, inducing correlations between treatment and recovery even if there is no direct causal influence.

In order to distinguish between the two possibilities, one must replace *passive observation* of the early variable with an *intervention* upon it. For instance, pharmaceutical companies do not leave the choice of treatment to the subjects of their trials, but carefully

randomize the assignment of drug or placebo. This ensures that the treatment variable is statistically independent of any potential common causes with recovery. Consequently, any correlations with recovery that persist must be due to a direct causal influence. The question of whether there *were* in fact potential common causes can also be answered if one also records whether or not there is a correlation between recovery and the subject's preferred choice of treatment. Thus, the ability to intervene allows for a complete solution of the causal inference problem: it reveals both which variables are causes of which others and, via the strength of the correlations, the precise mathematical form of the causal dependencies.

In this article, we consider the quantum version of this causal inference problem. The challenge is to infer, based on probing the correlations between two temporally ordered quantum systems, whether these correlations are due to a direct causal influence of one system on the other, a common cause acting on both, or a combination of the two possibilities. An additional complication relative to the classical version of the problem is that quantum theory places restrictions on gathering information about systems; for instance, not all observables that can be defined on a system can be measured precisely at the same time. Nonetheless, we show that the ability to intervene on the early quantum system allows for a complete solution. This constitutes a new type of tomography, which subsumes tomography of bipartite states and tomography of processes, and promises applications for determining whether the state evolution implemented by a given device is Markovian. We implement this new type of tomography experimentally and obtain a complete description of the causal structure.

The real surprise, however, is that even if one only has the ability to *passively observe* the early system, the quantum correlations hold signatures of the causal structure—in other words, certain types of correlation *do* imply causation. Differences in the patterns of correlations generated by different causal structures were pointed out recently in [**?**], in the context of extension problems. Fitzsimons, Jones and Vedral [69] defined a function of the observed correlations which acts as a witness of direct causal influence, by ruling out a purely common-cause explanation. We present the larger framework that places this result on an equal footing with an analogous result for common-cause relations. Moreover, we exploit the distinctive properties of quantum correlations to derive, for a particular class of causal scenarios, a *complete solution* of the causal inference problem using passive observation alone—a task that is impossible classically. We implement a family of such scenarios experimentally and show that passive observation is indeed sufficient for solving the causal inference problem in this case.

B.4   The quantum causal inference problem

The two quantum systems whose causal structure we are probing will be denoted A and B, with A preceding B in time. The dynamics relating them may be arbitrarily complicated, involving any number of additional systems and any pattern of interactions among these. Nonetheless, any nontrivial causal relation that is induced between A and B takes one of three forms: A could be a direct cause of B, the two could be influenced by a common cause, or there could be a mixture of the two causal mechanisms (either a probabilistic mixture or a case where both act simultaneously). The three possibilities are depicted in Fig. 1a as directed acyclic graphs and in Fig. 1b as quantum circuits.

A complete solution of the causal inference problem specifies not just the causal structure but also the functional relationship that holds between each system and its causal parents. For instance, this can be achieved by specifying the identity of the gates in the circuits depicted in Fig. 1b. More generally, we aim to specify the functionality of the unknown circuit fragment that relates A and B (the dashed region in Fig. 1b).

A particular example of our causal inference problem is depicted in Fig. 1c. A qubit A is prepared in a maximally entangled state with an ancillary qubit E. Subsequently, A and E are subjected to an unknown quantum operation drawn from a 1-parameter family: a probabilistic mixture of identity, with probability $1 - p$, and swap, with probability p. The case of pure identity corresponds to a purely direct-cause connection between A and B (top), the case of pure swap corresponds to a purely common-cause connection (middle), and every other case corresponds to a hybrid of the two causal structures (bottom).

B.5   Intervention versus passive observation in the quantum realm

The data upon which causal inference will be based is a set of correlations between the outcomes of measurements on A and on B. In an interventionist scheme (depicted in Fig. 2a), A is first measured and then reprepared in a state selected at random. In a passive observation scheme (Fig. 2b), the state of A is updated to be the one found by the measurement, that is, it is updated according to the standard projection postulate. It is useful to adopt a distinct notation for the versions of A before and after the measurement; we denote these by C and D respectively. (The notational convention is natural because if B is correlated with C, it is through a *common* cause, while if it is correlated with D, it is through a *direct* cause. This "splitting" of a variable in order to determine its causal
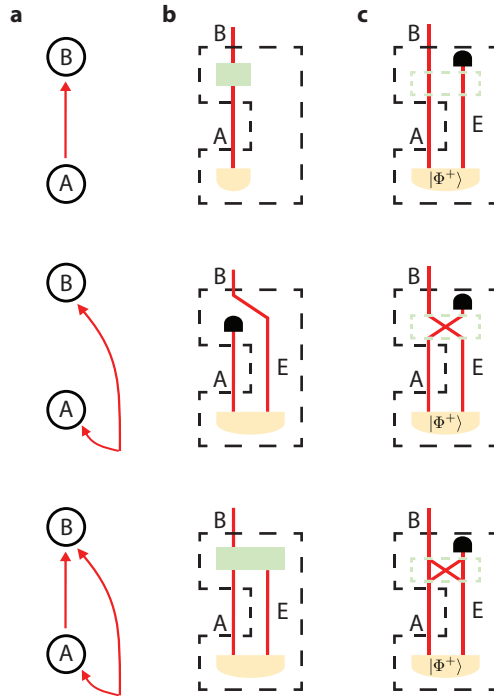
Figure B.1: **The quantum causal inference problem.** We aim to discriminate the three possible causal relations that may hold between a pair of temporally ordered quantum systems: (top to bottom) direct-cause, common-cause or a combination of both. (a) Directed acyclic graphs, where nodes represent quantum systems and directed edges represent causal influences, are the conventional depiction of causal structure in the causal inference literature [67, 68]. (b) Quantum circuits depicting these causal structures, where wires represent quantum systems, and boxes represent operations: gates (green), state preparations (orange) and the operation of discarding the system (black). (c) An example of a family of quantum circuits that range over the three possible causal relations. The gate acting on A and E (dashed green box) is either identity (top), swap (middle) or a probabilistic mixture of the two (bottom).

relations had been proposed for classical variables in [**?**].) The distinction between the two quantum schemes for probing A mirrors the distinction between the two classical schemes in the sense that is relevant for causal inference: while intervention provides independent information about C and D, passive observation provides the same information about C as it does about D.

We will show that the quantum causal inference problem can be completely solved in the interventionist scheme, by performing informationally complete sets of measurements on B and on C and preparations on D. In the passive observation scheme, on the other hand, we are limited to performing an informationally complete set of measurements on B
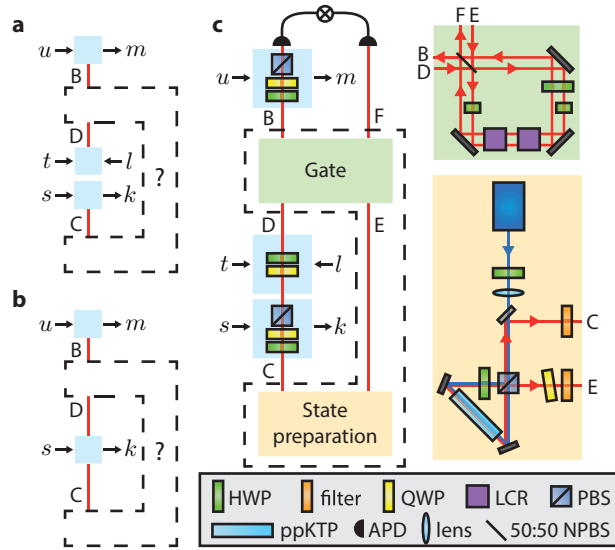
Figure B.2: **Two schemes for probing causal relations and experimental setup.** The unknown circuit fragment enclosed in the dashed box can be probed by two schemes. (a) Interventionist scheme. The outputs B and C are both subjected to tomographically complete sets of measurements, while D is prepared in states drawn from a tomographically complete set. Lowercase variables denote settings and outcomes of these interventions. (b) Passive observation scheme. The outputs B and C are both subjected to tomographically complete sets of measurements. The measurement on C is projective, fixing the preparation on D. (c) Experimental setup including polarization-entangled photon source and probabilistic swap gate. Notation for optical elements: half-wave plate (HWP), quarter-wave plate (QWP), liquid crystal retarder (LCR), polarising beamsplitter (PBS), periodically-poled KTP crystal (ppKTP), avalanche photodiode (APD), and non-polarising beamsplitter (NPBS).

74

and on C, while the preparation of D is determined by the outcome of the measurement on C.

We restrict ourselves to the case where A and B are qubits and use the Pauli observables and Pauli eigenstates as informationally complete sets. Each measurement is described by two classical variables: the setting $\{1, 2, 3\}$, specifying which Pauli observable is measured, and the outcome, $\{\pm 1\}$. We denote these by s and k respectively for the measurement on C, and by u and m for B, as depicted in Figs. 2a and 2b.

In the interventionist scheme (Fig. 2a), system D is prepared in the $l \in \{\pm 1\}$ eigenstate of the $t \in \{1, 2, 3\}$ Pauli observable. Therefore, the experimental data available for causal inference in the interventionist scheme can be represented by the conditional probability distribution $P(km|lstu)$.

For the passive observation scheme, we measure C using the standard quantum state update rule. This can be equivalently understood as a repreparation of D wherein the values of t and l are restricted to be equal to s and k respectively. It follows that the experimental data for causal inference in this case is the conditional probability distribution $P(km|su)$.

B.6   Experiment

We implement the one-parameter family of circuits introduced in Fig. 1c, which ranges through the possible causal structures as we vary the parameter p, using the experimental setup shown in Fig. 2c. The polarization degrees of freedom of a pair of photons constitute the pair of qubits. We use downconversion to create entangled photon pairs in the state $|\Phi^+\rangle = \frac{1}{\sqrt{2}}(|H\rangle|H\rangle + |V\rangle|V\rangle)$, where $|H\rangle$ ($|V\rangle$) denotes horizontal (vertical) polarization. One of the photons, C, is subjected to a polarisation measurement, followed by a repreparation, which yields D. The pair of photons is then subjected to a probabilistic swap gate: with probability p the modes are exchanged; otherwise they are unaffected. The first photon of the output, B, is subjected to a final measurement of its polarisation before both photons are detected in coincidence.

B.7 Mathematical representation of the unknown circuit fragment

The dashed box in Fig. 2a takes one input, D, and produces outputs B and C. It can therefore be represented by a completely positive and trace-preserving (CPTP) map of the form $\mathcal{E}_{CB|D} : \mathcal{L}(\mathcal{H}_D) \to \mathcal{L}(\mathcal{H}_C \otimes \mathcal{H}_B)$, where $\mathcal{L}(\mathcal{H})$ is the space of linear operators on the Hilbert space $\mathcal{H}$. Note, however, that the output C precedes the input D in time. The map $\mathcal{E}_{CB|D}$ must therefore satisfy the additional constraint that C cannot depend on D in any way. We term such an object a *causal map*.

Circuit fragments that do not fall into one of the standard classes (preparations, channels or measurements) have been studied in the context of alternative formulations of quantum theory by a number of authors. All such proposals have been motivated at least in part by the goal of describing causal structure in quantum theory, and many provide a means of describing the circuit fragment that we study. In the quantum combs framework of Chiribella, D'Ariano and Perinotti [70], $\mathcal{E}_{CB|D}$ is a particular type of 2-comb. In the operator tensor formalism of Hardy [71], $\mathcal{E}_{CB|D}$ is an instance of an operator tensor. In the framework of Oreshkov, Costa and Brukner [72], $\mathcal{E}_{CB|D}$ is a particular type of process matrix (one that respects a global causal order). The "multi-time" formalism of Aharonov *et al.* [73] and the general boundary formalism of Robert Oeckl [74] both have objects that would likely be able to describe the causal map $\mathcal{E}_{CB|D}$ were they suitably generalized. It is also possible to understand the causal map $\mathcal{E}_{CB|D}$ as a generalization of the notion of a quantum conditional state in the framework of Leifer and Spekkens [75], which built on earlier work by Leifer [76]. Indeed, it was the latter framework, with its strong connection to the field of causal inference, that served as the primary motivation for the present work.

Note that the causal map $\mathcal{E}_{CB|D}$ incorporates as special cases both bipartite states and unipartite processes. If the structure is purely common-cause (as in Fig. 1b middle), the map will have the form

$$\mathcal{E}_{CB|D}^{\mathrm{cc}} = \rho_{CB} \otimes \mathrm{Tr}_D, \tag{B.1}$$

describing a state on CB and the trace operation on D. Conversely, if the structure is purely direct-cause (as in Fig. 1b top), the map will have the form

$$\mathcal{E}_{CB|D}^{\mathrm{dc}} = \rho_C \otimes \mathcal{E}_{B|D}', \tag{B.2}$$

describing a quantum channel from D to B and a normalized state on C.

More generally, the causal map can describe objects that are neither states nor processes (as in Fig. 1b bottom). For example, if the structure is a probabilistic mixture of common-

cause and direct-cause, we can write

$$\mathcal{E}_{CB|D} = p\mathcal{E}_{CB|D}^{\mathrm{cc}} + (1-p)\mathcal{E}_{CB|D}^{\mathrm{dc}}, \tag{B.3}$$

where the mixing parameter $p \in [0,1]$ interpolates between the extreme cases given in Eqs. (B.1) and (B.2). An even more general form arises if direct-cause and common-cause contributions act at the same time, for instance, if the example of Fig. 1c is modified to allow a family of unitaries that *coherently* interpolate between identity and swap.

B.8 Data analysis in the interventionist scheme

The conditional probability distribution $P(km|lstu)$ obtained in the interventionist scheme is sufficient to tomographically reconstruct the map $\mathcal{E}_{CB|D}$. This is proven in the supplementary material. The key is that the set of preparations on D span $\mathcal{L}(\mathcal{H}_D)$, the real vector space of linear operators on the Hilbert space of D, and the sets of measurements on B and C span $\mathcal{L}(\mathcal{H}_B)$ and $\mathcal{L}(\mathcal{H}_C)$ respectively, so that together they completely characterize the input-output functionality of the map, in the same way that informationally complete sets of preparations and measurements allow conventional tomography of states and processes. We term this scheme *causal tomography* since it achieves a complete solution of the causal inference problem. Considering that the map $\mathcal{E}_{CB|D}$ subsumes bipartite states and processes as special cases, but also describes more general possibilities, causal tomography constitutes a novel, more general scheme that includes conventional tomography as limiting cases.

We apply our scheme to tomographically reconstruct $\mathcal{E}_{CB|D}$ from data obtained in the experiment that implements the interventionist scheme. The resulting maps are presented in Fig. 3a and are found to achieve an average fidelity of 94.5% with the maps that we sought to implement.

Although the reconstructed map constitutes a complete description of the causal mechanism, one is sometimes interested in more coarse-grained information. For instance, for the case of a probabilistic mixture of direct-cause and common-cause mechanisms, learning the value of the mixing parameter p is sufficient to determine the causal structure, if not the exact functional relationships. To estimate p in the interventionist scheme, we fit the experimental data to a map of the form of Eq. (B.3). Fig. 4a shows our best estimate as a function of the value that the experiment sought to implement. Our scheme is shown to extract p with high accuracy, with an rms deviation from the implemented value of only 0.024.
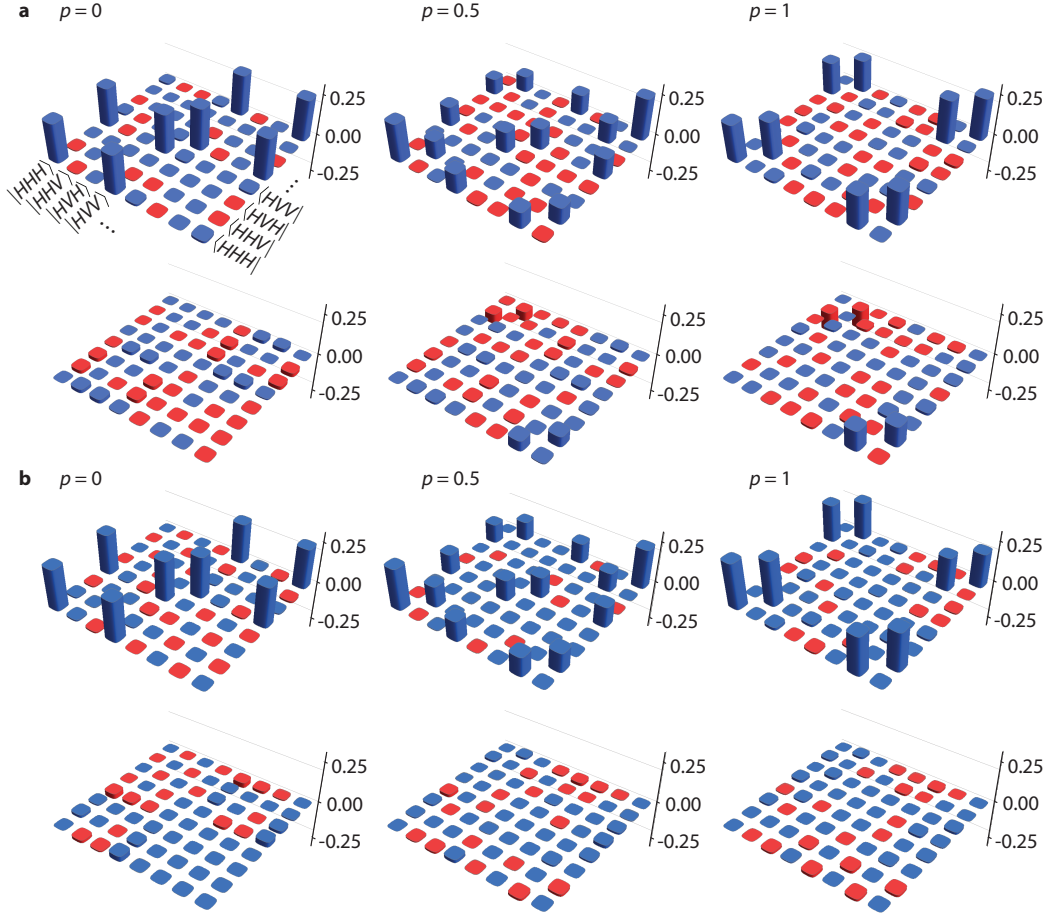
Figure B.3: **Reconstruction of the causal map.** Reconstructions based on (a) the interventionist scheme and (b) the passive observation scheme, for three different causal structures (shown in Fig. 1c), with probability of common cause $p = 0$ (left), $p = 1/2$ (middle) and $p = 1$ (right). We show the Choi representation of the maps [40, 77, 78], which is defined as the tripartite state $\rho_{CBD} \equiv \left(\mathcal{E}_{CB|D'} \otimes \mathbb{1}_D \right) (|\Phi^+\rangle_{D'D}\langle\Phi^+|)$. The arrays represent the real (top) and imaginary (bottom) components of the density matrices, with blue representing positive values and red negative ones. The basis is ordered as CBD, i.e. $|HHH\rangle = |H\rangle_C|H\rangle_B|H\rangle_D$. In the case $p = 0$, we expect a Choi state $\rho_{\exp} = \frac{1}{2}\mathbb{1}_C \otimes |\Phi^+\rangle_{BD}\langle\Phi^+|$, corresponding to the map $\mathcal{E}_{CB|D} = \frac{1}{2}\mathbb{1}_C \otimes \mathcal{I}_{B|D}$ where $\mathcal{I}_{B|D}$ is the identity map. The tomographically reconstructed states, denoted ρ_{fit}, match this expectation with a fidelity $F \equiv \text{Tr}\sqrt{\rho^{1/2}\rho_{\text{fit}}\rho^{1/2}}$ (see [79]) of 98.3% using the interventionist scheme, while passive observation achieves 98.4%. In the case $p = 1$, we expect $\mathcal{E}_{CB|D} = |\Phi^+\rangle_{CB}\langle\Phi^+|\text{Tr}_D$, which has Choi state $|\Phi^+\rangle_{CB}\langle\Phi^+| \otimes \frac{1}{2}\mathbb{1}_D$. The tomographically reconstructed states have fidelity (a) 89.9% and (b) 98.4% with this expected state. We note that the data from the interventionist scheme is best fit by a state on CB that deviates slightly from $|\Phi^+\rangle$, suggesting that the state prepared experimentally did not quite match what we sought to prepare, a fact that is revealed by our causal tomography scheme. Finally, in the case $p = 1/2$, we expect the equal mixture of the two previous cases, which we find with fidelity (a) 95.2% and (b) 96.0%.
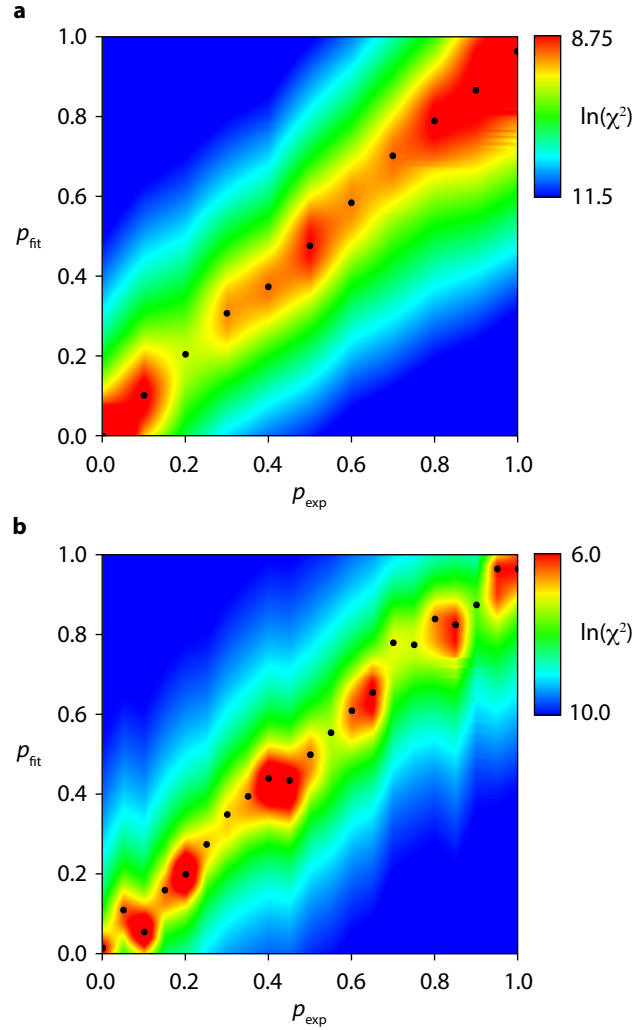
Figure B.4: **Indicators of causal structure determined by interventions and passive observation.** We probe a probabilistic mixture of common-cause, with probability p_{exp}, and direct-cause, using (a) the interventionist scheme or (b) passive observation, and fit to a mixed causal structure with probability of common-cause p_{fit}. Colour encodes the quality of the fit, as measured by the logarithm of the least-squares residue χ^2. The narrow valley of good fit around $p_{\mathrm{fit}} = p_{\mathrm{exp}}$ shows that our analysis recovers the correct value for the probability, thereby identifying the causal structure, with an rms deviation of 0.024 in the interventionist scheme and 0.032 using passive observation.

B.9 Data analysis in the passive observation scheme

Unlike the interventionist scheme, the passive observation scheme does not allow a tomographic reconstruction of the map $\mathcal{E}_{CB|D}$ in an arbitrary causal scenario. This is because, without the randomizing repreparation, the state prepared on D is the same one found in the measurement on C. Therefore, although the measurements on C span the operator space $\mathcal{L}(\mathcal{H}_C)$ and the repreparations of D span $\mathcal{L}(\mathcal{H}_D)$, they do not together span the operator space $\mathcal{L}(\mathcal{H}_C \otimes \mathcal{H}_D)$.

Nonetheless, the correlations that are observed between A and B in the passive observation scheme may still contain a signature of the causal structure, as demonstrated by the simple examples in Table 1. Indeed, it turns out that one can perfectly distinguish any unitary process from any pure maximally entangled bipartite state. If the causal scenario is a probabilistic mixture of these two possibilities, then passive observation allows one to infer the both the probability and the exact nature of the process and the state, thereby affording a complete solution of the causal inference problem (up to one choice of sign). An explicit construction is provided in the supplementary material.

Our experiment implements such a mixture, with the process and the state chosen such as to remove the aforementioned ambiguity, and indeed we obtain a complete solution of the causal inference problem. Fig. 3b displays reconstructions of causal maps from data obtained in the passive observation scheme, which achieve an average fidelity of 97.6%, on par with the results from the interventionist scheme. In Fig. 4b, we plot our best fit for the mixing parameter p based on the data from passive observation, finding an rms deviation of 0.032 from the implemented values, again comparable to what was obtained using the interventionist scheme. Considering that in a classical context, causal inferences about a pair of variables are not possible based on passive observations alone, our results demonstrate a quantum advantage for this problem.

B.10 Discussion

The example from Table I makes use of entangled states and coherent channels. This is not an accident. Common-cause mechanisms that prepare separable states and direct-cause mechanisms that implement entanglement-breaking channels ('measure and reprepare') can be modeled by classical variables. In particular, like their classical counterparts, both produce the same patterns of correlations under passive observation, so that it is not possible to determine the causal structure in these cases. We conclude that entanglement

and coherence are necessary for achieving the quantum advantage in causal inference. In the supplementary material, we show that these conditions are also sufficient if we are promised either a purely common-cause or a purely direct-cause relation between two qubits.

The causal inference schemes described here promise extensive applications in experiments exhibiting quantum effects. For instance, they can provide a test of whether the dynamics of a given open quantum system is Markovian or not [80, 81, 82, 83, 84, 85, 86, 87]. This is because in a non-Markovian evolution, the environment acts as a common-cause between the dynamical system at one time and the same system at a later time. Our inference schemes may also help to detect initial correlations between system and environment, which, if unaccounted for, can lead to errors in the characterization of processes [88, 78, 89, 90, 91, 92].

Our results suggest several interesting avenues for future research. What can be inferred about the map $\mathcal{E}_{CB|D}$ from passive observations alone if one is not promised the particular causal structure we considered here? What can be inferred from measurements that interpolate between passive observation and intervention? How does one generalize such schemes from pairs of systems to arbitrary numbers of systems, for which the possible causal structures are far more varied?

B.11   Methods

We produce polarisation-entangled photons using parametric downconversion in a nonlinear crystal embedded in a Sagnac interferometer [28, 29, 36]. A 10-mW laser with centre wavelength 405 nm propagates through a polarising beamsplitter (PBS), splitting into two components that travel in opposite directions in the Sagnac interferometer. Each component produces degenerate type-II phase-matched downconverted pairs at 809.5 nm in a 10-mm periodically-poled KTP (ppKTP) crystal. There is a half-wave plate (HWP) placed on one side of the crystal so that each component enters the crystal with horizontal polarisation. Upon exiting the interferometer through the PBS, the photon pair is entangled in polarisation. The exact entangled state can be set using a HWP in the pump beam and a quarter-wave plate (QWP) in one of the exiting photon paths; we prepare the maximally entangled state $|\Phi^+\rangle$. In one arm, we separate the pump from the downconverted light using a dichroic mirror. The photons are coupled into single-mode fibres after passing through a bandpass filter to reduce background. We use quantum state tomography to characterise the source and find an average fidelity of 98.5% with $|\Phi^+\rangle$.

Our measurement set consists of horizontal $|H\rangle$ and vertical $|V\rangle$ polarisation, $|D\rangle = \frac{1}{\sqrt{2}}(|H\rangle + |V\rangle)$, $|A\rangle = \frac{1}{\sqrt{2}}(|H\rangle - |V\rangle)$, $|R\rangle = \frac{1}{\sqrt{2}}(|H\rangle + i|V\rangle)$, and $|L\rangle = \frac{1}{\sqrt{2}}(|H\rangle - i|V\rangle)$. We measure polarisation using a polarising beamsplitter (PBS) preceded by a half-wave plate (HWP) and a quarter-wave plate (QWP), which are adjusted so that only one particular eigenstate can pass. By alternating the settings of the wave plates to transmit either one or the other eigenstate of a given Pauli observable in different runs of the experiment, we obtain the same statistics as if we measured in a completely non-destructive manner, which would extract the eigenvalue of the desired Pauli observable while leaving the photon intact.

The experiment requires a gate $\mathcal{G}$ that can faithfully transmit the photon polarisations directly from $D \to B$ and $E \to F$ with probability $1 - p$ and swap the photon polarisations from $D \to F$ and $E \to B$ with probability p. We implement this with the displaced Sagnac interferometer shown in Fig. B.2c [93, 94]. There are two distinct paths in the interferometer: one travelling clockwise, the other travelling anticlockwise. If there is no phase difference between the two paths, the light exits the interferometer at the same side of the beamsplitter at which it entered, with a transverse displacement; if there is a π phase difference, it exits at the opposite side. If light is incident on both input ports of the interferometer, the zero phase shift implements the identity, whilst the π phase shift implements the swap.

This probabilistic switching is implemented using a variable liquid crystal retarder (LCR), whose birefringence can be controlled by an external voltage. A second LCR is included and set to perform the identity operation for compensation. Three half-wave plates at 45° are inserted in the interferometer. The clockwise path encounters the LCR after passing through both waveplates, while the anticlockwise path encounters the LCR *between* the two waveplates. This asymmetry results in the birefringence affecting the two paths differently. When the LCR implements the identity, $\mathbb{1}$, both paths pick up the same phase shift, so the net effect of the gate is the identity. When it implements the phase gate, Z, one path picks up a π phase shift with respect to the other, so the net effect of the gate is the swap. We switch between these two levels of birefringence probabilistically using the random number generator in LabView at a rate of 5 Hz, effectively changing between the identity and swap operations with a chosen probability p.

The experiments proceed as follows. After preparing the entangled state on modes C and E, we measure the polarisation of C. Assuming that the photon passes through the PBS, we can then reprepare it with another QWP and HWP in the desired state for mode D. Light in modes D and E is then sent into the gate $\mathcal{G}$. The output of the gate in mode B is detected using a HWP, QWP, and PBS, and F is directly detected. We detect in coincidence to ensure that the source produced the requisite state. The coincidence

detection is performed using single-photon detectors and coincidence logic with a window of 3 ns. Our coincidence count rate at B and F is approximately 2000 Hz.

B.12 Acknowledgments

B.13 Supplementary Materials

B.13.1 Interventionist scheme

Causal tomography

In this section, we show that the probability distribution obtained in the interventionist scheme, $P(km|lstu)$, completely specifies the causal map $\mathcal{E}_{CB|D}$ describing the unknown circuit fragment (dashed box in Fig. 2a in the main article). The limiting cases of purely common-cause and purely direct-cause relations are discussed in more detail in the next section, showing how the generic scheme reduces to tomography of bipartite states and single-system processes, respectively.

We take $s, t, u \in \{1, 2, 3\}$ to index the three Pauli operators $\{\sigma_1, \sigma_2, \sigma_3\}$ and by extension their eigenbases. The values $k, l, m \in \{+1, -1\}$ specify the eigenstates, and Π_{sk}, Π_{tl}, and Π_{um} denote the projectors onto those eigenstates. Rather than referring directly to the map $\mathcal{E}_{CB|D}$, it is convenient to introduce the Jamiołkowski representation of the map [95, 41, 40, 75]: the operator $\rho_{CB|D} \in \mathcal{L}(\mathcal{H}_C \otimes \mathcal{H}_B \otimes \mathcal{H}_D)$ defined by

$$\rho_{CB|D} = \text{Tr}_{D'}\left[\left(\mathcal{E}_{CB|D'} \otimes \mathbb{1}_{D}\right)\left(|\Phi^+\rangle_{D'D}\langle\Phi^+|^{T_D}\right)\right], \tag{B.4}$$

where T_D denotes the partial transpose on D. (The Choi state, $\rho_{CB|D}$, which we introduced in the main article to represent the map $\mathcal{E}_{CB|D}$, differs from $\rho_{CB|D}$ by a partial transpose

on D and a normalization factor.) One can express the action of the map $\mathcal{E}_{CB|D}$ on an arbitrary state ρ_D in terms of $\rho_{CB|D}$ as

$$\mathcal{E}_{CB|D}(\rho_D) = \mathrm{Tr}_D\left[\rho_{CB|D}(\mathbb{1}_{CB} \otimes \rho_D)\right]. \tag{B.5}$$

Assuming the input system D is prepared in the Pauli eigenstate Π_{tl} and σ_s is measured on C while σ_u is measured on B, the probability of obtaining outcomes k, m can be expressed in terms of the Jamiołkowski operator $\rho_{CB|D}$ as

$$P(km|lstu) = \mathrm{Tr}_{CBD}\left[\rho_{CB|D}(\Pi_{sk}^C \otimes \Pi_{um}^B \otimes \Pi_{tl}^D)\right]. \tag{B.6}$$

It turns out to be convenient to work with the distribution $P(klm|stu)$ rather than $P(km|lstu)$. Given that l is chosen uniformly at random from $\{+1, -1\}$, independently of s, t, or u, the relation between the two is simply

$$P(klm|stu) = \frac{1}{2}P(km|lstu). \tag{B.7}$$

In essence, one can think of the preparation of D as a filtering-type measurement of the Pauli observable σ_t acting on the maximally mixed state on D. In this scenario, it is natural to consider the joint distribution of outcomes for three measurements, $P(klm|stu)$.

Eqs. (B.6) and (B.7) imply that from $P(klm|stu)$ we can determine the components of $\rho_{CB|D}$ on the basis of operator space $\mathcal{L}(\mathcal{H}_C \otimes \mathcal{H}_B \otimes \mathcal{H}_D)$ formed by the Pauli operators, $\sigma_s^C \otimes \sigma_u^B \otimes \sigma_t^D$, for $s, t, u \in \{1, 2, 3\}$. We refer to these components as correlators and denote them C_{stu},

$$\begin{aligned} C_{stu} &\equiv \mathrm{Tr}\left[\rho_{CB|D}(\sigma_s^C \otimes \sigma_u^B \otimes \sigma_t^D)\right] \\ &= 2\sum_{k,l,m=\pm 1} klm\, P(klm|stu). \end{aligned} \tag{B.8}$$

To reconstruct $\rho_{CB|D}$, however, we need to have its components relative to a complete basis of the operator space. Such a basis is provided by products of the set of Pauli operators, if the latter is taken to include the identity operator. Defining $\sigma_0 = \mathbb{1}$ and introducing variables s', t', u' with range $\{0, 1, 2, 3\}$, the set of product operators $\sigma_{s'}^C \otimes \sigma_{t'}^D \otimes \sigma_{u'}^B$ provides a complete basis. We again refer to the components in this basis as correlators, and denote them $C_{s't'u'}$,

$$C_{s't'u'} \equiv \mathrm{Tr}\left[\rho_{CB|D}(\sigma_{s'}^C \otimes \sigma_{u'}^B \otimes \sigma_{t'}^D)\right], \tag{B.9}$$

where $s', t', u' \in \{0, 1, 2, 3\}$.

The cases wherein one of s', t', u' is zero while the other two are in $\{1, 2, 3\}$ describe correlations between Pauli observables for a pair of systems, for instance, $C_{s0u} \equiv \mathrm{Tr}_{CBD}$ $\left[\rho_{CB|D} (\sigma_s^C \otimes \sigma_u^B \otimes \mathbb{1}_D) \right]$ for $s, u \in \{1, 2, 3\}$. Note that the marginal of $P(klm|stu)$ on any two outcome variables is independent of the value of the setting variable for the third: $P(kl|stu) = P(kl|st)$, $P(km|stu) = P(km|su)$, and $P(lm|stu) = P(lm|tu)$. The only subtle case is the second one, which follows from the fact that l is chosen uniformly at random, such that the state on D when one is not conditioning on l is independent of t, $\sum_l \frac{1}{2} \Pi_{t,l} = \frac{1}{2} \mathbb{1}$. It follows that the correlators in question can be expressed as:

$$C_{s0u} = 2 \sum_{k,m=\pm 1} km \, P\left(km|su\right),$$

$$C_{0tu} = 2 \sum_{l,m=\pm 1} lm \, P\left(lm|tu\right),$$

$$C_{st0} = 2 \sum_{k,l=\pm 1} kl \, P\left(kl|st\right). \tag{B.10}$$

Furthermore, since C precedes D in time, it cannot depend on D. Hence $P(kl|st) = P(k|s)P(l|t)$, and, given that l is chosen uniformly at random, we find that $C_{st0} = 0$.

The cases wherein two of s', t', u' are zero and only one is in $\{1, 2, 3\}$ describe marginal expectations for Pauli observables, for instance, $C_{s00} \equiv \mathrm{Tr}_{CBD} \left[\rho_{CB|D} (\sigma_s^C \otimes \mathbb{1}_B \otimes \mathbb{1}_D) \right]$ for $s \in \{1, 2, 3\}$. As before, the marginal on a single outcome variable is independent of the other two setting variables: $P(k|stu) = P(k|s)$, $P(l|stu) = P(l|t)$, and $P(m|stu) = P(m|u)$. Again, the only subtle case is the second one, which follows from the fact that l is chosen uniformly at random. The correlators can therefore be expressed as:

$$C_{s00} = 2 \sum_{k=\pm 1} k \, P\left(k|s\right),$$

$$C_{0t0} = 2 \sum_{l=\pm 1} l \, P\left(l|t\right),$$

$$C_{00u} = 2 \sum_{m=\pm 1} m \, P\left(m|u\right). \tag{B.11}$$

The fact that l is chosen uniformly at random also implies that $C_{0t0} = 0$ for all t.

Finally, from the fact that $\mathcal{E}_{CB|D}$ is trace-preserving, it follows that $\mathrm{Tr}_{CB} \rho_{CB|D} = \mathbb{1}_D$, so that $\mathrm{Tr}_{CBD} \left[\rho_{CB|D} \right] = 2$, and hence

$$C_{000} = 2. \tag{B.12}$$

85

Thus each of the correlators $C_{s't'u'}$ can be calculated from the measured statistics. Because the Pauli operators form an orthogonal basis of the operator space relative to the Hilbert-Schmidt inner product, we can invert Eq. (B.9) and reconstruct $\rho_{CB|D}$ via

$$\rho_{CB|D} = \frac{1}{8} \sum_{s',t',u'=0}^{3} C_{s't'u'} \sigma_{s'}^{C} \otimes \sigma_{u'}^{B} \otimes \sigma_{t'}^{D}. \tag{B.13}$$

The map $\mathcal{E}_{CB|D}$ is then recovered from $\rho_{CB|D}$ using Eq. (B.5).

We refer to this scheme, by which the causal map $\mathcal{E}_{CB|D}$ is reconstructed from the measurement statistics, as *causal tomography*.

Special cases: tomography of processes and bipartite states

This section describes how causal tomography reduces to tomography of bipartite states and tomography of single-system processes in the cases where the causal structure is purely common-cause and purely direct-cause respectively.

In the case of a purely common-cause relation, neither B nor C depend on which state Π_{lt} is prepared on D, so that

$$P(klm|stu) = P(km|su). \tag{B.14}$$

It follows that there are no triple-wise correlations, $C_{stu} = 0$. We already found that, since D has no influence on C, $C_{st0} = 0$ and $C_{0t0} = 0$. Furthermore, the lack of a causal connection between D and B in the purely common-cause case implies $P(lm|stu) = \frac{1}{2}P(m|u)$, and consequently $C_{0tu} = 0$. Consequently, the only nonzero correlators for the purely common-cause scenario are those of the form $C_{s'0u'}$. Hence, the correlators can be expressed as $C_{s't'u'} = 2\delta_{t',0}C_{s'u'}$, with

$$
\begin{aligned}
C_{su} &\equiv \sum_{k,m=\pm 1} km\, P(km|su), \\
C_{s0} &\equiv \sum_{k=\pm 1} k\, P(k|s), \\
C_{0u} &\equiv \sum_{m=\pm 1} m\, P(m|u), \\
C_{00} &\equiv 1.
\end{aligned}
\tag{B.15}
$$

The reconstruction presented in Eq. (B.13) yields

$$\rho_{CB|D} = \rho_{CB} \otimes \mathbb{1}_D, \tag{B.16}$$

with

$$\rho_{CB} = \frac{1}{4} \sum_{s'u'=0}^{3} C_{s'u'} \sigma_{s'}^{C} \otimes \sigma_{u'}^{B}, \tag{B.17}$$

which is precisely the expression for the tomographic reconstruction of a two-qubit state from the correlators between Pauli operators on the two qubits.

In the limiting case of a purely direct-cause relation, C is not correlated with B or D: the probability distribution factorizes into

$$P(klm|stu) = P(k|s) P(lm|tu), \tag{B.18}$$

so the correlators factor as $C_{s't'u'} = C_{s'}C_{t'u'}$, with

$$
\begin{aligned}
C_{tu} &= 2 \sum_{l,m=\pm 1} lm \, P(lm|tu), \\
C_{t0} &= 2 \sum_{l=\pm 1} l \, P(l|t), \\
C_{0u} &= 2 \sum_{m=\pm 1} m \, P(m|u), \\
C_{00} &= 2, \\
C_{s} &= \sum_{k=\pm 1} k \, P(k|s), \\
C_{0} &= 1.
\end{aligned}
\tag{B.19}
$$

Note that $C_{t0} = 0$ for all t because l is chosen uniformly at random.

From these correlators, one reconstructs a conditional of the form

$$\rho_{CB|D} = \rho_C \otimes \rho_{B|D}. \tag{B.20}$$

where

$$\rho_C = \frac{1}{2} \sum_{s'=0}^{3} C_{s'} \sigma_{s'}, \tag{B.21}$$

and

$$\rho_{B|D} = \frac{1}{4} \sum_{t'u'=0}^{3} C_{t'u'} \sigma_{t'}^{D} \otimes \sigma_{u'}^{B}. \tag{B.22}$$

Clearly, Eq. (B.21) is the standard expression for the tomographic reconstruction of a qubit state from the expectation values of the Pauli operators. Meanwhile, Eq. (B.22) is the expression for the tomographic reconstruction of the Jamiołkowski representation of a single-qubit process. Denoting the completely positive trace-preserving map associated with this proces by $\mathcal{E}'_{B|D}$, its action can be expressed in terms of $\rho_{B|D}$ using the standard Jamiołkowski isomorphism, $\mathcal{E}'_{B|D}(\rho_D) = \text{Tr}_D\left[\rho_{B|D}(\mathbb{1}_B \otimes \rho_D)\right]$.

B.13.2   Passive observation

Signatures of causal structure

This section considers two possible causal structures: either D has a direct causal influence on B, or C and B are connected by a common cause. We derive properties of the measurement statistics that reflect the underlying causal structure.

In the passive observation scheme, we perform a projective measurement on C, with rank-one projectors Π_{sk}^C indexed by the setting s and the outcome k. The measurement obeys the projection postulate, so that the state on D after a measurement of s yielding k is given by the same projector, Π_{sk}^D. The late system, B, is probed by a measurement with projectors Π_{um}^B, with settings u and outcomes m. We can therefore relate the joint probability distribution over measurement outcomes, $P(km|su)$, to the causal map $\mathcal{E}_{CB|D}$ by

$$P(km|su) = \text{Tr}_{BC}\left(\Pi_{um}^B \otimes \Pi_{sk}^C \mathcal{E}_{CB|D}(\Pi_{sk}^D)\right). \tag{B.23}$$

In the case where the relation is purely common-cause, the causal map reduces to the form

$$\mathcal{E}_{CB|D}^{\text{cc}} = \rho_{CB} \otimes \text{Tr}_D, \tag{B.24}$$

for some bipartite state ρ_{CB}. It follows that in this case,

$$P(km|su) = \text{Tr}_{BC}\left(\Pi_{sk}^C \otimes \Pi_{um}^B \rho_{CB}\right), \tag{B.25}$$

which is simply the standard expression for joint statistics obtained from measurements on a pair of quantum systems.

Similarly, noting that the projectors that constitute the measurement sum to identity, $\sum_m \Pi_{um} = \mathbb{1} \,\forall u$, we find the marginal distribution over k to be

$$P(k|su) = \text{Tr}_C\left(\Pi_{sk}^C \rho_C\right) = P(k|s), \tag{B.26}$$

88

which is simpliy the probability distribution that we would expect from the marginal state $\rho_C \equiv \mathrm{Tr}_B\rho_{CB}$. We will see below that the same marginal distribution is produced by a direct-cause structure, and can therefore not serve as an indicator of causal structure. Instead, we use the chain rule,

$$P(km|su) = P(m|ksu)P(k|su), \tag{B.27}$$

to isolate the conditional probability $P(m|ksu)$ of finding outcome m in a measurement on B, conditioned on the measurement on C finding Π_{sk}.

In order to obtain a simple expression for the conditional probability distribution, we define the *conditional quantum state*, as introduced in Ref. [75]: a bipartite operator, $\rho_{B|C} \in \mathcal{L}(\mathcal{H}_C \otimes \mathcal{H}_B)$, given by

$$\rho_{B|C} \equiv \left(\rho_C^{-\frac{1}{2}} \otimes \mathbb{1}_B\right) \rho_{CB} \left(\rho_C^{-\frac{1}{2}} \otimes \mathbb{1}_B\right), \tag{B.28}$$

in terms of which the conditional probability distribution is simply

$$P(m|ksu) = \mathrm{Tr}_{CB}\left(\Pi_{sk}^C \otimes \Pi_{um}^B\rho_{B|C}\right). \tag{B.29}$$

The operator $\rho_{C|B}$ is called the *acausal* conditional state in Ref. [75], to textitasize the fact that it does not describe a (direct) causal influence. Neverthelss, it encodes a rule of inference, namely what one can infer about B if one finds a certain state on C. This sort of state update rule has been studied under the name of steering [96] and the general form of the affine map $\mathcal{E}_{B|C}$ which is Jamiołkowski isomorphic to $\rho_{B|C}$ is described in proposition V.1 of Ref. [75].

By its definition, $\rho_{B|C}$ clearly satisfies the quantum analogue of the law of total probability $\mathrm{Tr}_C\rho_{B|C} = \mathbb{1}_C$, which corresponds to the fact that the steering map $\mathcal{E}_{B|C}$ is trace-preserving. More importantly, like the bipartite state ρ_{CB} from which it is derived, the conditional $\rho_{B|C}$ is positive semi-definite. That is, the steering map $\mathcal{E}_{B|C}$ is not completely positive in general, but its composition with the partial transpose on C, $\mathcal{E}_{B|C} \circ T_C$, is a completely positive map. We conclude that if the statistics $P(m|ksu)$ *cannot* be cast in the form of Eq. (B.29) for such an operator, then they can not be explained by common-cause alone, indicating that there must be at least some measure of direct causal influence as well.

In the purely direct-cause scenario, the causal map is of the form

$$\mathcal{E}_{CB|D}^{\mathrm{dc}} = \rho_C \otimes \mathcal{E}_{B|D}, \tag{B.30}$$

for some quantum channel $\mathcal{E}_{B|D}$ and some state ρ_C. It follows that in this case,

$$P(km|su) = \mathrm{Tr}_C\left(\Pi_{sk}^C \rho_C\right) \mathrm{Tr}_{BD}\left(\Pi_{um}^B \mathcal{E}_{B|D}(\Pi_{sk}^D)\right). \tag{B.31}$$

Tracing over the output of the channel, B, gives $\mathrm{Tr}_B\left(\mathcal{E}_{B|D}(\Pi_{sk}^D)\right) = 1$ regardless of the input Π_{sk} on D, so the marginal probability distribution over k becomes

$$P(k|su) = \mathrm{Tr}_C\left(\Pi_{sk}^C \rho_C\right) = P(k|s), \tag{B.32}$$

which depends only on the marginal state ρ_C, as it did in the common-cause scenario. The conditional distribution in the direct-cause case is therefore given by

$$P(m|ksu) = \mathrm{Tr}_{BD}\left(\Pi_{um}^B \mathcal{E}_{B|D}(\Pi_{sk}^D)\right), \tag{B.33}$$

determined entirely by the channel $\mathcal{E}_{B|D}$.

In order to facilitate the comparison with the common-cause scenario, we express the conditional probability in terms of the Jamiołkowksi operator of the channel $\mathcal{E}_{B|D}$:

$$P(m|ksu) = \mathrm{Tr}_{BD}\left(\Pi_{um}^B \otimes \Pi_{sk}^D \rho_{B|D}\right), \tag{B.34}$$

which closely parallels the form of Eq. (B.29). Operators like $\rho_{B|D}$ are introduced in Ref. [75] as *causal* conditional states. Like acausal conditionals above, in order to represent a trace-preserving map, they satisfy the law of total probability,

$$\mathrm{Tr}_B \rho_{B|D} = \mathbb{1}_D. \tag{B.35}$$

However, in order to represent a *completely positive* map, $\rho_{B|D}$ must have a positive partial transpose (PPT) rather than being positive itself. This is the key difference from the common-cause case, which ultimately allows us to distinguish the two scenarios. Specifically, if the statistics $P(m|ksu)$ *cannot* be cast in the form of Eq. (B.34) for a PPT operator $\rho_{B|D}$, then they cannot be explained by a purely direct-cause mechanism, indicating that there must be at least some measure of common cause as well.

To summarize, if the observed statistics cannot be put in the form (B.29) with ρ_{CB} positive semi-definite, then they do not admit of an explanation purely in terms of a common cause, while if they cannot be put in the form of (B.31), with $\rho_{B|D}$ PPT, then they do not admit of an explanation purely in terms of a direct cause. Hence, properties of the observed statistics can not only witness the impossibility of a common cause explanation, as noted in Ref. [69], they can also witness the impossibilty of a direct cause explanation. It is in this sense that the observed statistics in a passive observation scheme contain signatures

of the causal structure. Note that this analysis applies regardless of the dimension of the Hilbert spaces describing the systems.

It is interesting to note that, if C and B are related by a common cause, then the marginal probability distributions over the outcomes of both measurements, k and m, are independent of the setting of the respective other measurement: it follows from Eq. (B.25) that

$$
\begin{align}
P(k|su) &= P(k|s), \tag{B.36}\\
P(m|su) &= P(m|u). \tag{B.37}
\end{align}
$$

This captures the impossibility of signalling between two systems that are not connected by a direct-cause link.

In the direct-cause case, Eq. (B.34) implies that

$$
P(k|su) = P(k|s), \tag{B.38}
$$

that is, the outcomes of measurements on C are independent of the setting at B, which is a consequence of the fact that C is prior to B in time. However, the marginal distribution over the outcome at B

$$
P(m|su) = \sum_k \operatorname{Tr}_C \left(\Pi^C_{sk} \rho_C \right) \operatorname{Tr}_{BD} \left(\Pi^B_{um} \mathcal{E}_{B|D}(\Pi^D_{sk}) \right), \tag{B.39}
$$

is generally *not* independent of the measurement setting s at C, allowing one to signal via the direct-cause connection.

In the conetext of causal inference, observing such signalling ($P(m|su) \neq P(m|u)$) allows one to trivially conclude that there must be at least some measure of direct causal influence. Conversely, if we wish to study the case wherein the quantum causal inference prblem is nontrivial, we can restrict ourselves to situations that preclude signalling. Namely, if one has no prior kowledge of C, so that ρ_C is the maximally mixed state, $\rho_C = \frac{1}{d_C}\mathbb{1}_C$, then $P(k|s) = \frac{1}{d_C}$ and consequently

$$
\begin{align}
P(m|su) &= \frac{1}{d_C}\operatorname{Tr}_B \left(\Pi^B_{um} \mathcal{E}'_{B|D}(\sum_k \Pi^D_{sk}) \right) \\
&= \frac{1}{d_C}\operatorname{Tr}_B \left(\Pi^B_{um} \mathcal{E}'_{B|D}(\mathbb{1}_D) \right) \tag{B.40}
\end{align}
$$

which implies

$$
P(m|su) = P(m|u). \tag{B.41}
$$

91

The latter condition asserts that there is no possibility of signalling by choosing the setting s and observing the outcome m. On the other hand, if ρ_C is not the maximally mixed state, different measurement settings s give rise to different distributions $P(k|s)$, which ultimately allow signalling. Thus, for the purpose of causal inference, we can restrict ourselves to the case of ρ_C maximally mixed, since otherwise the problem admits a trivial solution.

Furthermore, if we consider a probabilistic mixture of common-cause and direct-cause relations,

$$\rho_{CB|D} = p\rho_{CB} \otimes \mathbb{1}_D + (1-p)\rho_C \otimes \rho_{B|D}, \tag{B.42}$$

and the marginal ρ_C of the direct-cause component is assumed to be maximally mixed so as to prevent signalling, then we can also assume that the marginal of the bipartite state, $\mathrm{Tr}_B \rho_{CB}$, is maximally mixed. If this were not the case, the marginal statistics $P(k|s)$ would be sufficient to distinguish the two causal scenarios. (The marginal state on B in both the direct-cause and common-cause cases remains arbitrary and therefore the marginal statistics $P(m|u)$ cannot distinguish the two cases either.)

To summarize, in the nontrivial version of the quantum causal inference problem, the conditional independences that hold in the direct-cause scenario, Eqs. (B.38) and (B.41), are precisely the same as those that hold in the common-cause scenario, Eqs. (B.36) and (B.37), and the possibilities for the marginal statistics $P(k|s)$ and $P(m|u)$ are also precisely the same in the two scenarios. The nontrivial version of the problem is the one wherein the signature of the causal structure must be found in the form of the correlations, encoded in $P(m|ksu)$, alone.

Reconstruction of the causal map given a promise

We now demonstrate that in the passive observation scheme one can sometimes achieve a complete solution of the quantum causal inference problem. More specifically, we show that if the systems are qubits and one is promised that the unkown circuit fragment is a probabilistic mixture of a direct cause mechanism associated with a unitary and a common-cause mechanism associated with a pure maximally entangled state, then passive observation is sufficient to solve the problem (up to a binary ambiguity in the general case).

As discussed in the previous section, causal inference based on passive observation relies on the conditional probability distribution $P(m|ksu)$. In the case of a probabilistic mixture of common-cause and direct-cause, this can be expressed in terms of two conditional quantum states, $\rho_{B|C}$ and $\rho B|D$, as

$$
\begin{aligned}
P(m|ksu) &= p\mathrm{Tr}_{BC}\left(\Pi_{um}^B \otimes \Pi_{sk}^C \rho_{B|C}\right) \\
&+ (1-p)\tfrac{1}{2}\mathrm{Tr}_{BD}\left(\Pi_{um}^B \otimes \Pi_{sk}^D \rho_{B|D}\right).
\end{aligned}
\tag{B.43}
$$

The promise that defines our more restricted causal inference problem is: (i) the bipartite state that gives rise to the common-cause conditional, ρ_{BC}, is pure and maximally entangled. (In the context of the constraint that ρ_{BC} has a maximally mixed marginal on C, we note that $\rho_{B|C} = \rho_{CB}$, and it is sufficient to demand that ρ_{BC} be maximally entangled.), and (ii) $\rho_{B|D}$ describes a unitary process. Achieving a complete solution of the causal inference problem in this case corresponds to determining $\rho_{B|C}$, $\rho_{B|D}$ and the value of the mixing parameter p. Here we derive an explicit and unique (up to one choice of sign) solution to this problem. The analysis refers only to qubits, because some steps do not apply to higher dimensions (such as the Bloch sphere representation and Euler's rotation theorem).

Our proof technique is formulated in terms of a particular representation of single-qubit processes and the steering associated with two-qubit states [97], namely the effect that they have on the Bloch sphere. Both cases correspond to an affine transformation that rotates and scales the Bloch vectors, and, in the case of non-unital processes and non-maximally entangled states respectively, introduces an offset. This representation can be easily visualized: for each point on the Bloch sphere, one plots the corresponding point in the Bloch sphere that is the image of the first point under the map, resulting in an ellipsoid. In order to describe the map completely, the ellipsoid can be colour-coded: the colour of a point on the ellipsoid indicates which point on the Bloch sphere it is the image of, for instance the image of $|+x\rangle$ is coloured red, the image of $|-x\rangle$ is cyan (anti-red), green for $|+y\rangle$ and so on.

An analytical description of the affine transformation is provided by the components in the Pauli basis of the Jamiołkowski-isomorphic operator to the map. For the direct-cause case,

$$\Theta_{s'u'} \equiv \mathrm{Tr}\left(\rho_{B|D}\sigma_{s'}^D \otimes \sigma_{u'}^B\right), \tag{B.44}$$

and for the common-cause case,

$$\Theta_{s'u'} \equiv \mathrm{Tr}\left(\rho_{B|C}\sigma_{s'}^C \otimes \sigma_{u'}^B\right), \tag{B.45}$$

where $s', u' \in \{0, 1, 2, 3\}$ index the basis elements $\{\mathbb{1}, \sigma_1, \sigma_2, \sigma_3\}$.

The components $\{\Theta_{0,u}\}_{u=1,2,3} \equiv \vec{c}$ encode the offset of the centre of the ellipsoid. In the direct-cause case, this Bloch vector describing the image under the quantum channel of the maximally mixed state. In the common-cause case, it is the Bloch vector describing the state on B unconditioned on any measurement outcome on C. For the unitary channels and maximally entangled states that we are considering, $\vec{c}$ is the zero vector.

The components with non-zero indices define the matrix

$$T \equiv \{\Theta_{su}\}_{s,u=1,2,3}, \tag{B.46}$$

which encodes the rotations and scaling. More specifically, it can be shown that the directions of the axes of the ellipsoid are given by the eigenvectors of TT^T, and their lengths by the square roots of its eigenvalues.

In this context, we term a single-qubit channel or a two-qubit state *extremal* if its ellipsoid coincides with the unit sphere. In the case of channels, this is a well-known constraint: it implies that the channel must introduce no noise, but rather implements a pure rotation described by a unitary operator. Meanwhile, two-qubit states whose steering ellipsoid is the full sphere are pure and maximally entangled.

In the extremal case, the distinction between states and processes is simple: extremal processes correspond to proper rotations of the Bloch sphere, with $\det T = +1$. If the colour-coding is such that the triad red-green-blue is right-handed on the input sphere, then the coloured sphere describing the output of the channel will have that same handedness. Extremal *states*, on the other hand, produce steering ellipsoids whose colour distribution has the opposite handedness to the input sphere, being reached by an improper rotation, with $\det T = -1$. (This can be seen algebraically as follows: partial transposition, which maps the set of causal conditional state to the set of acausal conditional states, simply changes the sign of terms involving σ_2, which implies multiplying the T matrix by $diag\{+1, -1, +1\}$.) The examples discussed in Table 1 are instances of extremal states and processes.

Before turning to a probabilistic mixture of a generic extremal process and a generic extremal state, consider how the two are related. Let the matrices T_{dc}, T_{cc} encode their respective effects on the Bloch sphere, and note that T_{dc} can be transformed into T_{cc} in two steps: reflection through the origin, which we denote by F, and rotation about some particular axis $\hat{n}$ by some particular angle. We write the angle as $\pi + \gamma$, so that the rotation can be decomposed into $R_{\hat{n},\pi}$ followed by $R_{\hat{n},\gamma}$. Thus

$$T_{cc} = R_{\hat{n},\gamma} R_{\hat{n},\pi} F T_{dc}. \tag{B.47}$$

After the first step, the image of each point on the surface of the sphere under FT_{dc} is diametrically opposed to its image under T_{dc} alone. Under the rotations, the two points whose images lie at $\pm\hat{n}$ remain opposites. Meanwhile, the images in the plane orthogonal to $\hat{n}$ coincide again after the π rotation. Once we include the final rotation by γ, there will be an offset by γ between the images of T_{dc} and T_{cc} in the plane orthogonal to $\hat{n}$, while their images along $\hat{n}$ are diametrically opposed.

Now consider a probabilistic mixture of the two extremal cases. By linearity, it is associated to a matrix

$$T_m \equiv (1-p)T_{dc} + pT_{cc}. \tag{B.48}$$
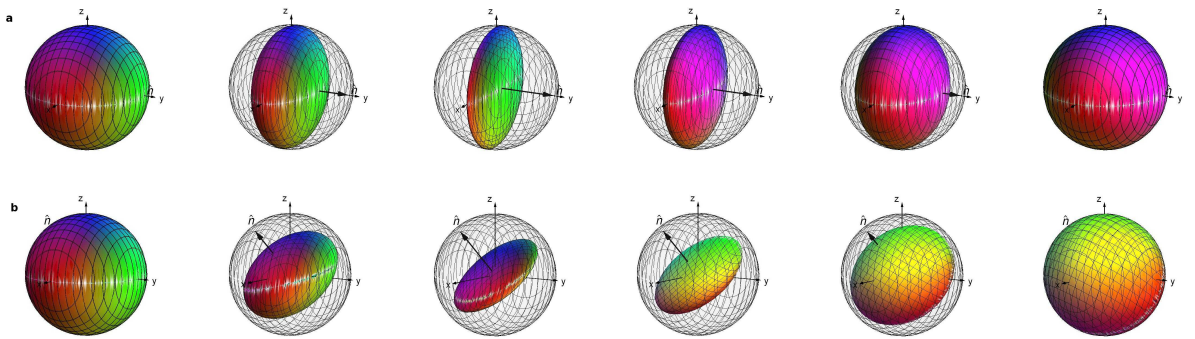
Figure B.5: **Bloch sphere representation of a probabilistic mixture of a unitary process and a pure, maximally entangled state.** The image of the Bloch sphere under an affine map is an ellipsoid, with colours distinguishing the images of different inputs: red denotes the image of $|+_x\rangle$, cyan (anti-red) for $|-_x\rangle$, green for $|+_y\rangle$ and so on. Unitary processes correspond to a unit sphere with the colours distributed such that the triad red-green-blue right-handed, such as the identity channel, on the far left, while pure, maximally entangled states correspond to unit spheres with a left-handed distribution, as they appear on the far right. Mixtures of the two extremes (shown for probability of common-cause $p = 0.00, 0.25, 0.45, 0.65, 0.85, 1.00$, from left to right) produce ellipsoids that are flattened in the direction $\hat{n}$ (thick arrow) to a height $2|1 - 2p|$, and rotationally symmetric in the plane orthogonal to $\hat{n}$, with radius r. (a) A mixture of the identity channel and the state $|\Phi^+\rangle$, as realized in our experiment, produces a radius $r = 1$ throughout the transition. (b) Mixing the identity channel with a generic pure, maximally entangled state produces intermediate ellipsoids with radius $r < 1$.
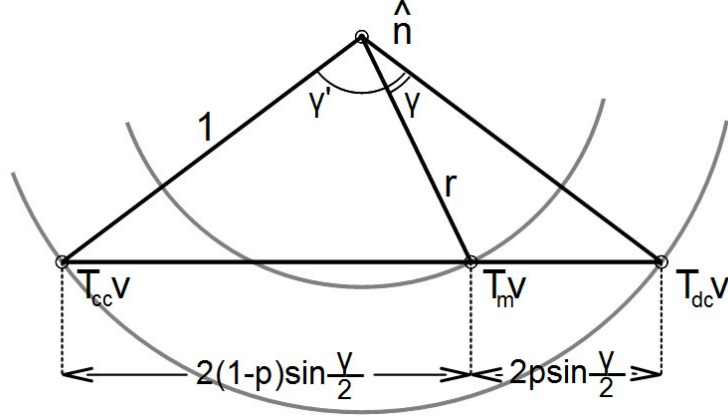
Figure B.6: **Geometric construction for characterizing a probabilistic mixture of a unitary process and a pure, maximally entangled state.** In the plane orthogonal to $\hat{n}$, the image of a given input Bloch vector $\vec{v}$ under T_m lies on the chord connecting the images under T_{dc} and T_{cc}. Its distance from the centre, which gives the radius r, is related to the angle γ spanned by the chord and the probability p of common cause in the mixture.

The image of the Bloch sphere under such a combination is shown in Fig. 1. It must still be an ellipsoid, since T_m is an affine transformation. Furthermore, it inherits the symmetry under rotation about $\hat{n}$. Therefore it has one semi-axis (eigenvector of $T_m T_m^T$) along $\hat{n}$, and a degenerate pair orthogonal to it. The length of the semi-axis (square root of eigenvalue) along $\hat{n}$ is $|1 - 2p|$, because the images under T_{dc} and T_{cc} along this direction are diametrically opposed. When $p = \frac{1}{2}$, this implies that the ellipsoid reduces to a disk. For $p < \frac{1}{2}$, the contribution from the process dominates, so $\det T_m > 0$, while $\det T_m < 0$ heralds $p > \frac{1}{2}$. The length of the other two semi-axes, in the plane orthogonal to $\hat{n}$, can be obtained using the geometrical construction in Fig. 2:

$$\sin^2 \frac{\gamma}{2} = \frac{1 - r^2}{4\,(p - p^2)}. \tag{B.49}$$

The images of points under T_m that lie in this plane are rotated from the corresponding images under T_{dc} by an angle γ', in the same direction (same sign) as γ above, and with magnitude given by

$$2r \cos \gamma' = 1^2 + r^2 - \left[2p \sin \frac{\gamma}{2}\right]^2. \tag{B.50}$$

Given an ellipsoid that arose from such a convex combination, it is straightforward to extract the direction $\hat{n}$, the probability p and the angle γ. (In the pathological case that all

three semi-axes have the same length, one finds that $\gamma = 0$, which implies that the image of T_{cc} is diametrically opposed to that of T_{dc} for all inputs, and there is no need to single out a direction $\hat{n}$. The probability p can still be read off normally.)

Given those parameters, the following steps then allow one to recover T_{dc} from T_m: (1) scaling by $1/(1-2p)$ in the direction of $\hat{n}$ and $1/r$ in the perpendicular plane, $S_{\perp\hat{n},1/r}S_{\hat{n},1/(1-2p)}$; and (2) rotation about $\hat{n}$ by $-\gamma'$, $R_{\hat{n},-\gamma'}$:

$$T_{dc} = R_{\hat{n},-\gamma'}S_{\perp\hat{n},1/r}S_{\hat{n},1/(1-2p)}T_m, \tag{B.51}$$

and similarly the common-cause contribution can be found via

$$T_{cc} = R_{\hat{n},-\gamma+\gamma'}S_{\perp\hat{n},1/r}S_{\hat{n},1/(2p-1)}T_m. \tag{B.52}$$

Note that there is an ambiguity in the direction of the rotations: assuming we take γ and γ' to be non-negative by convention, the orientation of $\hat{n}$ (which is not fixed by the ellipsoid) generates two possible solutions. However, they are related by simple rotations of T_{cc} and T_{dc} about $\hat{n}$ by fixed angles. The ambiguity is removed when $\gamma = 0$, as is the case in the example that we implemented in our experiment, mixing the identity channel and the state $|\Phi^+\rangle$. But even if this ambiguity persists, given a probabilistic mixture of any unitary process and any maximally entangled pure bipartite state, we can uniquely determine the mixing probability p as well as the angle γ and the direction of $\hat{n}$ up to an inversion about the origin.

The role of coherence and entanglement

The previous section shows that *extremal* states and processes can be distinguished perfectly by passive observation alone, and if one is promised a probabilistic mixture of two such objects, the causal inference problem can be solved completely without the need for interventions.

Without the promise of extremality, however, passive observation does not allow a complete solution of the causal inference problem. Indeed, when confronted with a channel that is entanglement-breaking, or a bipartite state that is separable, passive observation does not provide *any* information about the causal relations. This is because the sets of correlations that can arise from the two scenarios are identical, corresponding to conditional states that are both positive and PPT. In these cases, we have the same ambiguity as is found classically. These cases can be identified by their steering ellipsoid using a criterion due to Jevtic et al. [97]: a two-qubit state is separable and a single-qubit channel is

entanglement-breaking if and only if the ellipsoid it defines fits inside a tetrahedron which is in turn circumscribed by the Bloch sphere.

It follows that in order to obtain some information about the causal relations, it is necessary that one or both of the following conditions hold: the direct-cause mechanism is a channel that preserves some coherence, or the common-cause mechanism is a bipartite state that has some entanglement. We conclude that having either coherence or entanglement is a necessary conditions for achieving a quantum advantage for causal inference.

Conversely, coherence of the process and entanglement of the bipartite state is also a sufficient condition for inferring the causal structure, if we are promised that it is either purely common-cause or purely direct-cause, and the systems are qubits. To see this, recall that two-qubit states are separable if and only if they have a positive partial transpose. If the state is known to be entangled, its partial transpose must not be positive, $\rho_{B|C}^{T_C} \not\geq 0$, which implies a pattern of correlations that rules out a direct-cause explanation. Similarly, single-qubit processes that are not entanglement-breaking have $\rho_{B|D} \not\geq 0$, which rules out the common-cause explanation. Thus we can identify the causal structure unambiguously.

B.13.3 Reconstructing the causal map in the presence of noise

We have shown that for the interventionist scheme, we can reconstruct the causal map from the observed statistics, and in the passive observation scheme, we can do so if we are given a promise about the form of the causal map. In an experiment with a finite number of runs, the observed statistics are subject to statistical fluctuations, therefore one estimates the causal map by a least-squares fit procedure. That is, one determines the causal map that generates statistics that are closest, according to a particular figure of merit, to the observed statistics. In this section, we describe some of the details of this fitting procedure. We first consider data from the interventionist scheme, then present the analysis of data obtained by passive observation.

While the theoretical analysis in the previous sections was based on relative frequencies of outcomes given settings, such as $P(km|lstu)$, the statistical analysis of experimental data is based directly on the numbers of counts obtained for each combination of parameters. We denote the observed absolute frequencies by $\tilde{P}^{\mathrm{obs}}(km|lstu)$. This is the number of coincidence counts detected when the wave-plates before and after the polarizers are set to implement a certain set of values of $klmstu$. Assuming that each set of values $klmstu$ was implemented on N runs of the experiment, we can write the count numbers predicted by the fitting model as

$$\tilde{P}^{\mathrm{fit}}(km|lstu) = NP^{\mathrm{fit}}(km|lstu). \tag{B.53}$$

The relative frequencies $P^{\text{fit}}(km|lstu)$ are given in terms of the causal map $\rho_{CB|D}$ by

$$P^{\text{fit}}(km|lstu) = \text{Tr}_{CBD}\left[\rho_{CB|D}(\Pi^C_{sk} \otimes \Pi^B_{um} \otimes \Pi^D_{tl})\right]. \tag{B.54}$$

We do not consider the most general form of a causal map, but use the promise that the causal structure is a probabilistic mixture of common-cause and direct-cause:

$$\rho_{CB|D} = p\rho_{CB} \otimes \mathbb{1}_D + (1-p)\rho_C \otimes \rho_{B|D}, \tag{B.55}$$

where ρ_{CB} and ρ_C are density operators, ie trace-one positive-semidefinite, and $\rho_{B|D}$ is PPT and satisfies the law of total probability, since it represents a channel. Thus, we can consider our model to be parameterized by p, N and the operators ρ_{CB}, ρ_C, $\rho_{B|D}$, with the predicted count numbers given by

$$P^{\text{fit}}(km|lstu) = pN\text{Tr}[\rho_{CB}(\Pi^C_{sk} \otimes \Pi^B_{um})] \tag{B.56}$$

$$+(1-p)N\text{Tr}[\rho_C\Pi^C_{sk}]\text{Tr}[\rho_{B|D}(\Pi^B_{um} \otimes \Pi^D_{tl})]. \tag{B.57}$$

The fitting is simplified if, rather than imposing the appropriate normalization of all the operators and subsequently including additional parameters N and p, we allow one operator in each term to be unnormalized: we define

$$\tilde{\rho}_{CB} \equiv pN\rho_{CB} \tag{B.58}$$

$$\tilde{\rho}_C \equiv (1-p)N\rho_C, \tag{B.59}$$

in terms of which

$$P^{\text{fit}}(km|lstu) = \text{Tr}[\tilde{\rho}_{CB}(\Pi^C_{sk} \otimes \Pi^B_{um})] \tag{B.60}$$

$$+\text{Tr}[\tilde{\rho}_C\Pi^C_{sk}]\text{Tr}[\rho_{B|D}(\Pi^B_{um} \otimes \Pi^D_{tl})]. \tag{B.61}$$

We seek the model, parametrized by $\tilde{\rho}_{CB}$, $\tilde{\rho}_C$ and $\rho_{B|D}$, that best fits the observed frequencies, in the sense that it minimizes the residue

$$\chi^2 = \sum_{klmstu} \frac{\left[\tilde{P}^{\text{fit}}(km|lstu) - \tilde{P}^{\text{obs}}(km|lstu)\right]^2}{\tilde{P}^{\text{fit}}(km|lstu)}. \tag{B.62}$$

Recall from Section B.13.1 that $\rho_{CB|D}$ can be expressed as a function of the statistics one would obtain in the limit of infinitely many runs. It follows that we expect the least-squares fit of experimental data to find a unique global minimum, with the best-fitting $\rho_{CB|D}$ close to the one realized in the experiment.

In the case of passive observation, the observed absolute frequencies are $\tilde{P}^{\text{obs}}(km|su)$. The absolute frequencies predicted by the model are related to the relative frequencies by the number of runs for each set of values of the settings $kmsu$, which we denote N:

$$\tilde{P}^{\text{fit}}(km|su) = NP^{\text{fit}}(km|su). \tag{B.63}$$

Considering a probabilistic mixture of common-cause and direct-cause, and recalling that, in the passive observation scheme, we reprepare the same state Π_{sk} on D that was found on C, the relative frequencies are

$$P^{\text{fit}}(km|su) = p\text{Tr}[\rho_{CB}(\Pi_{sk}^C \otimes \Pi_{um}^B)] \tag{B.64}$$
$$+(1-p)\text{Tr}[\rho_C \Pi_{sk}^C]\text{Tr}[\rho_{B|D}(\Pi_{um}^B \otimes \Pi_{sk}^D)], \tag{B.65}$$

where again ρ_{CB} and ρ_C are states, while $\rho B|D$ represents a channel. Combining the two previous equations and defining the unnormalized operators

$$\tilde{\rho}_{CB} \equiv pN\rho_{CB} \tag{B.66}$$
$$\tilde{\rho}_C \equiv (1-p)N\rho_C, \tag{B.67}$$

we can write the count numbers predicted by the model for the case of passive observation as

$$P^{\text{fit}}(km|su) = \text{Tr}[\tilde{\rho}_{CB}(\Pi_{sk}^C \otimes \Pi_{um}^B)] \tag{B.68}$$
$$+\text{Tr}[\tilde{\rho}_C \Pi_{sk}^C]\text{Tr}[\rho_{B|D}(\Pi_{um}^B \otimes \Pi_{sk}^D)]. \tag{B.69}$$

We seek to minimize the residue

$$\chi^2 = \sum_{kmsu} \frac{\left[\tilde{P}^{\text{fit}}(km|su) - \tilde{P}^{\text{obs}}(km|su)\right]^2}{\tilde{P}^{\text{fit}}(km|su)}. \tag{B.70}$$

As we have shown in Section B.13.2, if there is a promise that $\rho_{CB|D}$ represents a probabilistic mixture of a pure maximally entangled bipartite state and a unitary channel, then $\rho_{BC|D}$ can be obtained from the data in the passive observation scheme up to a sign ambiguity. It follows that for our experiment, which aims to prepare a mixture of this type which removes the ambiguity, we expect there to be a unique global minimum of χ^2 in parameter space, and that consequently the $\rho_{CB|D}$ which best fits the data will be close to the one realized in the experiment. Note that we do not impose maximal entanglement of ρ_{CB} or unitarity of the map associated to $\rho_{B|D}$ as a constraint in our fit. Nonetheless,

as long as the experiment has come close to achieving these ideals, we expect the fit to be good over only a small interval of possibilities for ρ_{CB}, ρ_C, $\rho_{B|D}$, and the value of p.

The operators that parametrize our model are subject to the following constraints, based on properties derived in section B.13.2. The unnormalized states $\tilde{\rho}_{CB}$ and $\tilde{\rho}_C$ are positive-semidefinite, and their traces are related by

$$\frac{\text{Tr}_{CB}\tilde{\rho}_{CB}}{\text{Tr}_{CB}\tilde{\rho}_{CB} + \text{Tr}_C\tilde{\rho}_C} = p. \tag{B.71}$$

The conditional $\rho_{B|D}$ is PPT and satisfies the law of total probability,

$$\text{Tr}_B\rho_{B|D} = \mathbb{1}_D. \tag{B.72}$$

The positive-semidefinite operators invoked above can be parametrized conveniently following Ref. [5]. A two-qubit positive-semidefinite operator such as $\tilde{\rho}_{CB}$ requires 16 real numbers, which we arrange into a vector $\vec{r}_{CB}$. Define the lower-triangular 4 by 4 matrix

$$R_{CB} = \begin{pmatrix} r_1 & 0 & 0 & 0 \\ r_5 + \imath r_6 & r_2 & 0 & 0 \\ r_{11} + \imath r_{12} & r_7 + \imath r_8 & r_3 & 0 \\ r_{15} + \imath r_{16} & r_{13} + \imath r_{14} & r_9 + \imath r_{10} & r_4 \end{pmatrix}, \tag{B.73}$$

and take

$$\tilde{\rho}_{CB} = R_{CB}^\dagger R_{CB}. \tag{B.74}$$

This form is manifestly positive-semidefinite, and by varying over the vectors $\vec{r}_{CB}$, we vary over all $\tilde{\rho}_{CB}$. A further convenient feature of this parametrization is that the trace of ρ_{CB} is given simply by square of the 2-norm of $\vec{r}_{CB}$,

$$\text{Tr}_{CB}\tilde{\rho}_{CB} = |\vec{r}_{CB}|^2. \tag{B.75}$$

Positive-semidefinite operators for a single qubit can be obtained by a similar construction: a vector of 4 real numbers, $\vec{r}_C$, defines the components of a lower triangular 2 by 2 matrix R_C, in terms of which $\rho_C = R_C^\dagger R_C$. If a PPT operator $\rho_{B|D}$ is called for, one can take the partial transpose of the above form: $\vec{r}_{B|D}$ is again a vector of 16 real numbers that defines a matrix $R_{B|D}$ by Eq. (B.73), and one takes $\rho_{B|D} = (R_{B|D}^\dagger R_{B|D})^{T_D}$, where T_D is the partial transpose. We note that the trace of the PPT operator is also given by the square of the norm of its parameter vector: $\text{Tr}_{BD}\tilde{\rho}_{B|D} = |\vec{r}_{B|D}|^2$.

The additional constraints on operators are enforced by adding penalty functions to the principal function χ^2. The constraint that relates the traces of the unnormalized operators

in each term to the probability p, Eq. (B.71), can be cast directly in terms of the norms of the parameter vectors: we add a term

$$\lambda \left(\frac{|\vec{r}_{CB}|^2}{|\vec{r}_{CB}|^2 + |\vec{r}_C|^2} - p \right)^2 . \tag{B.76}$$

The additive term enforcing the law of total probability, Eq. (B.72), is proportional to the sum of the absolute value squared of the elements of the difference between $\mathrm{Tr}_B \rho_{B|D}$ and $\mathbb{1}_D$,

$$\lambda \sum_{ij} \left| \left(\mathrm{Tr}_B \rho_{B|D} - \mathbb{1}_D \right)_{ij} \right|^2 . \tag{B.77}$$

The Lagrange multiplier λ for each penalty term was selected heuristically, with values of 10^7 found to enforce the constraints without obscuring the principal function.

Pattern of correlations				Direct-cause explanation?	Common-cause explanation?
C_{11}	C_{22}	C_{33}	$\Pi_s\, C_{ss}$		
$+1$	$+1$	$+1$	$+1$	$\mathcal{E}(\cdot) = \mathbb{1}(\cdot)\mathbb{1}$	No
$+1$	-1	-1	$+1$	$\mathcal{E}(\cdot) = \sigma_1(\cdot)\sigma_1$	No
-1	$+1$	-1	$+1$	$\mathcal{E}(\cdot) = \sigma_2(\cdot)\sigma_2$	No
-1	-1	$+1$	$+1$	$\mathcal{E}(\cdot) = \sigma_3(\cdot)\sigma_3$	No
-1	-1	-1	-1	No	$\rho = |\Psi^-\rangle\langle\Psi^-|$
-1	$+1$	$+1$	-1	No	$\rho = |\Phi^-\rangle\langle\Phi^-|$
$+1$	-1	$+1$	-1	No	$\rho = |\Phi^+\rangle\langle\Phi^+|$
$+1$	$+1$	-1	-1	No	$\rho = |\Psi^+\rangle\langle\Psi^+|$

Table B.1: **Signatures of causal structure accessible by passive observation.** Suppose the same Pauli observable is measured on both A and B, i.e., $(s, u) \in \{(1,1), (2,2), (3,3)\}$, and suppose the outcomes k and m are found to be perfectly correlated, either positively or negatively, with correlation coefficients $C_{su} \equiv p(k = m|su) - p(k \neq m|su) \in \{\pm 1\}$. For simplicity, we also assume that the marginal distribution over k (respectively m) is uniform for all values s (respectively u). In this case, perfect negative correlation for all three observables can only be explained by a common cause, namely, when the measurements are implemented on two qubits prepared in the singlet state $\rho = |\Psi^-\rangle\langle\Psi^-|$. There is no channel that produces this pattern: it would constitute a universal NOT gate, which is not a completely positive map. Similarly, positive correlation for all three observables admits of a direct-cause explanation, namely, when the measurements are implemented on the input and output of the identity channel $\mathcal{E}(\cdot) = \mathbb{1}(\cdot)\mathbb{1}$. No bipartite state has this pattern of correlations, a fact sometimes described as the nonexistence of an 'antisinglet' state. Every row of the table can be explained in this fashion. It emerges that it is the product of the correlation coefficients, $C_{11} \cdot C_{22} \cdot C_{33}$, which contains the signature of the causal structure. Notation: σ_1, σ_2 and σ_3 are the Pauli matrices and $|\Psi^\pm\rangle \equiv \frac{1}{\sqrt{2}}(|0\rangle|1\rangle \pm |1\rangle|0\rangle)$, $|\Phi^\pm\rangle \equiv \frac{1}{\sqrt{2}}(|0\rangle|0\rangle \pm |1\rangle|1\rangle)$ are the Bell states, with $\{|0\rangle, |1\rangle\}$ the eigenstates of σ_3.

References

[1] Dagmar Bruß. Characterizing entanglement. Journal of Mathematical Physics, 43(9):4237–4251, 2002.

[2] J. S. Bell. On the Einstein-Podolsky-Rosen paradox. Physics, 1(3):195–200, 1964.

[3] Michael A. Nielsen and Isaac L. Chuang. Quantum computation and quantum information. Cambridge University Press, 2010.

[4] G. Mauro D'Ariano, Matteo G. A. Paris, and Massimiliano F. Sacchi. Quantum tomography. Advances in Imaging and Electron Physics, 128:206–309, 2003.

[5] Daniel F. V. James, Paul G. Kwiat, William J. Munro, and Andrew G. White. Measurement of qubits. Physical Review A, 64(5):052312, 2001.

[6] I. D. Ivanovic. Geometrical description of quantal state determination. Journal of Physics A: Mathematical and General, 14(12):3241, 1981.

[7] William K. Wootters and Brian D. Fields. Optimal state-determination by mutually unbiased measurements. Annals of Physics, 191(2):363–381, 1989.

[8] Igor D. Ivanovic. How to differentiate between non-orthogonal states. Physics Letters A, 123(6):257–259, 1987.

[9] Dennis Dieks. Overlap and distinguishability of quantum states. Physics Letters A, 126(5):303–306, 1988.

[10] Asher Peres. How to differentiate between non-orthogonal states. Physics Letters A, 128(1):19, 1988.

[11] Anthony Chefles and Stephen M. Barnett. Optimum unambiguous discrimination between linearly independent symmetric states. Physics Letters A, 250(4):223–229, 1998.

[12] Asher Peres and Daniel R. Terno. Optimal distinction between non-orthogonal quantum states. Journal of Physics A: Mathematical and General, 31(34):7105, 1998.

[13] Yuqing Sun, Mark Hillery, and János A. Bergou. Optimum unambiguous discrimination between linearly independent nonorthogonal quantum states and its optical realization. Physical Review A, 64(2):022311, 2001.

[14] Terry Rudolph, Robert W. Spekkens, and Peter S. Turner. Unambiguous discrimination of mixed states. Physical Review A, 68:010301, Jul 2003.

[15] Philippe Raynal and Norbert Lütkenhaus. Optimal unambiguous state discrimination of two density matrices: Lower bound and class of exact solutions. Physical Review A, 72:022342, Aug 2005.

[16] Philippe Raynal and Norbert Lütkenhaus. Optimal unambiguous state discrimination of two density matrices: A second class of exact solutions. Physical Review A, 76:052322, Nov 2007.

[17] M. A. Jafarizadeh, M. Rezaei, N. Karimi, and A. R. Amiri. Optimal unambiguous discrimination of quantum states. Physical Review A, 77(4):042314, 2008.

[18] H. Sugimoto, T. Hashimoto, M. Horibe, and A. Hayashi. Complete solution for unambiguous discrimination of three pure states with real inner products. Physical Review A, 82(3):032338, 2010.

[19] Gerald Waldherr, Adetunmise C. Dada, Philipp Neumann, Fedor Jelezko, Erika Andersson, and Jörg Wrachtrup. Distinguishing between nonorthogonal quantum states of a single nuclear spin. Physical Review Letters, 109(18):180501, 2012.

[20] Tao Zhou. Unambiguous discrimination between two unknown qudit states. Quantum Information Processing, 11(6):1669–1684, 2012.

[21] Janoes Bergou, Edgar Feldman, and Mark Hillery. Extracting Information from a Qubit by Multiple Observers: Toward a Theory of Sequential State Discrimination. Physical Review Letters, 111:100501, September 2013.

[22] Carl W. Helstrom. Quantum detection and estimation theory. Academic Press New York, 1976.

[23] Roger Clarke, Anthony Chefles, Stephen M. Barnett, and Erling Riis. Experimental demonstration of optimal unambiguous state discrimination. Physical Review A, 63(4):040305(R), March 2001.

[24] János A. Bergou. Discrimination of quantum states. Journal of Modern Optics, 57(3):160–180, 2010.

[25] Gregorius C. G. Berkhout, Martin P. J. Lavery, Johannes Courtial, Marco W. Beijersbergen, and Miles J. Padgett. Efficient sorting of orbital angular momentum states of light. Phys. Rev. Lett., 105:153601, Oct 2010.

[26] Mohammad Mirhosseini, Mehul Malik, Zhimin Shi, and Robert W. Boyd. Efficient separation of the orbital angular momentum eigenstates of light. Nature communications, 4, 2013.

[27] S. P. Walborn, A. N. de Oliveira, R. S. Thebaldi, and C. H. Monken. Entanglement and conservation of orbital angular momentum in spontaneous parametric down-conversion. Physical Review A, 69:023811, Feb 2004.

[28] Taehyun Kim, Marco Fiorentino, and Franco N. C. Wong. Phase-stable source of polarization-entangled photons using a polarization sagnac interferometer. Phys. Rev. A, 73:012316, 2006.

[29] Alessandro Fedrizzi, Thomas Herbst, Andreas Poppe, Thomas Jennewein, and Anton Zeilinger. A wavelength-tunable fiber-coupled source of narrowband entangled photons. Opt. Express, 15(23):15377–15386, 2007.

[30] C. K. Hong and L. Mandel. Theory of parametric frequency down conversion of light. Physical Review A, 31(4):2409, 1985.

[31] Z. Y. Ou, L. J. Wang, and L. Mandel. Vacuum effects on interference in two-photon down conversion. Physical Review A, 40(3):1428, 1989.

[32] David S. Hum and Martin M. Fejer. Quasi-phasematching. Comptes Rendus Physique, 8(2):180–198, 2007.

[33] Alois Mair, Alipasha Vaziri, Gregor Weihs, and Anton Zeilinger. Entanglement of the orbital angular momentum states of photons. Nature, 412(6844):313–316, 2001.

[34] J. Torres, A. Alexandrescu, and Lluis Torner. Quantum spiral bandwidth of entangled two-photon states. Physical Review A, 68(5), November 2003.

[35] Filippo M. Miatto, Alison M. Yao, and Stephen M. Barnett. Full characterization of the quantum spiral bandwidth of entangled biphotons. Physical Review A, 83(3):033816, 2011.

[36] D. N. Biggerstaff, R. Kaltenbaek, D. R. Hamel, G. Weihs, T. Rudolph, and K. J. Resch. Cluster-state quantum computing enhanced by high-fidelity generalized measurements. Phys. Rev. Lett., 103:240504, 2009.

[37] Charles H. Bennett, David P. DiVincenzo, Peter W. Shor, John A. Smolin, Barbara M. Terhal, and William K. Wootters. Remote state preparation. Physical Review Letters, 87:077902, Jul 2001.

[38] Wei-Tao Liu, Wei Wu, Bao-Quan Ou, Ping-Xing Chen, Cheng-Zu Li, and Jian-Min Yuan. Experimental remote preparation of arbitrary photon polarization states. Physical Review A, 76:022308, Aug 2007.

[39] Charles H. Bennett, Herbert J. Bernstein, Sandu Popescu, and Benjamin Schumacher. Concentrating partial entanglement by local operations. Physical Review A, 53(4):2046, 1996.

[40] M. D. Choi. Completely positive linear maps on complex matrices. Linear Algebra and Applications, 10:285, 1975.

[41] A. Jamiolkowski. Linear transformations which preserve trace and positive semidefiniteness of operators. Reports on Mathematical Physics, 3:275, 1972.

[42] S. P. Walborn, D. S. Lemelle, M. P. Almeida, and P. H. Souto Ribeiro. Quantum key distribution with higher-order alphabets using spatially encoded qudits. Physical review letters, 96(9):090501, 2006.

[43] J. B. Pors, A. Aiello, S. S. R. Oemrawsingh, M. P. van Exter, E. R. Eliel, and J. P. Woerdman. Angular phase-plate analyzers for measuring the dimensionality of multimode fields. Phys. Rev. A, 77:033845, Mar 2008.

[44] C. E. R. Souza, C. V. S. Borges, A. Z. Khoury, J. A. O. Huguenin, L. Aolita, and S. P. Walborn. Quantum key distribution without a shared reference frame. Physical Review A, 77(3):32345, 2008.

[45] S. P. Walborn, D. S. Lemelle, D. S. Tasca, and P. H. Souto Ribeiro. Schemes for quantum key distribution with higher-order alphabets using single-photon fractional fourier optics. Physical Review A, 77(6):062323, 2008.

[46] Jonathan Leach, Barry Jack, Jacqui Romero, Anand K. Jha, Alison M. Yao, Sonja Franke-Arnold, David G. Ireland, Robert W. Boyd, Stephen M. Barnett, and Miles J. Padgett. Quantum correlations in optical angle–orbital angular momentum variables. Science, 329(5992):662–665, 2010.

[47] Megan Agnew, Jonathan Leach, Melanie McLaren, F. Stef Roux, and Robert W. Boyd. Tomography of the quantum state of photons entangled in high dimensions. Physical Review A, 84(6):062101, 2011.

[48] Adetunmise C. Dada, Jonathan Leach, Gerald S. Buller, Miles J. Padgett, and Erika Andersson. Experimental high-dimensional two-photon entanglement and violations of generalized bell inequalities. Nature Physics, 7(9):677–680, 2011.

[49] L. E. Oxman and A. Z. Khoury. Fractional topological phase for entangled qudits. Phys. Rev. Lett., 106:240503, Jun 2011.

[50] Bart-Jan Pors, Filippo Miatto, E. R. Eliel, J. P. Woerdman, et al. High-dimensional entanglement with orbital-angular-momentum states of light. Journal of Optics, 13(6):064008, 2011.

[51] M. Agnew, J. Leach, and R. W. Boyd. Observation of entanglement witnesses for orbital angular momentum states. The European Physical Journal D, 66(6):1–4, 2012.

[52] Jonathan Leach, Eliot Bolduc, Daniel J. Gauthier, and Robert W. Boyd. Secure information capacity of photons entangled in many dimensions. Physical Review A, 85(6):060304, 2012.

[53] Megan Agnew, Jeff Z. Salvail, Jonathan Leach, and Robert W. Boyd. Generation of orbital angular momentum bell states and their verification via accessible nonlinear witnesses. Physical Review Letters, 111(3):030402, 2013.

[54] John M. Donohue, Megan Agnew, Jonathan Lavoie, and Kevin J. Resch. Coherent ultrafast measurement of time-bin encoded photons. Physical Review Letters, 111:153602, Oct 2013.

[55] Mehul Malik, Omar S Magaña-Loaiza, and Robert W. Boyd. Quantum-secured imaging. Applied Physics Letters, 101(24):241103–241103, 2012.

[56] Ulrike Herzog and János A. Bergou. Optimum unambiguous identification of d unknown pure qudit states. Physical Review A, 78(3):032320, 2008.

[57] Shengshi Pang and Shengjun Wu. Optimum unambiguous discrimination of linearly independent pure states. Physical Review A, 80(5):052320, 2009.

[58] János A. Bergou, Ulrike Futschik, and Edgar Feldman. Optimal Unambiguous Discrimination of Pure Quantum States. Physical Review Letters, 108(25):250502, 2012.

[59] LiBing Chen and Hong Lu. Nonlocal unambiguous discrimination among N nonorthogonal qudit states lying in a higher-dimensional Hilbert space. Science China Physics, Mechanics and Astronomy, 55(1):55–59, 2012.

[60] Lvjun Li. Bounds on unambiguous discrimination between quantum states. Physical Review A, 86(3):032320, 2012.

[61] Sonja Franke-Arnold and J. Jeffers. Unambiguous state discrimination in high dimensions. The European Physical Journal D, 66(7):1–4, 2012.

[62] Masoud Mohseni, Aephraim M. Steinberg, and János A. Bergou. Optical realization of optimal unambiguous discrimination for pure and mixed quantum states. Physical Review Letters, 93(20):200403, 2004.

[63] Gesine A. Steudle, Sebastian Knauer, Ulrike Herzog, Erik Stock, Vladimir A. Haisler, Dieter Bimberg, and Oliver Benson. Experimental optimal maximum-confidence discrimination and optimal unambiguous discrimination of two mixed single-photon states. Phys. Rev. A, 83:050304, May 2011.

[64] M. A. Neumark. On a representation of additive operator set functions. C. R. (Doklady) Acad. Sci. URSS, 41(359), 1943.

[65] Daowen Qiu. Minimum-error discrimination between mixed quantum states. Physical Review A, 77(1):012328, 2008.

[66] Robert Fickler, Radek Lapkiewicz, William N. Plick, Mario Krenn, Christoph Schaeff, Sven Ramelow, and Anton Zeilinger. Quantum entanglement of high angular momenta. Science, 338(6107):640–643, 2012.

[67] Judea Pearl. Causality: models, reasoning and inference, volume 29. Cambridge Univ Press, 2000.

[68] Peter Spirtes, Clark Glymour, and Richard Scheines. Causation, Prediction, and Search. MIT Press, 2000.

[69] J. Fitzsimons, J. Jones, and V. Vedral. Quantum correlations which imply causation. arXiv, 2013.

[70] Giulio Chiribella, Giacomo Mauro D'Ariano, and Paolo Perinotti. Theoretical framework for quantum networks. Phys. Rev. A, 80(2):022339, 2009.

[71] Lucien Hardy. The operator tensor formulation of quantum theory. Philos. T. Roy. Soc. A, 370(1971):3385–3417, 2012.

[72] O. Oreshkov, F. Costa, and C. Brukner. Quantum correlations with no causal order. Nature Communications, 3:1092, 2012.

[73] Yakir Aharonov, Sandu Popescu, Jeff Tollaksen, and Lev Vaidman. Multiple-time states and multiple-time measurements in quantum mechanics. Phys. Rev. A, 79(5):052110, 2009.

[74] Robert Oeckl. A "general boundary" formulation for quantum mechanics and quantum gravity. Phys. Lett. B, 575(3):318–324, 2003.

[75] M. S. Leifer and Robert W. Spekkens. Towards a formulation of quantum theory as a causally neutral theory of bayesian inference. Phys. Rev. A, 88(5):052130, 2013.

[76] Matthew S. Leifer. Quantum dynamics as an analog of conditional probability. Phys. Rev. A, 74(4):042310, 2006.

[77] G. M. D'Ariano and P. Lo Presti. Quantum tomography for measuring experimentally the matrix elements of an arbitrary quantum operation. Phys. Rev. Lett., 86:4195–4198, May 2001.

[78] J. B. Altepeter, D. Branning, E. Jeffrey, T. C. Wei, P. G. Kwiat, R. T. Thew, J. L. O'Brien, M. A. Nielsen, and A. G. White. Ancilla-assisted quantum process tomography. Phys. Rev. Lett., 90:193601, 2003.

[79] Richard Jozsa. Fidelity for mixed quantum states. J. Mod. Opt., 41(12):2315–2323, 1994.

[80] Michael Marc Wolf, J. Eisert, T. S. Cubitt, and J. I. Cirac. Assessing non-Markovian quantum dynamics. Phys. Rev. Lett., 101(15):150402, 2008.

[81] Elsi-Mari Laine, Jyrki Piilo, and Heinz-Peter Breuer. Measure for the non-markovianity of quantum processes. Phys. Rev. A, 81(6):062115, 2010.

[82] Ángel Rivas, Susana F. Huelga, and Martin B. Plenio. Quantum non-Markovianity: Characterization, quantification and detection. arXiv:1405.0303, 2014.

[83] Ángel Rivas, Susana F. Huelga, and Martin B. Plenio. Entanglement and non-Markovianity of quantum evolutions. Phys. Rev. Lett., 105(5):050403, 2010.

[84] Xiao-Ming Lu, Xiaoguang Wang, and C. P. Sun. Quantum Fisher information flow and non-Markovian processes of open systems. Phys. Rev. A, 82(4):042103, 2010.

[85] Bi-Heng Liu, Li Li, Yun-Feng Huang, Chuan-Feng Li, Guang-Can Guo, Elsi-Mari Laine, Heinz-Peter Breuer, and Jyrki Piilo. Experimental control of the transition from Markovian to non-Markovian dynamics of open quantum systems. Nature Physics, 7:931–934, 2011.

[86] Jian-Shun Tang, Chuan-Feng Li, Yu-Long Li, Xu-Bo Zou, Guang-Can Guo, Heinz-Peter Breuer, Elsi-Mari Laine, and Jyrki Piilo. Measuring non-Markovianity of processes with controllable system-environment interaction. EPL (Europhysics Letters), 97(1):10002, 2012.

[87] J. Wallman, S. Flammia, M. Barnhill, and J. Emerson. Simpler, faster, better: robust randomized benchmarking tests for non-unitality and non-Markovianity in quantum devices. In Bulletin of the American Physical Society, 2014.

[88] P. Pechukas. Reduced dynamics need not be completely positive. Phys. Rev. Lett., 73:1060, 1994.

[89] N. Boulant, J. Emerson, T. F. Havel, D. G. Cory, and S. Furuta. Incoherent noise and quantum information processing. J. Chem. Phys., 121:2955, 2004.

[90] Y. S. Weinstein, T. F. Havel, J. Emerson, N. Boulant, M. Saraceno, S. Lloyd, and D. G. Cory. Quantum process tomography of the quantum Fourier transform. J. Chem. Phys., 121:6117, 2004.

[91] M. Howard, J. Twamley, C. Wittmann, T. Gaebel, F. Jelezko, and J. Wrachtrup. Quantum process tomography and Lindblad estimation of a solid-state qubit. New Journal of Physics, 8(3):33, 2006.

[92] H. Carteret, D. R. Terno, and K. Zyczkowski. Physical accessibility of non-completely positive maps. Phys. Rev. A, 77:042113, 2008.

[93] P. G. Kwiat, J. R. Mitchell, P. D. D. Schwindt, and A. G. White. Grover's search algorithm: an optical approach. J. Mod. Opt., 47(2-3):257–266, 2000.

[94] Tomohisa Nagata, Ryo Okamoto, Jeremy L. O'Brien, Keiji Sasaki, and Shigeki Takeuchi. Beating the standard quantum limit with four-entangled photons. Science, 316:726, 2007.

[95] Ingemar Bengtsson and Karol Zyczkowski. Geometry of quantum states. Cambridge Univ. Press, New York, 2006.

[96] H. M. Wiseman, S. J. Jones, and A. C. Doherty. Steering, entanglement, nonlocality, and the Einstein-Podolsky-Rosen paradox. Phys. Rev. Lett., 98:140402, Apr 2007.

[97] Sania Jevtic, Matthew F. Pusey, David Jennings, and Terry Rudolph. The quantum steering ellipsoid. arXiv:1303.4724, 2013.